Group III-Nitride Nanowires as Multifunctional Optical Biosensors

---

Dissertation zur Erlangung des Grades

Doktor der Naturwissenschaften

vorgelegt dem

Fachbereich 07 - Mathematik und Informatik, Physik, Geographie

von

Sara Sibylle Hölzel

Master of Science
Materialwissenschaften

Gießen 2018

Justus-Liebig-Universität Gießen
I. Physikalisches Institut
AG Prof. Dr. Martin Eickhoff
Nanotechnologische Materialien

Abgabedatum: 03.09.2018
Erstgutachter: Prof. Dr. Martin Eickhoff
Zweitgutachter: Prof. Dr. Detlev Hofmann

Abstract

The application of InGaN/GaN nanowire heterostructures (NWHs) and GaN nanowires (NWs) as electrodes for the simultaneous photoelectrochemical and optical detection of charge transfer processes caused by near-surface chemical reactions and optical interactions is investigated.

In the first chapter, the charge transfer between InGaN/GaN NWH electrodes and an aqueous electrolyte in presence of ascorbic acid, uric acid and hydrogen peroxide (H_2O_2) was investigated by simultaneous photoluminescence (PL) and photocurrent (PC) measurements. The analysis revealed that the acidic dissociation of these molecules modifies the surface charge in the NW resulting in a reduction of the barrier height and surface band bending (SBB), respectively. These electrodes allow for the detection of the molecules by oxidation due to a transfer of photo-generated holes. Furthermore, the detection of ascorbic acid with uric acid and H_2O_2 as background signals as well as the identification of H_2O_2 with ascorbic and uric acid as background signals is shown.

In the second section of this chapter, the charge transfer processes between GaN NW electrodes and covalently immobilized charge separation triad molecules are analyzed. The excitation of the photoactive triad molecules resulted in a modulation of the PC. The increase of the anodic PC was attributed to a direct electron transfer via the photoactive fullerenes or by the decrease of the barrier height due to dipole formation at the interface. Simultaneous PL and PC measurements proved the establishment of a negative charge at the interface which increases the effective SBB and thus, enhances the charge transfer between photo-generated charge carriers from the NW and the electrolyte. Additionally, the experiments revealed that the presence of surface states is relevant for the performance of the electrode.

In the second chapter of this work, InGaN/GaN NWH arrays as optochemical electrodes in combination with a standard optical microscope were used for the optical readout and imaging of biochemical processes that are based on local changes of the pH or the electrical potential. The resolution limits were studied and a bias resolution of $\Delta U_C \leq 1\,\mathrm{mV}$, a pH resolution of $\Delta\mathrm{pH} \leq 0.03$ and a time resolution of $\Delta t \leq 50\,\mathrm{ms}$ could be shown. The imaging of biochemical processes with chemical contrast was demonstrated by the investigation of the sodium/proton exchanger of isolated crypts of rats. It is shown that quantitative analysis of the pH changes with a spatial resolution of below $\Delta\mathrm{x} < 0.63\,\mu\mathrm{m}$ is possible.

Hence, it is demonstrated that the photoelectrochemical analysis of InGaN/GaN NWH and GaN NW electrodes allows the identification of the interfacial reactions as dynamic equilibrium by monitoring the PL and PC which serve as measurand for the SBB. In addition, the NWH arrays allow for bioimaging by providing high spatial and temporal resolution.

Zusammenfassung

Die Anwendung von Elektroden auf Basis von InGaN/GaN-Nanodrahtheterostrukturen (NWHs) und GaN-Nanodrähten (NWs) zur optischen und photoelektrochemischen Detektion von Ladungstransferprozessen durch oberflächennahe chemische Reaktionen oder optische Wechselwirkungen wird in dieser Arbeit untersucht.
Im ersten Kapitel wird zunächst der Ladungstransfer zwischen InGaN/GaN-NWH-Elektroden und einem wässrigen Elektrolyten bei Anwesenheit von Ascorbinsäure, Harnsäure und Wasserstoffperoxid (H_2O_2) durch die simultane Messung der Photolumineszenz(PL) und des Photostroms (PC) untersucht. Hier kann gezeigt werden, dass die Dissoziation dieser Moleküle die Oberflächenladung an der Grenzfläche verändert, wodurch die Oberflächenbandverbiegung (SBB) abnimmt. Ebenso wird gezeigt, dass Oberflächenzustände bei dem Ladungstransfer eine wichtige Rolle spielen. Die Moleküle konnten mit den InGaN/GaN-NWH-Elektroden anhand ihrer Oxidation durch photogenerierte Ladungsträger und den damit verbundenen Oxidationsphotostrom detektiert werden. Des Weiteren wurde im Verlauf dieser Arbeit die Detektion von Ascorbinsäure in Anwesenheit von Harnsäure und H_2O_2 als auch die Detektion von H_2O_2 in Anwesenheit von Ascorbin- und Harnsäure gezeigt.
Im zweiten Teil dieses Kapitels werden die Ladungstransferprozesse zwischen GaN-NW-Elektroden und kovalent immobilisierten Molekülen (Triadmoleküle), die eine Ladungstrennung erzeugen können, analysiert. Die Anregung der photoaktiven Triadmoleküle führte zu einer Modulation des Photostroms. Die Zunahme des anodischen Stroms wurde einem direkten Elektronentransfer über die photoaktiven Fullerene oder der Abnahme der Barrierenhöhe aufgrund der Entstehung von Dipolen an der Grenzfläche zugeschrieben. Simultane PL- und Photostrommessungen belegten die Bildung einer negativen Ladung an der Grenzfläche, die die effektive Oberflächenbandverbiegung erhöht und so den Ladungstransfer zwischen photogenerierten Ladungsträgern aus dem NW und dem Elektrolyten verstärkt. Zusätzlich zeigten die Experimente, dass Oberflächenzustände die Leistung der Elektrode beeinflussen.
Im zweiten Kapitel dieser Arbeit wurden InGaN/GaN-NW-Arrays als optochemische Elektroden in Kombination mit einem optischen Mikroskop für die Detektion und das Abbilden biochemischer Prozesse, die auf lokalen pH- oder Spannungsänderungen basieren, verwendet. Es konnte eine Auflösung von $\Delta U_C \leq 1\,\mathrm{mV}$ für die Spannung und von $\Delta\mathrm{pH} \leq 0.03$ für den pH Wert sowie eine Zeitauflösung von $\Delta t \leq 50\,\mathrm{ms}$ gezeigt werden. Das Abbilden biochemischer Prozesse mit chemischem Kontrast wurde durch die Untersuchung des Natrium/Wasserstoffionen-Austauschers isolierter Krypten von Wistar Ratten nachgewiesen. Die quantitative Analyse des pH-Wertes mit einer räumlichen Auflösung von unter $\Delta\mathrm{x} < 0.63\,\mu\mathrm{m}$ ist möglich.
Damit konnte gezeigt werden, dass die photoelektrochemische Analyse von InGaN/GaN-

NWH- und GaN-NW-Elektroden die Identifizierung der Grenzflächenreaktionen als dynamisches Gleichgewicht, mit PL und PC als Messgrößen für die SBB, ermöglicht. Darüber hinaus können NWH-Arrays für das Abbilden biochemischer Prozesse mit hoher räumlicher und zeitlicher Auflösung verwendet werden.

Contents

Abbreviations

A	anodic
AA	ascorbic acid
abs	absorption
acc	acceleration
Ag/AgCl	silver/silver chloride
Al	aluminum
APTES	(3-aminopropyl)trimethoxysilane
B	barrier
C	cathodic
C	conduction
CCD	charge-coupled device
CdSe	cadmium selenide
C60	fullerene
E	energy
em	emission
exc	excitation
F	Fermi
Fc	ferrocene
GaN	gallium nitride
gap	band gap
H_2O_2	hydrogen peroxide
InGaN	indium gallium nitride
max	maximum
N_2	nitrogen
NW(s)	nanowire(s)
OCP	open circuit potential
PAH-FITC	polycationic solution of poly(allylamine) hydrochloride conjugated with fluorescein
PC	photocurrent
photo	photoexcitation
PL	photoluminescence
PSS	polyanionic poly(sodium-4-styrene sulfonate)
QDs	quantum dots
SBB	surface band bending
SCR	space charge region

SEM	scanning electron microscopy
Si	silicon
UA	uric acid
UV/Vis	ultraviolet/visible
V	valence
VAC	vacuum
ZnP	zinc porphyrin
ZnS	zinc sulfide
α	degree of dissociation
b	bowing parameter
c	concentration
D	molecule
W	depletion width
d	diameter
E_0	standard potential
E_C	conduction band edge
E_V	valence band edge
f	effective focal length
$FWHM$	full width at half maximum
λ	wavelength
l	length
I	current
j	current density
m	mass
NA	numerical aperture
ϑ	temperature
Φ	flux
φ	potential
Φ_quantum	quantum yield
pk_a	acid dissociation constant
P	power
ρ	specific electrical resistance
L	shell number
σ	conductivity
SNR	signal-to-noise ratio
T	temperature
t	time
U	voltage
v	speed
V	potential
W	width
WD	working distance

Chapter 1

Introduction

Biosensors allow the detection and quantification of biological relevant processes and substances. They mainly consist of a recognition element and a transducer that enables for conversion of the signal into a measured physical quantity. Biosensors are important for the development and analysis in biological and medical areas [1–3]. Especially, the development of semiconductor biosensors has attracted attention and the research in this field is still increasing [4, 5].

The design and development of semiconductor biosensors started in 1970, when the first silicon-based ion-sensitive field-effect transistors (Si-ISFETs) were reported where the ion sensitivity is determined by the gate dielectric [6]. Subsequently, solution-gated FETs (SGFETs) with immobilized enzymes on the gate area were used for electrical detection of enzyme-catalyzed reactions [7, 8]. Both spatial and temporal resolution was achieved using Si-based SGFET arrays [9]. Nevertheless, SiO_2 surfaces featured electrochemical instability [10,11]. Since transistors suffer parasitic currents due to photoexcitation, these electrodes are not appropriate for imaging applications with the use of optical microscope technology which is a requirement to progress in the field of biology, medicine and diagnostic analysis.

In general, semiconductor materials as transducers for biosensors require certain characteristics such as a sufficient response at room temperature and biochemical stability under physiological conditions. Usually, the analyte is detected by its interaction with the transducer. A simple strategy of (bio-)chemical recognition is the detection of reaction-associated changes such as pH changes or the induction of an electric field. In this approach, the performance does not rely on any surface functionalization. For this purpose, the transducer material needs to possess an intrinsic property converting the microscopic change into a macroscopic response.

Group III-nitride nanowires (NWs) and nanowire heterostructures (NWHs) possess a stable photoluminescence (PL) intensity at room temperature that was recently demonstrated to sensitively respond to changes in the pH of the surrounding electrolyte solution and to an external bias application [12]. This allows the detection via optical readout. Since the lateral band bending can be modified by both, the pH and the bias, the definition of an electrochemical working point with enhanced sensitivity can be realized. InGaN/GaN

NWHs qualify for the local detection of near-surface reactions with each nanowire probing the changes in the surface band bending.

These material systems are suited for biochemical sensing purposes since they are electrochemically stable [13–15] and the surface was demonstrated to possess non-toxic properties towards living cells [15] and to exhibit a pH sensitivity of about 55 mV/pH [15–17]. To enhance the sensor selectivity, the nanowire surface allows for chemical functionalization. For this purpose, biomolecules can be covalently immobilized [16, 18, 19] and further modified with enzymes for biosensing applications [20, 21].

In this work, GaN nanowires and InGaN/GaN nanowire heterostructures as multifunctional optical biosensors are presented. In the first part, the charge transfer mechanisms of photo-excited carriers at the semiconductor/electrolyte interface are investigated. The optical detection of group III-nitride NWs is based on the modification of the surface band bending by surface charges. This modulation results in shifting the proportion of radiative and non-radiative processes that, among others, is trackable by photoluminescence and photocurrent (PC) measurements. The effects of this modulation of the PL intensity as radiative process has already been investigated [12] and also the use for (bio-)chemical applications was demonstrated [22]. Furthermore, the photocurrent density as one of the non-radiative loss mechanisms for the application as photoanode was analyzed [23]. By now, studies that examine both processes simultaneously have not been reported, yet. With the comparison of bias-dependent photocurrent, photoluminescence and electron spin resonance spectroscopy measurements [24], the importance of using multiple methods for the comprehension of the different processes was demonstrated for the first time. However, further research to gain insights in the detailed reaction is needed.

In the present work, the optically activated detection of ascorbic acid, uric acid and hydrogen peroxide with InGaN/GaN NWHs by simultaneous PL and PC measurements is demonstrated. Without any surface modification, the detection of the biomolecules is realized by the adjustment of the working point and a distinct PL and PC response.

Another approach is presented in the following section of the chapter. Photo-induced electron transfer processes are studied by the investigation of donor-acceptor (D-A) linked frameworks covalently linked to the GaN NW surfaces. The charge-induced PL and PC were analyzed which demonstrated a unique characteristic in presence of the charge separation state. The well-defined conditions supplied by GaN NWs in the electrochemical environment allowed to determine the charge transfer paths and to correlate the phenomena in this chapter.

Besides monitoring of PL and PC to investigate the charge transfer as such, the (bio-)chemical detection can be extended towards a quantification of pH-induced changes providing spatial resolution. The nanowires individually probe pH changes that are caused by intracellular processes and can therefore locally detect changes in pH/bias in the surrounding medium. By the use of InGaN/GaN NWHs as optochemical electrodes in combination with a standard microscope setup the dynamic bioimaging of cell activity is demonstrated in the last part if this work.

Chapter 2

Fundamentals

In the following chapter the fundamental concepts and mechanisms are introduced to understand the investigations and results of this work. First of all, the properties of the investigated samples, InGaN/GaN nanowire heterostructures and GaN NWs, are specified. Then, the techniques of photoluminescence (PL) and photocurrent (PC) measurements in electrolyte solutions are presented where the influence of bias voltage and pH are examined in more detail.

2.1 Preparation and Characterization of GaN Nanowires and InGaN/GaN Nanowire Heterostructures

In this section, the structures of the GaN nanowires and InGaN/GaN nanowire heterostructures are presented and the growth details are described.

2.1.1 GaN Nanowires

Not-intentionally-doped (n.i.d.) GaN NWs were grown in a self-assembled mode on conductive n-type silicon(Si)(111) substrates (As-doped, $\rho < 0.01\,\Omega$cm) by plasma-assisted molecular beam epitaxy ("RIBER Compact 12 system", Riber, Bezons, France) under nitrogen-rich conditions [25]. The growth of GaN NWs in wurtzite structure is along the $[000\overline{1}]$ direction [26]. The growth process is catalyst-free [25].
Before the growth process, the native oxide layer of the substrates is removed by wet chemical etching with buffered hydrofluoric acid. After nitridation of the Si surface, the GaN base growth is initiated. Details on the growth process are described in references [25, 27]. GaN NWs were grown at a substrate temperature of $\vartheta_{\text{substrate}} \approx 760\,^{\circ}$C. The GaN NW growth proceeded at a nitrogen plasma power of $P_{\text{N}_2} = 300\,$W and at a nitrogen flux of $\Phi_{\text{N}_2} = 1.0\,$sccm.
For the characterization of the nanowire morphology, scanning electron microscope (SEM) images were taken using a SEM of type "JSM-7001F" (JEOL Ltd., Tokyo, Japan). The acceleration voltage was $U_{\text{acc}} = 15\,$kV and the emission current was $I_{\text{em}} = 50\,\mu$A. SEM images

of GaN NWs in side view and in top view are shown in figure 2.1.

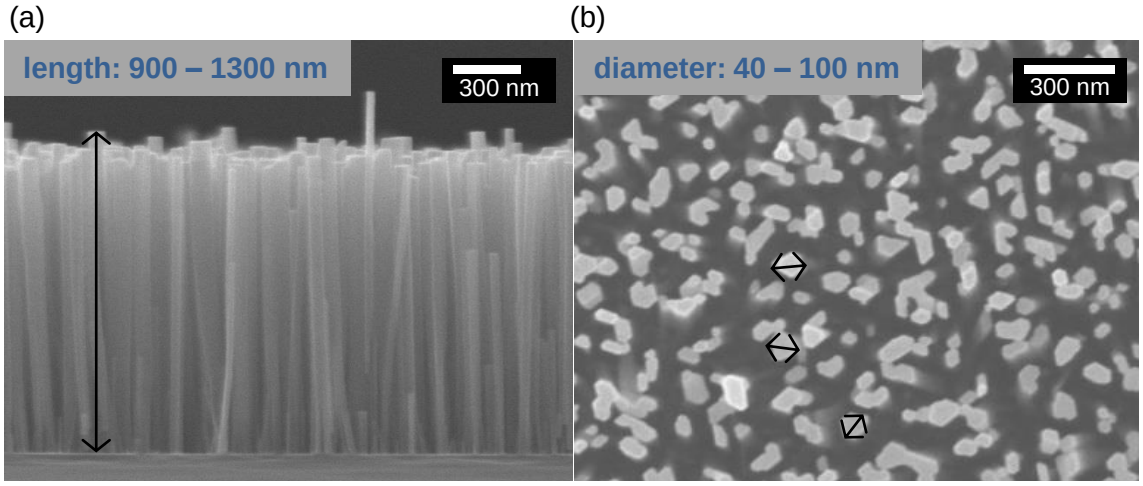

Figure 2.1: SEM images of GaN NWs in (a) side and (b) in top view.

The investigated GaN NWs possess a length of $l_{\mathrm{NW}} = 900\text{-}1300\,\mathrm{nm}$ and a diameter that ranges from $d_{\mathrm{NW}} = 40\text{-}100\,\mathrm{nm}$. A detailed structural analysis of GaN NWs as well as an optical characterization of GaN NWs are reported in ref. [25].
The band gap of GaN is $E_{\mathrm{gap}}(\mathrm{GaN}) = 3.41\,\mathrm{eV}$. For photoluminescence measurements, a HeCd laser with an excitation wavelength of $\lambda_{\mathrm{exc}} = 325\,\mathrm{nm}$ for above band gap excitation is used. The room temperature PL spectrum of GaN NWs in atmosphere is shown in figure 2.2 (blue curve). The PL intensity is normalized to the maximum intensity.

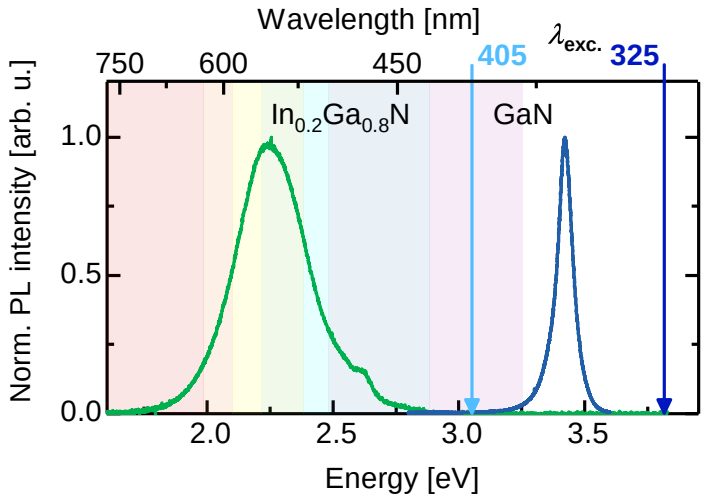

Figure 2.2: Normalized room temperature photoluminescence spectra of an InGaN/GaN nanowire heterostructure (green line) and of the GaN nanowire template (blue line) in atmosphere. InGaN/GaN NWHs were excited with a laserdiode of $\lambda_{\mathrm{exc}} = 405\,\mathrm{nm}$ and for GaN NWs (template for InGaN/GaN NWHs) the excitation wavelength is $\lambda_{\mathrm{exc}} = 325\,\mathrm{nm}$.

The room temperature PL spectrum of GaN NWs is dominated by the near-band edge recombination of GaN at $E_{\mathrm{gap}}(\mathrm{GaN}) = 3.41\,\mathrm{eV}$. Additionally, for measurements in aqueous electrolytes, the excitation with ultraviolet (UV) light results in a luminescence of water

from the aqueous electrolyte. Pure water is reported to possess an intrinsic luminescence at an energy of $E_{\mathrm{water,max}} = 3.4\,\mathrm{eV}$ [28]. Thus, the intrinsic water luminescence is in the same energy region as the GaN PL at room temperature. While the water luminescence results in a constant PL contribution, the GaN PL intensity is bias-dependent. In the experiments, the applied bias voltage is chosen to be in the high cathodic range ($U_{\mathrm{C}} \gg U_{\mathrm{OCP}}$) which minimizes the influence of the water luminescence.

2.1.2 InGaN/GaN Nanowire Heterostructures

Self-assembled and not-intentionally-doped (n.i.d.) $In_xGa_{1-x}N$/GaN nanowire heterostructures (InGaN/GaN NWHs) are grown on low resistivity n-type Si(111) substrates (As-doped, $\rho < 0.01\,\Omega\mathrm{cm}$) by plasma-assissted molecular beam epitaxy ("RIBER Compact 12 system", Riber, Bezons, France) using nitrogen-rich conditions [25]. Typically, the total lengths of the NHWs are $l_{\mathrm{NWH}} = 600$ - $1000\,\mathrm{nm}$ and the average diameters amount to $d_{\mathrm{NWH}} = 50$ - $90\,\mathrm{nm}$. The InGaN/GaN NWHs comprise a GaN base which is followed by an InGaN part. The nominal lengths are $l_{\mathrm{NW}}(\mathrm{GaN}) \approx 250\,\mathrm{nm}$ and $l_{\mathrm{NW}}(\mathrm{InGaN}) \approx 350\,\mathrm{nm}$, respectively. The schematic presentation of the nanowire sample structure and a transmission electron microscope (TEM) image [1] are displayed in figure 2.3.

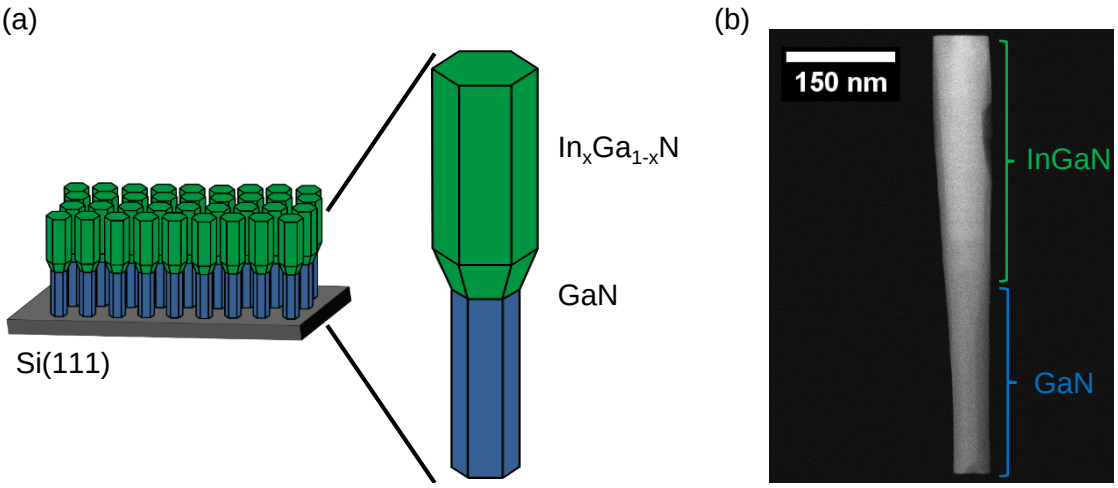

Figure 2.3: (a) Schematic presentation of InGaN/GaN NWHs and (b) TEM image of InGaN/GaN NWH in side view. The InGaN part is longer than the GaN base.

The native oxide layer of the substrates is removed by wet chemical etching in buffered hydrofluoric acid before growth. The growth process starts with the nitridation of the Si surface. Next, the GaN base growth is initiated which serves as a template for the InGaN NW growth. Details on the growth process of the GaN base are described in refs. [25, 27]. The GaN growth proceeds at a substrate temperature of $v_{\mathrm{substrate}}(\mathrm{GaN}) \approx 720\,^{\circ}\mathrm{C}$. Then, the substrate temperature is reduced to $v_{\mathrm{substrate}}(\mathrm{InGaN}) = 500\,^{\circ}\mathrm{C}$ to initiate the InGaN growth. The growth procedure and the structural analysis of the heterostructures are reported in refs. [25, 29]. Just as the GaN NWs, InGaN/GaN NWHs possess wurtzite

[1] The TEM image was taken by Katharina Gries from the group of Prof. Kerstin Volz (Faculty of Physics and Materials Science Center, Philipps-Universität, Marburg, Germany).

structure and are grown along the [000$\bar{1}$] direction.
The InGaN part is grown at $P_{N_2} = 300\,\mathrm{W}$ and $\Phi_{N_2} = 1.6\,\mathrm{sccm}$. For $\Phi_{N_2} > 0.8\,\mathrm{sccm}$ the introduction of semi-polar facets on the nanowire side walls is reported. This decreases the area of polar surfaces [25].
In figure 2.4 SEM images of the resulting InGaN/GaN NWHs in side view and in top view are displayed. The images were taken using a SEM of type "JSM-7001F" (JEOL Ltd., Tokyo, Japan). The settings were $U_{acc} = 15\,\mathrm{kV}$ and $I_{em} = 50\,\mu\mathrm{A}$.

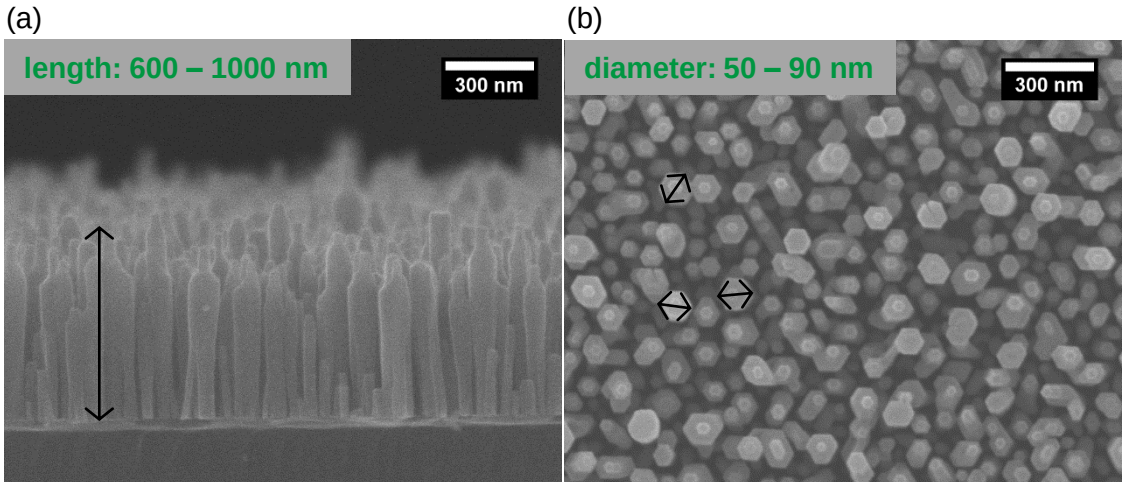

Figure 2.4: SEM of InGaN/GaN NWHs in (a) side and (b) in top view.

The In distribution along the growth direction is inhomogeneous. The concentration of indium is higher at the tip of the nanowire [25, 30, 31]. InN and GaN have a large lattice mismatch that results in internal elastic strain during deposition. As a consequence, this mismatch strain constrains the In incoporation into the NW so that the composition of the growing InGaN NW aligns the GaN substrate composition ("lattice pulling effect") [32]. Additionally, the indium content is increased at semi-polar side facets since the occupation of In adatoms preferentially occurs at low coordination sites which are present at these side facets [25, 33].
In contrast to GaN NWs, InGaN NWHs can be excited with a laserdiode of $\lambda_{exc} = 405\,\mathrm{nm}$ which is in the visible spectrum of light. This is important for biological applications since the lower excitation energy prevents the dissociation of the investigated biomolecules. By variation of the indium content, the excitation wavelength and the emission wavelength can be adjusted.
The room temperature PL spectrum of the InGaN/GaN NWHs in atmosphere is shown in green in figure 2.2 next to the PL spectrum of the GaN base (blue curve). InGaN NWHs possess a sufficient optical PL intensity that is detectable at room temperature [33]. The InGaN PL spectrum shows a broad intensity distribution from $E_{em} = 1.8\text{-}2.9\,\mathrm{eV}$ with its maximum at $E_{em,max} \approx 2.3\,\mathrm{eV}$. With $E_{em,max} = 2.3\,\mathrm{eV}$, the In content was calculated to $\mathrm{x} = 31\,\%$ according to ref. [34]. In contrast, the In content from X-ray diffraction measurements was estimated to $\mathrm{x} = 10\,\%$. This indicates an inhomogeneous In distribution along the nanowire with local accumulations of indium which define the PL transitions energies [33]. The inhomogeneous Indium distribution within one single NW resulting

from axial [31,35,36] and radial [37] deviations as well as wire-to-wire fluctuations of the NW ensembles [38] were reported accounting for the broad emission of the InGaN peak.

2.2 Photoelectrochemical Characterization

For photoelectrochemical characterization, the group III-nitride NWs are used as working electrodes (WEs) in a three-electrode setup. In this section, the measurement cell is described and the photoelectrochemical properties of the electrodes are presented.

2.2.1 Measurement Cell

A conventional three-electrode setup was used for the photoelectrochemical measurements. The setup allows of the application of an external bias to define the electrode´s potential and thus, to adjust the working point of the sample [12]. The NW sample serves as working electrode, a small platinum tube serves as counter electrode (CE) and an Ag/AgCl (3 M KCl) reference electrode (RE) is used. The native oxide layer on the backside of the silicon substrate was removed by wet-chemical etching in buffered hydrofluoric acid solution. Then, Ohmic contacts (80 nm aluminum(Al)/100 nm silver(Ag)) were deposited onto the Si substrate by thermal evaporation. The externally applied bias potentials refer to the Ag/AgCl reference electrode and are denoted as cathodic bias voltages U_C. The constant exchange of the electrolyte solution is ensured by the use of a peristaltic pump "Perimax 12" (Spetec GmbH, Erding, Germany). The speed of the electrolyte solution was set to $v_{\text{pump}} = 4.84\,\text{ml/min}$.
The schematic presentation of the measurement flow chamber for photoelectrochemical characterization is shown in figure 2.5.

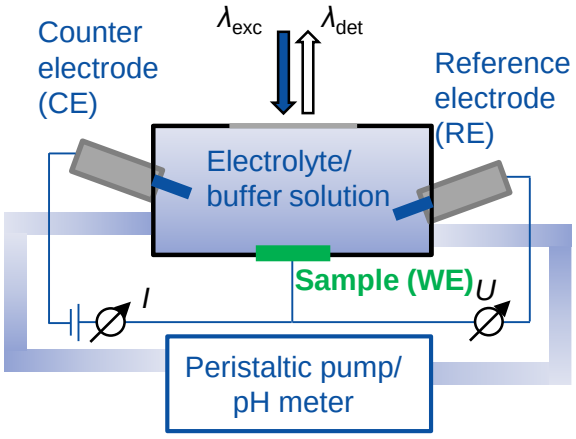

Figure 2.5: Schematic presentation of the measurement flow chamber for photoelectrochemical characterization.

The external bias was applied using a potentiostat of type "Wenking LB 81M" (Bank Elektronik GmbH, Giessen, Germany). As external voltage source, a sourcemeter ("sourcemeter 2400", Keithley Instruments Inc., Cleveland, U.S.A.) was connected to the potentiostat.

The current was detected with a multimeter ("multimeter 2700", Keithley Instruments Inc., Cleveland, U.S.A.). The presented current densities are calculated by the division of the current by active area of the electrode A which is determined by the silicon ring used for sealing and calculated to $A = 0.07\,\mathrm{cm}^2$.
Standard measurement procedures imply the use of 10 mM phosphate buffered saline (PBS) solution. For experiments with biological substances 100 mM 4-(2-hydroxyethyl)-1-piperazineethanesulfonic acid (HEPES) buffer solution is used which is commonly applied in cell culture. The acid dissociation constant of HEPES solution at $\vartheta = 25\,°\mathrm{C}$ amounts to $\mathrm{pK_a} = 7.45$ - 7.65. Its buffer effect is in the range of $\mathrm{pH} = 6.8$ - 8.2 [2]. The HEPES buffer solution was adjusted to $\mathrm{pH} = 7$ if not stated otherwise.
The pH of the solutions was adjusted with sodium hydroxide and hydrochloric acid. The pH was measured using a pH meter "Seven Multi" (Mettler Toledo GmbH, Schwerzenbach, Switzerland). This two-channel measuring device also enabled the measurement of the conductivity of the solutions for the experiments. Both the pH and the conductivity σ of the different solutions were monitored to exclude their influence on the obtained results.

2.2.2 Photoelectrochemical Properties

The photoelectrochemical properties are exemplary demonstrated with InGaN/GaN NWH electrodes using the experimental setup described in section 3.2.1.
The photoelectrochemical properties of the NW electrodes were investigated by the simultaneous measurement of the photoluminescence (PL) intensity and the photocurrent (PC). The PL intensity is the radiative recombination after photoexcitation with above band gap energy ($E_{\mathrm{exc}} > E_{\mathrm{gap}}$). After photoexcitation, the photo-generated electron-hole pairs thermalize to the ground state and recombine as photons. By photocurrent analysis, the non-radiative charge transfer of photo-excited holes from the nanowire electrode into the electrolyte solution can be studied.
Both GaN NWs and InGaN/GaN NWHs possess n-type behavior due to an unintentional n-type doping. This doping is based on silicon atoms on gallium sites and/or oxygen atoms that are on nitrogen sites [25]. For open circuit potential conditions, the n-type GaN NW and InGaN/GaN NWH samples show an upward surface band bending (SBB) (cf. section 3.1). The result is a charge carrier separation of minority (holes) and majority carriers (electrons) according to the "dead-layer-model" (cf. ref. [39]). Photo-generated electrons stay within the nanowire centre. In contrast, photo-generated holes are accumulated at the surface. The large density of near-surface holes allows the amplified non-radiative processes such as electron transfer into the electrolyte solution or the recombination via surface states. On the contrary, the radiative recombination rate, that also depends on the minority carrier density [24], is low.
Without external bias application the photocurrent density is high compared to the PL intensity due to enhanced non-radiative processes. The surface band bending of the elec-

[2] https://www.carlroth.com/downloads/allgemein/de/Infobroschuere_BiologischePuffer_DE.pdf, 06.07.2018

trode can be altered by applying an external bias voltage. As a consequence, the ratio of radiative and non-radiative recombinations is shifted. The photocurrent increases with the application of an anodic bias voltage U_A. The PL intensity increases with the application of a cathodic bias voltage U_C. The PL intensity and the PC density of InGaN/GaN NWHs in dependence of the external bias voltage U_C are shown in figure 2.6.

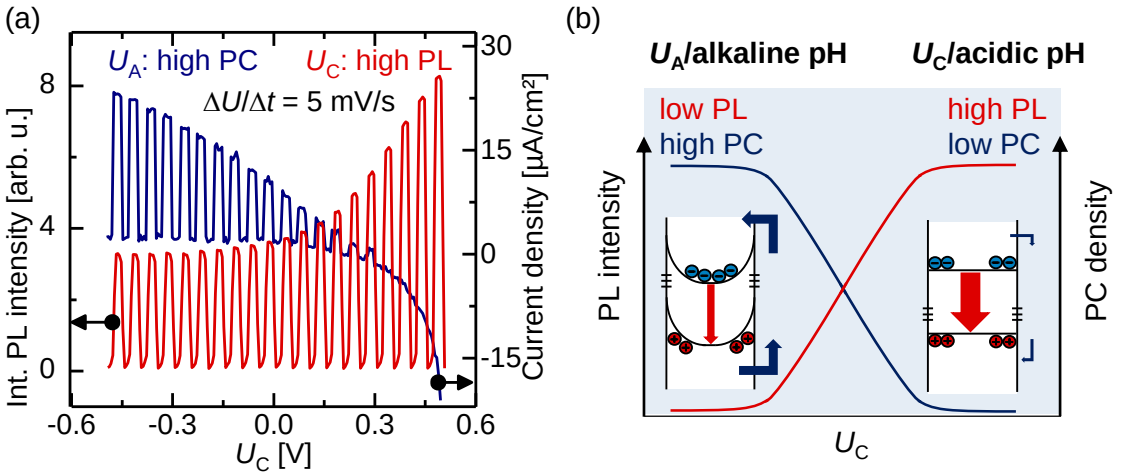

Figure 2.6: (a) Chopped light voltammetry with a bias voltage change of $\Delta U_C/\Delta t = 5\,\mathrm{mV/s}$. The current density and the PL intensity were simultaneously measured. The PC increases with anodic bias voltages U_A. The PL intensity increases with cathodic bias voltages U_C. (b) Schematic presentation of bias and pH dependence of PL and PC.

The PL intensity and the PC were measured simultaneously in dependence of U_C. The bias voltage was sweeped with $\Delta U_C/\Delta t = 5\,\mathrm{mV/s}$. The chopping of the excitation source allows for quantification and differentiation of the dark current and the photocurrent in the same measurement procedure.

In the anodic bias range (U_A, figure 2.6(a)) the photocurrent increases with increasing U_A. In contrast, the PL intensity decreases with increasing U_A. At U_A, the upward SBB is increased (cf. figure 2.6(b)) and the separation of photo-generated electron-hole pairs is enhanced. Thus, non-radiative recombinations due to hole transfer into the redox level of the molecules increase [24]. The minority carriers that determine the PL intensity are reduced so that the PL intensity is decreased. For increasing cathodic bias voltage U_C to voltages above the open circuit potential, the upward surface band bending decreases. When the applied bias potential reaches the flat band conditions $U_C = U_{\text{flat band}}$, the hole transfer into the electrolyte solution is quenched due to a reduction of near-surface accumulated minority carriers and the PL intensity increases [24]. In this process, the energy barrier for electrons at the NW surface for transfer into the electrolyte is reduced. The PL intensity is not affected by the electron transfer into the electrolyte solution. For increasing U_C, the number of minority carriers in the bulk is increased. As a result the PL intensity is strongly enhanced. In contrast to the PL intensity, the majority carriers add to the total current density. This becomes apparent for $U_C > 0.3\,\mathrm{V}$ in figure 2.6(a). At high U_C, a cathodic PC can be measured which increases with increasing U_C [24].

In addition to the bias dependence, the PL intensity of group III-nitride NWs depends on the solution pH [12], which can be explained based on the site-binding model for metal-oxide surfaces [40]. The GaN and InGaN surfaces, such as many semiconductor materials, possess a thin native oxide layer in atmosphere [41, 42]. In the site-binding model, the hydroxylated surface sites allow for protonation and deprotonation. A deprotonation of the hydroxylated surface for high pH values results in negatively charged surface sites, whereas protonation at low pH leads to positively charged ones. As a consequence, the pH-dependent surface charge alters the SBB. A positive surface charge is comparable to the application of external U_C. The negative surface charge is analogous to the application of external U_A. The pH dependence of the PL intensity of group III-nitride NWs is exemplary shown for InGaN/GaN NWHs in figure 2.7.

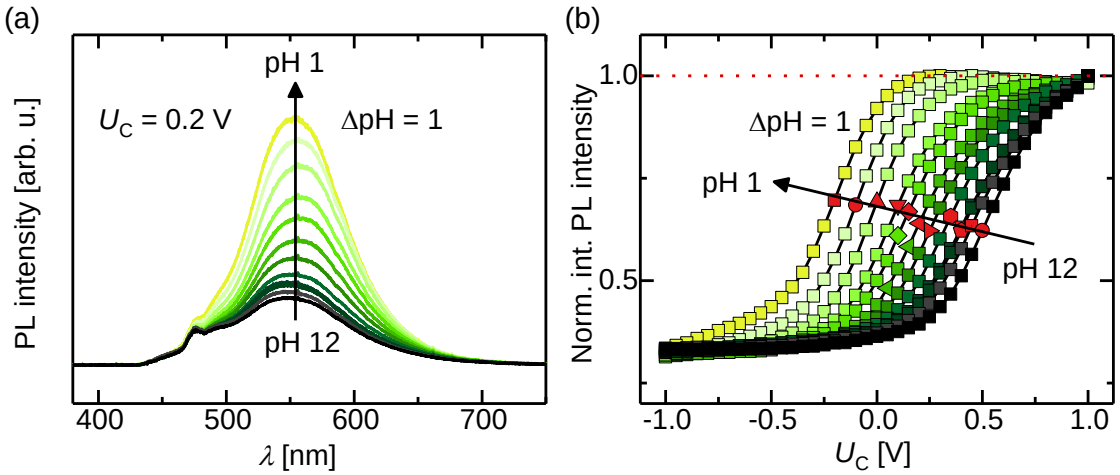

Figure 2.7: (a) PL spectra of InGaN/GaN NWHs in a 10 mM PBS solution at $U_C = 0.2$ V for different pH. The PL intensity increases for increasing pH from pH = 12 to pH = 1. (b) Normalized integrated (norm. int.) PL intensity of InGaN/GaN NWHs in dependence of U_C for different pH. The working points of the NW electrode are indicated in red. The excitation wavelength was $\lambda_{exc} = 405$ nm.

The pH dependence can be attributed to a modification of the effective SBB. The positive surface charge results in a reduction of the upward SBB. As a result, the PL intensity increases. The pH and bias dependences (cf. figure 2.7(b)) show an S-shape behavior which shifts to the anodic direction for acidification of the solution. The calibration curves can be used to determine the working point (= inflection point) with the highest sensitivity of the PL intensity (or PC density) to pH or bias changes. The inflection points of the different curves are marked in red. Application of the respective bias potentials results in the maximum bias and pH resolution referring to PL intensity or PC density. The PL sensitivity of InGaN/GaN NHWs is 80 mV/pH for neutral to alkaline solutions and 120 mV/pH for acidic solutions. This corresponds to a pH resolution of ΔpH = 0.008 - 0.0125 for a bias change of $\Delta U = 1$ mV.

In combination, the PC density and the PL intensity in dependence of the external bias voltage and the solution pH are shown in figure 2.8 for an InGaN/GaN NWH electrode. The data points were extracted from transient measurements which explains the difference

to the curve shape in figure 2.7(b).

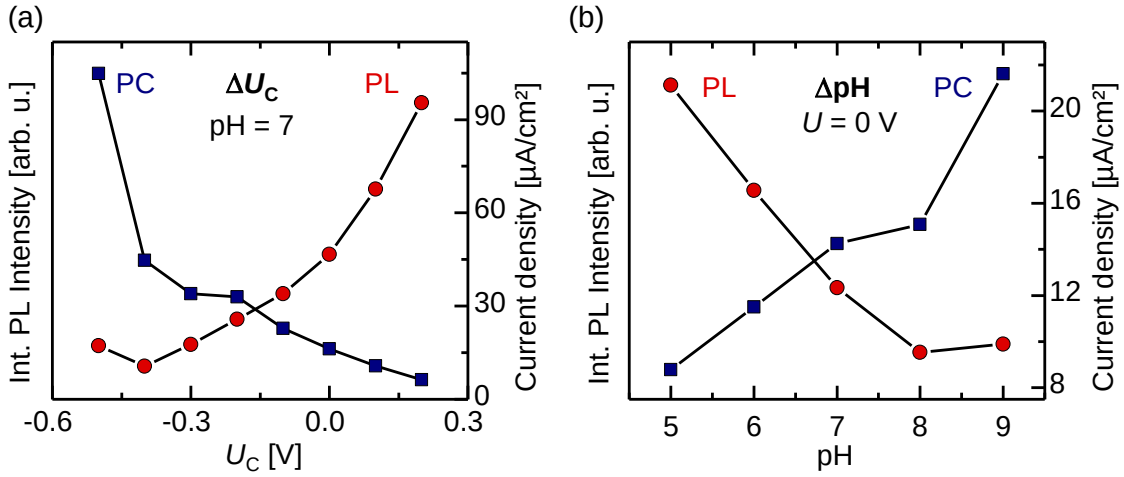

Figure 2.8: Integrated PL intensity and current density for (a) different bias voltages at pH = 7 and (b) different pH values at $U = 0\,\mathrm{V}$. The values were extracted from transient measurements after a 10 min interval each. For the measurement 100 mM HEPES solution was used and the speed of the electrolyte solution was $v_{\mathrm{pump}} = 2.78\,\mathrm{ml/min}$.

The adjustment of the bias potential allows to operate the group III-nitride NW electrodes as anode or as cathode. Here, the photocurrent or the PL intensity can independently serve as a detection signal. Otherwise, these electrodes provide the advantage of simultaneously measuring the photoluminescence intensity and the current density. This enables the quantification of radiative as well as a non-radiative processes and directs to a better understanding of the charge transfer processes within the nanowire electrodes.
The application of GaN NWs and InGaN/GaN NWHs as sensor electrodes in electrolyte solution requires specific conditions. The GaN NW electrodes allow operation in the cathodic bias range. For anodic bias, the oxidation of the NW surface was observed [24]. The GaN surface is oxidized according to [24]

$$2\,\mathrm{GaN} + 6\,\mathrm{h^+} + 6\,\mathrm{OH^-} \rightleftharpoons \mathrm{Ga_2O_3} + 3\,\mathrm{H_2O} + \mathrm{N_2}. \tag{2.1}$$

The use of basic solutions (pH > 8) results in an ablation of the GaN NWs [12]. As a consequence, the use of GaN NW electrodes is limited to the application of U_{C} at neutral to acidic pH.
For InGaN/GaN NWH electrodes a photoelectrochemical oxidation at anodic bias voltages is reported [43]. At pH = 7.4, the oxide is mainly composed of Ga-O bonds, while at alkaline pH (pH = 11.3) In-O bonds are dominating [43]. This oxidation process continues up to a certain critical oxide thickness ("$d_{\mathrm{ox,critical}}$"). During oxidation, the PC density decreases, and finally saturates [23]. Hence, InGaN/GaN NWH electrodes can be applied in both bias ranges and independent from the solution pH.
Typically, the photocurrent shows an overshoot upon illumination as it is shown in figure 2.9.

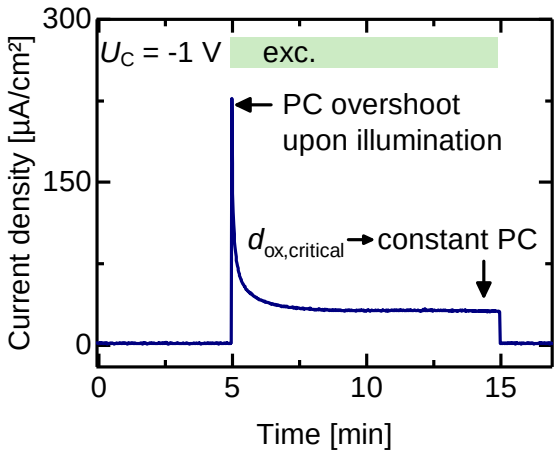

Figure 2.9: Photocurrent overshoot upon illumination of InGaN/GaN NWHs. After a subsequent decay, a steady photocurrent is obtained.

This general feature is observed for almost all electrodes based on semiconductor nanowires. The overshoot is a result of the flow of near-surface minority carriers into the electrolyte solution [44]. The subsequent decay is caused by the recombination of built-in minority carriers that are trapped in surface states and recombine with majorities [44].

Chapter 3

Detection of Charge Transfer Processes at the Electrode/Electrolyte Interface with GaN NWs and InGaN/GaN NWHs

GaN NWs and InGaN/GaN NWHs can be excited with above band gap energy resulting in a transfer of photo-generated charge carriers between the NWs and the electrolyte solution. For such three-dimensional materials, the mechanisms are analogous to those of two-dimensional semiconductor materials, with an enhanced surface-to-volume ratio. Hence, such surface transfer reactions are more significant.

In the first section of this chapter charge transfer processes between semiconductor materials and electrolyte solutions are discussed in general.

In the following section, the charge transfer processes between InGaN/GaN NWH electrodes and redox biomolecules in the electrolyte solution were investigated. Here, these transfers enable the detection of uric and ascorbic acid (UA and AA) as well as of hydrogen peroxide (H_2O_2) in solution. Since the PL and PC of InGaN/GaN NWHs can be excited with light of the visible spectrum, the activities of biomolecules are maintained during the detection process. The detection is achieved by simultaneous measurements of the PL intensity and the PC and the operation of the NWH electrode as photoanode and photocathode in an electrochemically well-defined working point.

In the second part of this chapter, a novel photoresponsive material system consisting of GaN NW electrodes chemically modified with triad molecules is presented and assessed. The charge transfer mechanism is investigated by simultaneous measurements of the GaN PL intensity and current density modulations by the supplementary excitation of the photoactive units of these triad molecules. The charge transfer processes are based on the appropriate band alignment of conduction and valence band edges of GaN and the redox levels of the triad molecules.

3.1 Charge Transfer Mechanisms Between Semiconductor/ Electrolyte Interfaces

In this paragraph, the charge transfer between InGaN/GaN NWHs or GaN NWs and the electrolyte solution is described based on the physics of semiconductor/liquid interfaces.

In general, most semiconductors in gaseous atmosphere possess surface states within the band gap. For n-type semiconductors, such as the group III-nitride NWs investigated here (cf. ref. [25]), electrons are transferred from the conduction band to the surface states. These negatively charged surface states generate an electric potential that causes an upward surface band bending (SBB). This is shown in a schematic presentation of the SBB with the development of the open circuit potential after photoexcitation (OCP_{photo}) in figure 3.1.

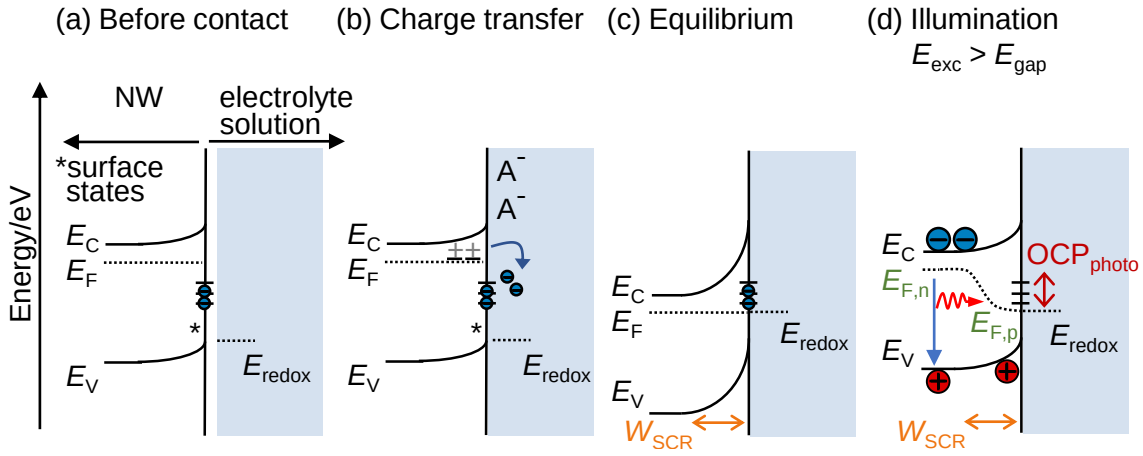

Figure 3.1: Schematic presentation of the surface band bending and the development of the open circuit potential after photoexcitation. E_V is the valence band energy, E_C is the conduction band energy, E_F represents the Fermi level, E_{redox} is the potential of the redox couple of the electrolyte solution and W_{SCR} is the depletion width.

The SBB describes the modulation of the band edge positions close to the surface. In the bulk of the semiconductor, the valence band and the conduction band remain unaltered. Between the modulated band edges at the surface and the bulk the space charge region (SCR) is formed. The extension of the SCR is described by the depletion width W_{SCR}.
In general, the electrical properties of the semiconductor/electrolyte interface are characterized in analogy to a Schottky contact [45, 46]. The SBB for group III-nitride NWs in contact with liquid interfaces, where redox couples are present, can be described by the "extended dead-layer-model" (for details cf. ref. [12]). Electrons are transferred from the energetically higher level, mainly the conduction band level, to the energetically lower level, the redox level of the liquid until equilibration of the electrochemical potential. Thus, the semiconductor possesses an excess positive charge due to the ionized donors that remain. On the contrary, the liquid exhibits an excess negative charge. Consequently, the negatively charged molecules accumulate at the NW surface (A^-, cf. figure 3.1(b)). As a result, the upward surface band bending increases. During this process, an internal electric

field is established which compensates the electric potential differences of the Fermi level and redox potential until their energetic alignment [47].
In the absence of an external electric field and without illumination, this potential can be measured with reference to the potential of the reference electrode and is often termed "open circuit potential in dark conditions". Under illumination, a true equilibrium cannot be reached. This is only possible in dark conditions where one Fermi level respresents the statistical distribution of minority and majority carriers [47]. For non-equilibrium conditions, the energetic levels of minority and majority carriers are individually described as hole and electron quasi-Fermi levels, respectively [47]. The difference of the latter is termed "open circuit potential/voltage after photoexcitation" (OCP_{photo}) [47] (cf. figure 3.1(d)) and is calculated as the difference of the OCP determined after illumination and in dark. The current/voltage (I/V) characteristic of a semiconductor/electrolyte interface can be described similar to that of a Schottky contact. The potential difference between the redox potential and the conduction band edge at the interface is the analogy for the barrier height φ_B of a Schottky contact. The schematic presentation of a Schottky contact and the I/V characteristics for dark conditions and after photoexcitation are shown in figure 3.2.

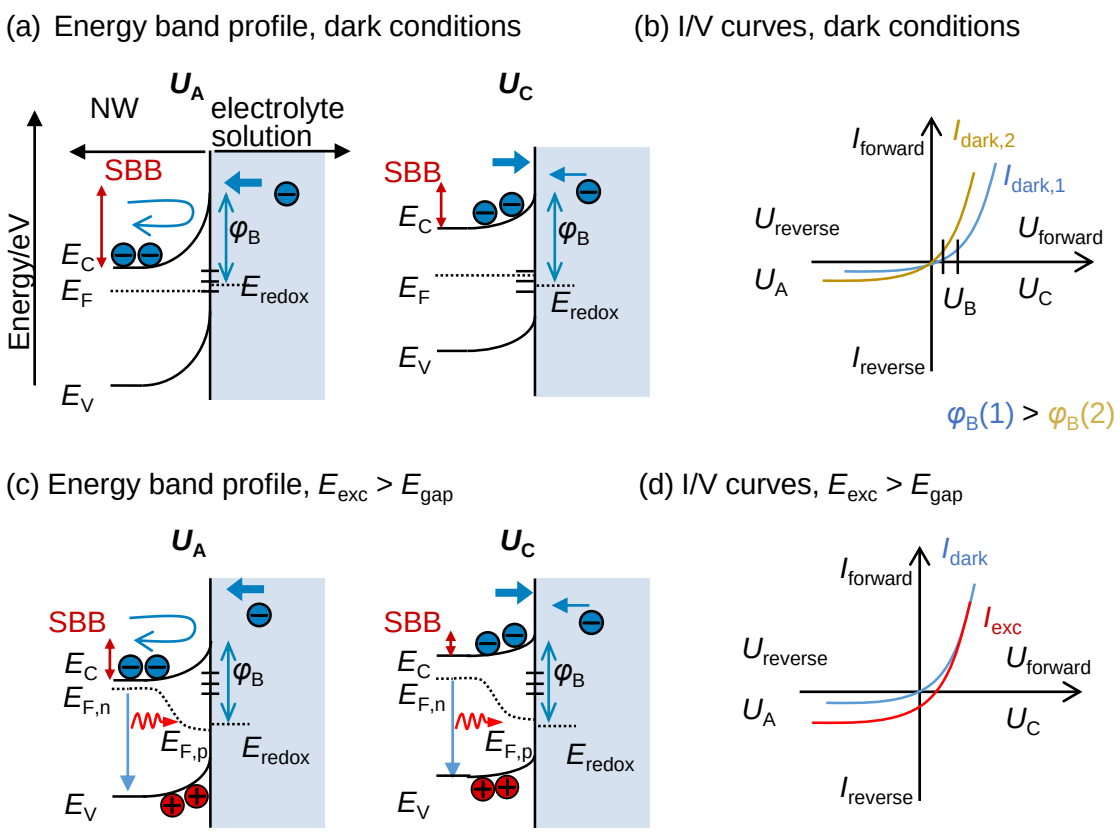

Figure 3.2: Schematic presentation of the semiconductor/electrolyte interface in analogy to a Schottky contact. The energy band profiles with external bias for (a) dark conditions and (c) above band gap excitation are shown. The related I/V characteristics are presented for (b) dark conditions and (d) above band gap excitation. E_V is the valence band energy, E_C is the conduction band energy and E_F is the Fermi level. The surface band bending (SBB) and the barrier height φ_B are indicated.

For dark conditions, the application of an anodic (cathodic) bias corresponds to the reverse bias U_{reverse} (forward bias U_{forward}) of a Schottky contact. The most dominant process of current transport across a Schottky contact in forward direction is the thermionic emission. The transport via diffusion or tunnelling can be neglected since their contributions are usually small compared to that of the thermionic emission. The current flow is the total dark current from electrons transferred from the semiconductor into the electrolyte $I_{\text{s-e}}$ reduced by the current of electrons transferred from the electrolyte into the semiconductor $I_{\text{e-s}}$

$$I_{\text{dark}} = I_{\text{s-e}} - I_{\text{e-s}}. \tag{3.1}$$

With the current density of the thermionic emission $j_{\text{thermionic}}$ described by the Richardson equation

$$j_{\text{thermionic}} = \mathrm{A_R} \cdot T^2 \cdot \exp\left(\frac{\mathrm{e}\,\varphi_{\mathrm{B}}}{\mathrm{k_B}\,T}\right) \tag{3.2}$$

with the Richardson constant $\mathrm{A_R} = 1.2 \cdot 10^6\,\mathrm{A/m^2K^2}$, the temperature T, the elementary charge e, the Boltzmann constant $\mathrm{k_B}$ and the barrier height φ_{B}, the total current density in dark is

$$j_{\text{dark}} = \mathrm{A_R} \cdot T^2 \cdot \exp\left(\frac{-(\varphi_{\mathrm{B}} - \mathrm{e}\,U)}{\mathrm{k_B}\,T}\right) - \mathrm{A_R} \cdot T^2 \cdot \exp\left(\frac{-\varphi_{\mathrm{B}}}{\mathrm{k_B}\,T}\right) \tag{3.3}$$

$$j_{\text{dark}} = \mathrm{A_R} \cdot T^2 \cdot \exp\left(\frac{-\varphi_{\mathrm{B}}}{\mathrm{k_B}\,T}\right) \cdot \left[\exp\left(\frac{\mathrm{e}\,U}{\mathrm{k_B}\,T}\right) - 1\right]$$

$$j_{\text{total}} = j_0 \cdot \left[\exp\left(\frac{\mathrm{e}\,U}{\mathrm{k_B}\,T}\right) - 1\right]. \tag{3.4}$$

The I/V characteristic for dark conditions can be altered by the modulation of the barrier height (cf. figure 3.2(c)). A decrease of the barrier height results in an increase of the current in forward and particularly in reverse direction. The barrier height is mainly determined by the redox potential of the electrolyte as well as density and energy of the surface states. A negative charge at the interface increases the barrier height whereas a positive charge reduces the height. The modulation of φ_{B} effect can be induced by surface charge due to ion adsorption or changes in the occupation number of surface states, respectively. In figure 3.3, this modulation is schematically shown for a reduction of a negative surface charge.

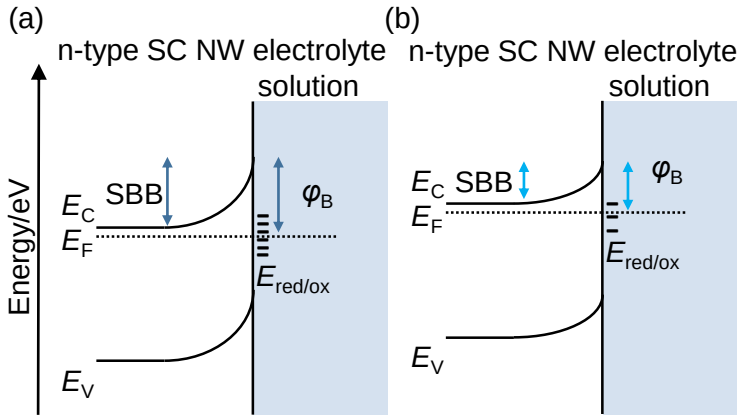

Figure 3.3: Schematic presentation of tuning the semiconductor SBB and the barrier height by the reduction of surface charges from (a) to (b).

The reduction of the negative surface charge, as it is the case for n-type semiconductors, decreases the SBB and the barrier height. In contrast, the increase of the negative surface charge results in an increase of both the SBB and the barrier height.
By photoexcitation of photoactive molecules immobilized on semiconductor surfaces, electrons are transferred withing the molecules and thus, resulting in a charge-separation state. This formation of stationary dipoles or surface charges at the semiconductor/electrolyte interface leads to a change of the effective barrier height. The induction of negative (positive) surface charges increases (decreases) the barrier height.

Photoexcitation of the Schottky contact region results in photogeneration of electron-hole pairs and thus, an increase of the current magnitude. The total current is given by the majority carrier current (thermionic emission) and the minority carrier current [48]. The current of the minority carriers is proportional to the photon flux [48]. This result in a net current density of

$$j_{\text{photo}} = j_{\text{ph}} + j_0 \cdot \left[\exp\left(\frac{\mathrm{e}\,U}{\mathrm{k}_B\,T} \right) - 1 \right] \text{ [48]} \tag{3.5}$$

where j_{ph} is the current density generated by the photon flux.

The current density under photoexcitation is a shift of the dark current I/V characteristic by the offset of the current generated by the photon flux and the electric field caused by the presence of the energy barrier (cf. figure 3.2(d)). The anodic current increases (anodic photocurrent generation) and for cathodic potentials the majority carrier current is prominent.

Photo-excited carriers can recombine radiatively or non-radiatively. In general, five different recombination mechanisms are possible and are summarized in figure 3.4 according to ref. [47].

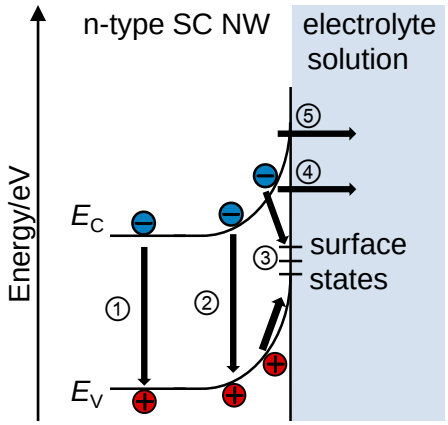

Figure 3.4: Recombination pathways for photo-excited carriers in presence of a liquid interface without surface passivation according to ref. [47]. The numbers correlate to the items listed below.

The recombination processes are divided into radiative and non-radiative pathways:

- **Radiative recombination pathways**

  (1) Recombination in the bulk

  (2) Recombination in the space charge region (less likely)

- **Non-radiative recombination pathways**

  (3) Recombination of an electron with a hole at defects (surface states for example)

  (4) Tunneling across the surface

  (5) Thermionic emission

An external bias can be applied to study these charge transfer mechanisms as it alters the surface band bending. This can either result in an enhancement or in a decrease of the upward SBB for the case of anodic bias (U_A, reverse bias) or cathodic bias (U_C, forward bias), respectively. The radiative processes can be investigated by measuring the PL intensity of the NW samples, with the charge transfer across the semiconductor interface into the electrolyte solution being simultaneously monitored by PC measurements (cf. section 2.2). With the use of electron spin resonance (ESR) spectroscopy as an additional measurement method, the transferred charge mechanisms can be ascribed to minority or majority carriers [24]. The PL intensity shows an S-shape behavior as a function of U_C [12], whereas the PC exhibits an inverse S-shape behavior (cf. figure 2.6(b)). In the present case, the PL intensity and the PC are mainly affected by the minority carriers [24].
The modulation of photo-generated charge carriers at the NW surface can be used to detect (bio-) chemical processes that are accompanied by charge transfers or charge adsorption on the surface. By application of an external bias, the NW electrodes can be utilized as either anode or cathode, allowing the detection of reduction (U_C) or of oxidation processes (U_A) as in that case the type of the transferred charge can be selected. A schematic presentation of these two sensing mechanisms is shown in figure 3.5.

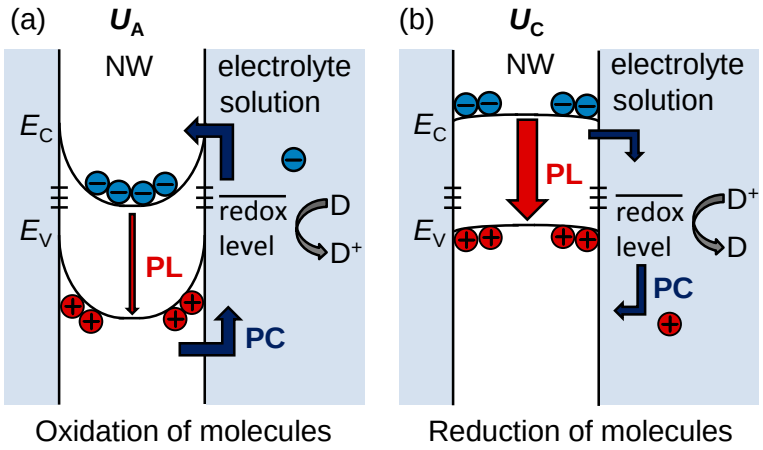

Figure 3.5: Schematic presentation of anodic and cathodic bias voltage application to the WE demonstrating the possibilities of using either (a) oxidation or (b) reduction reactions as detection mechanism. "D/D^+" denotes a molecule in the neutral or in the oxidized form that can either act as a donor or acceptor.

The application of an anodic bias voltage U_A increases the upward SBB in the semiconductor NW. As a consequence, an anodic current can be used for the oxidation of molecules that are present in the electrolyte solution ($D + h^+ \rightarrow D^+$), as holes are transferred from the valence band edge E_V to the redox level of the electrolyte solution or to the redox level of molecules in the electrolyte solution. The photo-excited electrons are transported by the back side contact into the current circuit ($NW - h^+ \rightarrow NW^-$). In contrast, the application of a cathodic bias voltage U_C reduces the upward SBB. In the case of the cathodic current, electrons from the conduction band edge of the WE can be transferred into the redox level of the electrolyte solution/molecule ($D^+ + e^- \rightarrow D$). Concurrently, photo-excited holes are transported by the back side contact into the current circuit ($NW - e^- \rightarrow NW^+$). The respective reactions at the photo-anode (WE) and the cathode (CE) in an aqueous electrolyte solution can be described by

anodic reaction: $2 \cdot h^+ + H_2O \rightarrow \frac{1}{2} \cdot O_2 + 2 \cdot H^+$
cathodic reaction: $2 \cdot e^- + 2 \cdot H^+ \rightarrow H_2$

$H_2O \rightarrow \frac{1}{2} \cdot O_2 + H_2$.

Charge transfer processes such as redox reactions require an appropriate band alignment of the valence and conduction band of the semiconductor and the redox levels of the molecules. The band edge potentials of the valence and conduction band edges of GaN, InGaN and InN and the redox levels of aqueous solutions are shown in figure 3.6.

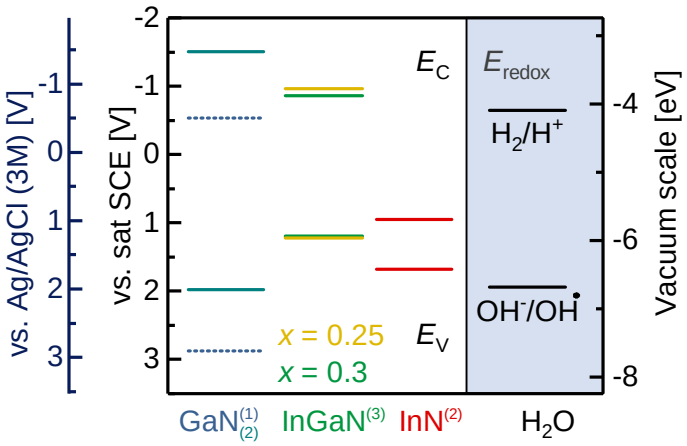

Figure 3.6: Band edge potentials of the valence and conduction band edges of GaN, InGaN and InN and the redox levels for aqueous solutions in units of the electrochemical [V] and vacuum scale [eV]. The values of the semiconductor band edge potentials are extracted or calculated according to refs. (1) [49], (2) [50], (3) [51] and (4) [52]. The redox levels for aqueous solutions are according to ref. [53].

GaN band edges values (1) are calculated according to the results for n-GaN band edge potentials from photocurrent measurements in ref. [49]: $V_C = (-0.538 - 0.046 \cdot \mathrm{pH})\,\mathrm{V}$ vs. SCE for the conduction band edge potential and $V_V = (2.872 - 0.046 \cdot \mathrm{pH})\,\mathrm{V}$ vs. SCE for the valence band edge potential. The GaN and InN band edge values (2) are adopted from ref. [50]. Since the In distribution in the nanowires is inhomogeneous, the InGaN band edges cannot be precisely determined.

The band gap of a binary alloys can be described by a linear relationship of the band gap of each material and the composition. Deviations from the linear interpolation are described by the bowing parameter b. The bowing parameter InGaN alloys is dependent on the In concentration (cf. refs. [34, 54]). In the present case, the In concentration was $[\mathrm{In}] = 20 - 30\,\%$. Thus, a bowing parameter of $b = 1.4\,\mathrm{eV}$ is used for the calculations.

The band gap energies for $\mathrm{In}_x\mathrm{Ga}_{1-x}\mathrm{N}$ alloys can be calculated according to ref. [51] as follows:

$$E_{\mathrm{gap}}(\mathrm{In}_x\mathrm{Ga}_{1-x}\mathrm{N}) = (1 - x) \cdot E_{\mathrm{gap}}(\mathrm{GaN}) + x \cdot E_{\mathrm{gap}}(\mathrm{InN}) - b \cdot x \cdot (1 - x) \qquad (3.6)$$

with b being the bowing parameter ($b = 1.4\,\mathrm{eV}$), $E_{\mathrm{gap}}(\mathrm{GaN})$ is the band gap energy of GaN with $E_{\mathrm{gap}}(\mathrm{GaN}) = 3.44\,\mathrm{eV}$ [54] and $E_{\mathrm{gap}}(\mathrm{InN})$ is the band gap energy of InN with $E_{\mathrm{gap}}(\mathrm{InN}) = 0.76\,\mathrm{eV}$ [54].

3.2 Detection of Ascorbic and Uric Acid and H_2O_2 by Simultaneous Photocurrent and Photoluminescence Measurements using InGaN/GaN NWH Electrodes

Hydrogen peroxide (H_2O_2) is generated as by-product in many biological oxidative processes such as the reduction by glucose oxidase [55, 56]. The fast and accurate determination of H_2O_2 is essential in the fields of food [57, 58], chemical and pharmaceutical industries [59, 60] as well as in the biomedicine and the clinical control [61–63]. Nevertheless, the presence of H_2O_2 gives rise to the inaccurate results of oxidase quantification. Besides, it has been reported that the excess of H_2O_2 damages biological tissues leading to aging [64,65]. It has also been related to some diseases like Parkinson´s disease [66,67]. Thus, the quantification of H_2O_2 in biological fluids is crucial for the control of biochemical processes.

Ascorbic acid (AA) and uric acid (UA) interfere with H_2O_2 [68] and negatively affect the detection of H_2O_2. AA and UA are low-mass antioxidants. They serve as free radical scavengers by donating electrons. The simultaneous detection of these two antioxidants is of great interest due to their presence in biological relevant fluids [69, 70].

Ascorbic acid, known as "vitamin C", is part of frequently used multivitamin preparations. Uric acid is the final product of the purine metabolism. The excess of UA is an indicator for diseases like gout [71, 72]. The differentiation between AA and UA is challenging due to the similar masses and close electrochemical potentials. A current method for UA detection is the use of colorimetric assays which, nevertheless, suffer from an inaccuracy in the quantification of UA [73]. Among others, the presence of AA inhibits the precise quantification of UA [74]. Also in this case, high performance liquid chromatography (HPLC) is used to simultaneously detect AA and UA in samples. However, potential problems are the reproducibility and the durability in acidic conditions [75]. The more advanced HPLC method is based on the coupling of HPLC with electrochemical detection (ECD). HPLC-ECD is the most selective and sensitive technique for vitamin C detection in plasma samples [76]. However, the equipment is cost-intensive and requires elaborate handling [76]. Electrochemical methods such as the differential pulse voltammetry are favored for the selective detection of AA and UA [77–79] since all three coexisting molecules AA, UA and H_2O_2 are electroactive. Nevertheless, the detection and determination of either ascorbic or uric acid is challenging since electrochemical potentials of AA and UA are close to each other [80].

Electrochemical sensors demonstrated to be an appropriate approach for the detection of ascorbic acid, uric acid and H_2O_2 [69]. They possess low detection limits (1 - 7 μM ascorbic acid [81,82], 1 - 27 nM uric acid [81,83], 0.48 μM H_2O_2 [84]), sufficient selectivity [81,83,85] and short response times (< 2 s for AA [82], 5 s for H_2O_2 [84]) [69]. In some cases, these electrodes are based on the functionalization of the sensor surface with chemical mediators. The functionalization results in a reduction of the overpotential and of the interference with other species [86, 87]. The presence of AA and UA, *inter alia*, interferes with the detection of H_2O_2 at the applied anodic potentials. Hence, the determination of H_2O_2 in

presence of these molecules still is an unsolved issue. One of the few successful reports is based on an electrode modified with a composite film of ZnO nanorods and Ag nanoparticles determining the H_2O_2 reduction current [68]. Nevertheless, that sensor system is based on a functionalization of the surface, requiring additional process steps that lack the simplicity of operation. Usually, one molecule species is detected and the interference of the other species is excluded [68, 79, 88]. Hence, at present, there is no fast and simple method to precisely detect AA, UA and H_2O_2 with the same sensor electrode.

The InGaN/GaN NWH arrays feature an intense room temperature photoluminescence (PL) [33] whose intensity sensitively depends on the lateral band profile (surface band bending, SBB) [12]. When operating the InGaN/GaN NWH arrays as optochemical electrodes, the PL intensity can be modulated by the application of an external bias or by the alteration of the pH of the electrolyte solution [12].

The use of the NWH electrodes in an electrochemical configuration allows simultaneous monitoring of the photocurrent (PC) and the PL intensity. Thus, electrical and optical readout of biochemical processes close to the surface can be realized. As a consequence, the charge transfer mechanisms between the electrode and the electrolyte solution can be studied at the same time. Using InGaN/GaN NWH as optochemical sensor electrodes, both oxidation and reduction processes can be induced and monitored, only requiring the adjustment of the respective electrochemical working point.

InGaN/GaN NWHs as three-dimensional materials possess a high surface-to-volume ratio. Consequently, the surface sensitivity is enhanced in comparison to two-dimensional planar structures. This makes the detection of small concentrations of biomolecules in sample solutions possible. In addition, the incorporation of In allows the use of an excitation wavelength in the visible spectrum. Thus, the detection of biomolecules is enabled since the interference and destruction of the molecules under study can be avoided.

Group-III nitride materials exhibit a high electrochemical stability [13–15]. In addition, AlGaN surfaces reveal non-toxic properties in contact with living cells [15]. This qualifies the electrodes for biological applications and in vivo studies. Other nanomaterials that are commonly used for optical biomolecule detection are nanoparticles (NPs), such as gold NPs or surface modified NPs like surface modified quantum dots (QDs). The detection mechanism here is based on the quenching of the nanoparticles´ PL intensity due to hole transfer from the QDs to the molecules [89]. In contrast to the InGaN/GaN NWH electrodes, the working point of such NPs cannot be defined. Thus, the applicability for the detection of one individual biomolecule is limited. Besides, quantum dots have been reported to possess electrochemical stability only in a small pH range in the neutral range of $6 < \mathrm{pH} < 9$ [90] or $6 < \mathrm{pH} < 8$ [91]. For application in different environments, an irreversible decrease of the photoluminescence intensity was observed.

The successful application of InGaN/GaN NWH and GaN NW optochemical electrodes as biosensors in aqueous solutions has recently been demonstrated [12, 22]. The detection of nicotinamidadenindinukleotid (NADH) using InGaN/GaN NWHs as photoanode was shown [22]. The NWH electrodes demonstrated a high sensitivity of 91 μA/mMcm^2 at low bias voltages of $U = 0\,\mathrm{V}$. Here, the NADH luminescence interfered with the PL intensity

of the NWH electrodes and consequently, only the photocurrent could be investigated as sensing mechanism.
Here, InGaN/GaN NWH electrodes as novel sensor material for the detection of H_2O_2, AA and UA are assessed. The PL intensity and PC as a function of the applied bias and the concentration for all three molecules are studied and their application for a new detection scheme is assessed.
In the following section, the measurement setup and the properties of ascorbic acid, uric acid and H_2O_2 are introduced with respect to the investigated detection mechanism. Subsequently, the experimental results are shown: First of all, the bias and concentration dependences of PC and PL intensity in the presence of the analyte molecules are investigated. Based on these findings, the detection of ascorbic and uric acid and H_2O_2 is demonstrated. Finally, the results for the detection using InGaN/GaN NWHs are summarized.

3.2.1 Photoluminescence and Photocurrent Measurement Setup

For photoelectrochemical analysis of the InGaN/GaN NWHs the measurement cell described in section 2.2.1 was used. The PL intensities of the investigated samples were measured in reflection mode. Only the InGaN part was excited using a laserdiode with $\lambda_{exc} = 405\,nm$. The output power of the laser diode can be varied between $P_{output} = 0$-$100\,mW$. Operating the laser diode with $P_{output} = 100\,mW$, the obtained power for sample excitation was determined to $P_{exc,sample} = 25\,mW$ using a power meter. The PL and PC setup is schematically shown in figure 3.7.

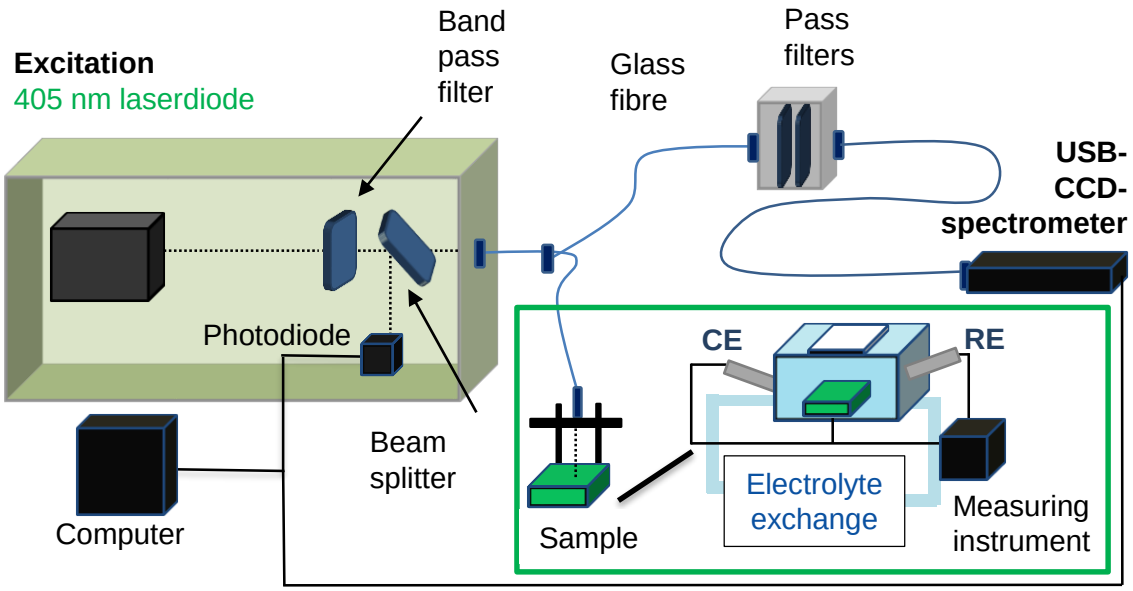

Figure 3.7: Schematic presentation of the PL and PC measurement setup for InGaN/GaN NWHs which can be used for excitation by a laserdiode ($\lambda_{exc} = 405\,nm$).

A band pass filter ($\lambda_{band\ pass} = 405 \pm 5\,nm$) is mounted directly in front of the laserdiode to filter the excitation wavelength. Then, the laser beam is divided by a beam splitter

with a ratio of 19:1. Five percent of the beam are detected by a photodiode to monitor the relative laser power throughout the measurement. The laser beam is coupled into glass fibres ($d_{\text{glass fibre}} = 600\,\mu\text{m}$) for excitation perpendicular to the sample. The PL signal of the sample passes a long pass filter ($\lambda_{\text{long pass}} = 435\,\text{nm}$) and a high precision (hp) long pass filter ($\lambda_{\text{long pass,hp}} = 425\,\text{nm}$) and is detected by a USB-charge-coupled-device(CCD)-spectrometer with a 3648 pixel CCD from $\lambda = 350$ - $880\,\text{nm}$ ("Qwave", RGB Photonics, Kelheim, Germany).
The focused laser spot has a diameter of $d_{\text{laser spot}} \approx 2\,\text{mm}$. Assuming a nanowire density of $180\,\text{NWs}/\mu\text{m}^2$, that equals an excitation of about 10^9 nanowires. The laser power on the sample is $P_{\text{sample}} \approx 25\,\text{mW}$. Hence, the laser excitation power can be calculated to $P_{\text{exc}} \approx 800\,\text{mW}/\text{cm}^2$.
If not stated otherwise, the standard integration time was $t_{\text{int}} = 1\,\text{s}$. For spectral PL measurements three acquisitions and for continuous transient PL measurements one acquisition is used. For transient measurements, the PL spectra were integrated from $\lambda = 400$ - $700\,\text{nm}$. All measurements were performed at room temperature.
The data were evaluated using a Java program written by Pascal Becker, a former member of the working group.
The pH value of the electrolyte solution with and without the investigated molecules as well as the conductivity of the buffer solution ($\sigma \sim 1.4\,\text{mS/cm}$ to $\sigma \sim 1.6\,\text{mS/cm}$) were adjusted before the measurements. The pH and the conductivity values of the reference solution (100 mM HEPES solution pH = 7) with and without $c = 1\,\text{mM}$ of the investigated molecules NADH, ascorbic acid (AA), uric acid (UA) and H_2O_2 are summarized in table 3.1.

Table 3.1: Comparison of pH and conductivity of the reference solution (100 mM HEPES solution pH = 7) with buffer solution with $c = 1\,\text{mM}$ of NADH, ascorbic acid (AA), uric acid(AA) and H_2O_2 each.

Buffer solution	pH	σ [μS/cm]
100 mM HEPES	6.94 ± 0.05	1571 ± 15
100 mM HEPES + 1 mM NADH	7.07 ± 0.05	1650 ± 15
100 mM HEPES + 1 mM AA	6.94 ± 0.05	1477 ± 15
100 mM HEPES + 1 mM UA	6.94 ± 0.05	1478 ± 15
100 mM HEPES + 1 mM H2O2	7.08 ± 0.05	1592 ± 15
100 mM HEPES + 1 mM AA + 1 mM UA	7.01 ± 0.05	1532 ± 15

3.2.2 Properties of Ascorbic Acid, Uric Acid and Hydrogen Peroxide

In the following section, the (electro-)chemical and optical properties of ascorbic acid, uric acid and hydrogen peroxide are presented. Mainly, the photoelectrochemical properties regarding the detection by simultaneous photoluminescence intensity and photocurrent measurements are discussed.

Ascorbic Acid (AA)

Ascorbic acid is a small molecule which is involved in many relevant biosyntheses such as the synthesis of collagen [92] or neurotransmitters [93]. AA is a water-soluble antioxidant. Thus, this acid reacts as scavenger in radical chain reactions [92,94] as for instance the lipid peroxidation [95]. AA is an efficient antioxidant since it is present at high concentrations in many compartments of the body such as the leukocytes and the eye [95]. AA possesses a low reduction potential which allows the reaction in numerous biological systems and it also acts as antioxidant for superoxide [95].
AA has a molecular weight of $M_{\mathrm{AA}} = 176.124\,\mathrm{g/mol}$ [96] which inhibits the diffusion through aqueous membrane pores [95]. The transcellular transport of ascorbate is mainly a sodium-dependent mechanism [97,98] with a Na^+-stoichiometry of 1:1 [99] to 1:2 [100] and requires metabolic energy [101]. With $\mathrm{p}K_{\mathrm{a}} = 4$ [102], it exists as ascorbate-anion AA^- in solutions with physiological conditions [95, 103]. The dissociation hydrolysis occurs either at the hydroxyl positions C2 or C3 with $\mathrm{p}K_{\mathrm{a}} = 4.17$ and $\mathrm{p}K_{\mathrm{a}} = 11.57$, respectively [95]. As antioxidant, AA serves as an electron donor. In these redox reactions, AA itself is reversibly oxidized in a two-electron process [104]. In figure 3.8, the dissociation and the oxidation reaction steps with the intermediate products are presented.

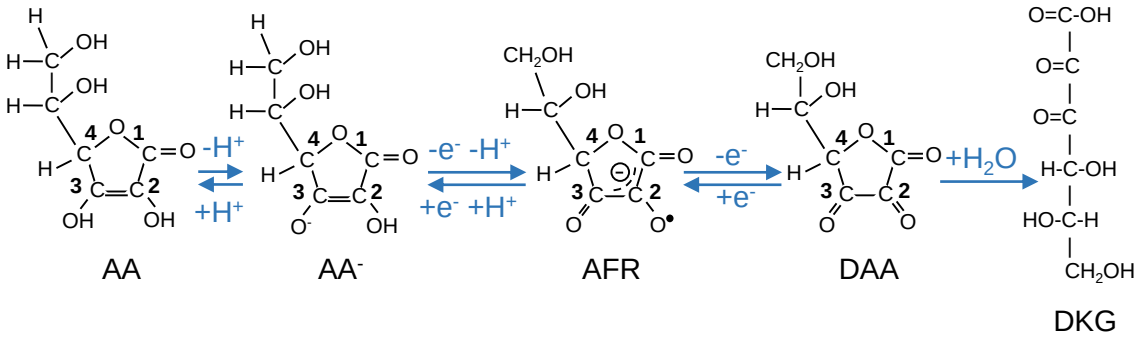

Figure 3.8: Schematic presentation of oxidation of ascorbic acid. The reversible oxidation of ascorbic acid (AA) to dehydro-L-ascorbic acid (DAA) is accompanied by two electron and two proton releases.

First, the oxidation involves the loss of one electron and one proton forming a radical cation (monode-hydro-L-ascorbic acid, AFR). This radical is not reactive and exhibits a high stability over a long time [104]. The long lifetime allows the detection by ESR for example [104]. Subsequently, AFR releases a second electron to form dehydro-L-ascorbic acid (DAA) via disproportionation [104]. DAA exhibits a half-life time of $t_{1/2} = 6$ - $20\,\mathrm{min}$ ($\mathrm{pH} = 7$, $\vartheta = 37\,^{\circ}\mathrm{C}$) [95, 105]. The instability is promoted in alkaline solutions and increases with increasing temperature [106]. The reconversion of DAA to ascorbic acid then proceeds in the acid-glutathione cycle [107]. At high concentrations ($c_{\mathrm{DAA}} = 100$ mM) a $\mathrm{pH} = 3$ could be measured [104]. Under neutral conditions (neutral pH, room temperature), DAA is unstable and hydrolyzes to 2,3-diketo-L-gulonic acid (DKG) [105, 107]. In this process, the ring structure is opened and the properties of "vitamin C" are no longer maintained. DKG is a reaction product of AA and is further reduced into various products. This process is pH- and temperature-dependent and can be affected by an alteration

of any of these two parameters [104].
The respective photo-induced reactions at the anode (WE) and the cathode (CE) can be described by

anodic reaction: $2\,h^+ + AA^- \rightarrow DAA + H^+$
cathodic reaction: $e^- + H^+ \rightarrow 1/2 \cdot H_2$.

The generated protons diffuse through the electrolyte solution to the anode and concurrently, the photo-excited electrons are transported by the back side contact into the current circuit.
However, DAA and AA exhibit similar biological functions [108], but the biological activity of DAA and AA in aqueous solutions differ. For example, the chemical characteristics of dehydro-l-ascorbic acid such as the transport mechanism are different [105, 109]. In contrast to the transport of AA, the transport of DAA does not require metabolic energy [105] and has been demonstrated to be a sodium-independent mechanism [98]. Instead, the transport of DAA proceeds by cellular trapping [105].
In physiological conditions (pH = 7.4), the concentration of AA is $c_{AA,physiol} = 0.03$ - 0.05 mM ($\hat{=} 0.5$ - 0.9 mg/100 ml) in blood [110].
Ascorbic acid shows an absorption band that ranges from approximately $\lambda_{abs} = 200$ - 400 nm [111, 112]. The absorption maximum is at $\lambda_{abs,max} \approx 300$ nm [111, 112]. A detailed investigation of the absorption properties of AA is reported in ref. [113]. In that reference, the absorption spectrum of AA in triply distilled water shows a blue-shift of the absorption peak from approximately $\lambda_{abs} = 265$ - 253 nm with increasing AA concentration [113]. The absorption peak is also shifted to smaller wavelengths with a decrease of the solution pH [113]. In alkaline media the absorption peak maximum position does not shift, but the absorbance is altered due to the formation of DAA [113]. The absorption spectrum of the ascorbate radical is shown in ref. [114]. It is relatively broad ranging from $\lambda_{abs} = 320$ - 420 nm with a maximum at $\lambda_{abs,max} = 360$ nm [114]. The absorption of ascorbate in aqueous solution shows that with the excitation by a laser diode with a wavelength of $\lambda_{exc} = 405$ nm, absorption of the excitation light can be avoided.
The fluorescence spectra reveal that AA fluoresces only very little with a “shoulder” at about $\lambda_{em} \approx 470$ nm for a concentration of $c_{AA} = 24$ mM and at $\lambda_{em} = 345$ nm for a concentration of $c_{AA} = 41.5\,\mu$M [113]. Fluorescence of ascorbic acid is not in the investigated wavelength range of $\lambda = 400$ - 700 nm. Thus, the influence of the AA molecule itself on the PL spectra of InGaN/GaN NWHs is insignificant.

Uric Acid (UA)

Uric acid ($M_{UA} = 168.112$ g/mol [1]) is formed as the end product in the purine catabolism in the human organisms [115]. The largest UA excretion, with about two third, is localized in the kidneys [116]. The last third of UA load is eliminated in the gastrointestinal tract [117]. Just as ascorbic acid, UA naturally exists as antioxidant. It works as free rad-

[1] https://pubchem.ncbi.nlm.nih.gov/compound/uric_acid, 06.07.2018

ical and singlet-oxygen scavenger [118]. The free radical scavenging properties of uric acid offers protection of the DNA from singlet oxygens or OH radicals [118]. In addition, the complex formation of UA with iron or copper prevents ascorbic acid from metal catalyzed oxidation processes. In contrast to AA, UA is not able to scavenge superoxide. Furthermore, the lipid peroxidation in the plasma can only be stopped by UA in the concurrent presence of AA [119].
In contrast to AA, the water solubility of UA is low. For instance, with $c_{\mathrm{UA,blood}} = 68\,\mathrm{mg/L}$, the mean concentration of uric acid in human blood is almost equal to the solubility limit [117]. Above this value, monosodium urate is formed. Typically, the concentration of uric acid in the human plasma is $c_{\mathrm{UA,blood}} = 300\text{ - }500\,\mu\mathrm{M}$ [120]. The excessive presence of UA in blood is called hyperuricemia. Hyperuricemia can cause the development of gout [121]. In solutions of neutral pH (pH = 7.4), UA exist as the monoanion UA^- with $\mathrm{p}K_\mathrm{a} = 5.4$ and $\mathrm{p}K_\mathrm{a} = 10.6$ [122]. In contrast to UA, the oxidized form of UA, allantoin, is more soluble in water [117]. The oxidation reaction of UA is shown in figure 3.9.

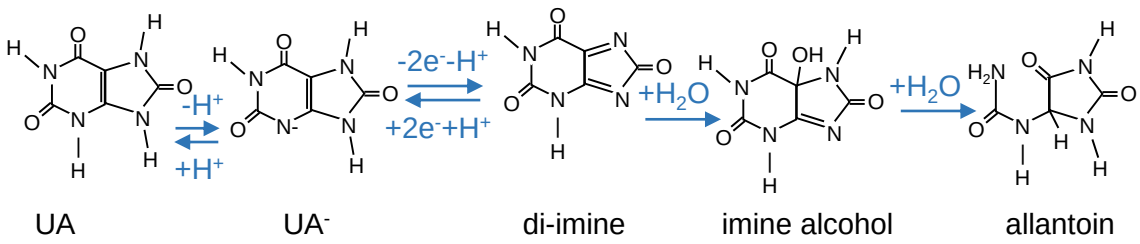

Figure 3.9: Schematic presentation of oxidation reaction of uric acid to allantoin.

The oxidation of uric acid to a di-imine species is accompanied by a two proton and a two electron release [120]. The di-amine species are chemically reactive. Thus, a nucleophilic attack from water results in the formation of imine alcohol [120]. After the addition of another water molecule, the imine alcohol degrades to allantoin [120].
The respective photo-induced reactions at the anode (WE) and the cathode (CE) can be described by

anodic reaction: $2\,\mathrm{h}^+ + \mathrm{UA}^- \rightarrow \text{di-imine} + 2\,\mathrm{H}^+$
cathodic reaction: $\mathrm{e}^- + \mathrm{H}^+ \rightarrow 1/2 \cdot \mathrm{H}_2$.

The generated protons diffuse through the electrolyte solution to the anode and concurrently, the photo-excited electrons are transported by the back side contact into the current circuit.
The absorption spectrum of UA in triply distilled water shows absorption ranging from approximately 210 nm to 320 nm with absorption maxima at $\lambda_{\mathrm{abs,max}} = 233\,\mathrm{nm}$ and $\lambda_{\mathrm{abs,max}} = 290\,\mathrm{nm}$. The absorption peaks show a blue-shift (red-shift) with decreasing (increasing) pH [113]. Also in this case, the excitation with a laser diode with a wavelength of $\lambda_{\mathrm{exc}} = 405\,\mathrm{nm}$ avoids absorption by the molecule.
The fluorescence spectrum or UA is pH-independent with an emmision maximum of $\lambda_{\mathrm{em,max}} \approx 355\,\mathrm{nm}$. The fluorescence intensity decreases with increasing pH [113]. These

spectra demonstrate a negligible fluorescence intensity at wavelengths above $\lambda_{em} > 470\,nm$ [113]. The fluorescence intensity of uric acid in the investigated wavelength range ($\lambda_{exc} = 400$ - 700 nm) is very low. Thus, the influence of UA on the PL spectra of InGaN/GaN NWHs is insignificant.

Hydrogen Peroxide (H_2O_2)

Hydrogen peroxide is a reactive oxygen species (ROS) just like the superoxide anion and the hydroxyl radical. H_2O_2 is the most stable among these three ROS [67]. Hydrogen peroxide is formed as side product of many oxidative decomposition reactions in cells. Thus, the precise detection of H_2O_2 is relevant in the biological field. Oxidase-sensor strategies rely on the detection of H_2O_2. Oxidases are part of most of the existent enzyme-based sensors and screening kits ($> 90\,\%$) [123]. In addition, H_2O_2 is used for disinfection of water [124] and for the disinfection in the food industry [62, 125].
Hydrogen peroxide is formed by the spontaneous and catalytic cleavage of superoxide anions [126]. It has a molecular weight of $M(H_2O_2) = 34.0147\,g/mol$ [96] and is significantly smaller than AA and UA. Based on the small size, the selective detection of H_2O_2 in a solution with AA was demonstrated [85]. In addition, due to the small size, H_2O_2 can diffuse transcellular through water channels where it causes protein oxidation [67]. This is why H_2O_2 is associated with cell damage and diseases [63].
Hydrogen peroxide features a special electro-catalytic activity and can both be oxidized and reduced. The chemical oxidation (reduction) reaction of hydrogen peroxide can be described according to

$$H_2O_2 + 2 \cdot h^+ \rightarrow 2 \cdot H^+ + O_2(g) \quad \text{(oxidation, alkaline solutions)} \tag{3.7}$$

and

$$H_2O_2 + 2 \cdot H^+ + 2 \cdot e^- \rightarrow 2 \cdot H_2O \quad \text{(reduction, acidic solutions)} \tag{3.8}$$

with a standard potential of $E_0 = 1.776\,V$ [96] for acidic solutions and $E_0 = 0.88\,V$ for molar alkaline solutions [127]. The oxidation and reduction of H_2O_2 is pH-dependent. For alkaline pH, H_2O_2 acts as reducing agent and H_2O_2 is oxidized. On the contrary, for solutions with acidic pH, H_2O_2 acts as oxidizing reagent and is reduced itself.
Hydrogen peroxide has a pK_a value of 11.62 [96], *id est*, almost 100 % of H_2O_2 is protonated in neutral solutions such as the cytosol [128].
H_2O_2 is known for its thermodynamic instability. The calculation of the Gibbs free energy ΔG with the enthalpies $H_{f,H_2O_2} = -187\,kJ/mol$ and $H_{f,H_2O} = -285.8\,kJ/mol$ and the entropies $S^\circ_{H_2O_2} = 109.6\,kJ/mol$, $S^\circ_{H_2O} = 70\,kJ/mol$ and $S^\circ_{O_2} = 161.1\,kJ/mol$ (all values are extracted from ref. [96]) yields $\Delta G < 0$ for standard conditions as well as for high and low temperatures. The molecule decomposes into water and oxygen. In addition, the H_2O_2 molecule is not stable when irridated with ultraviolet light ($\lambda_{exc} = 205$ - 280 nm) [129]. In

this course, highly reactive hydroxyl radicals are formed which interfere with the H_2O_2 molecule, leading to a disruption of the sensing signal. The reaction is according to

$$H_2O_2 + h\nu \rightarrow 2 \cdot OH^{\bullet}. \tag{3.9}$$

The InGaN NWHs allow for the excitation with light of a wavelength in the visible range. Thus, the disturbance and falsification of detection signals are avoided.
The absorption of H_2O_2 in the liquid and in the vapor phase coincide [2]. H_2O_2 absorbs in the ultraviolet region [130]. The transmission spectrum of 1 mM H_2O_2 in 100 mM HEPES solution at pH = 7 was measured and did not show absorption in the relevant wavelength range.
The fluorescence intensity of 1 mM H_2O_2 in 100 mM HEPES solution at pH = 7 for excitation with $\lambda_{exc} = 405$ nm is shown in figure 3.10.

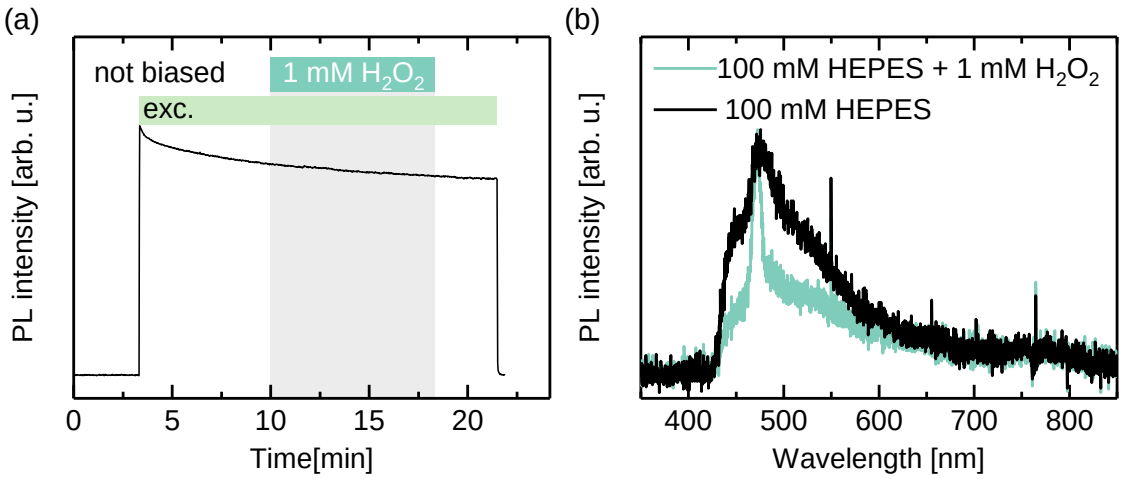

Figure 3.10: (a) PL intensity measurement with nitridated silicon as WE (not biased) using 100 mM HEPES solution pH = 7 without and with 1 mM H_2O_2 for excitation with $\lambda_{exc} = 405$ nm. The PL intensity decreases due to a degradation of the electrode. The presence of 1 mM H_2O_2 does not alter the PL intensity. (b) Fluorescence spectra of 100 mM HEPES solution pH = 7 with and without 1 mM H_2O_2 for excitation with $\lambda_{exc} = 405$ nm. The PL maximum does not shift in energy.

The investigations of the fluorescence intensity does not show a difference between the buffer solution with and without 1 mM H_2O_2. The PL intensity decreases due to degradation of the NW electrode.

[2] http://www.dtic.mil/dtic/tr/fulltext/u2/022243.pdf, 06.07.2018

3.2.3 Results and Discussion

Bias- and pH-dependent Photocurrent and Photoluminescence Measurements with InGaN/GaN NWH Electrodes in Presence of AA, UA and H_2O_2

The photoelectrochemical detection of NADH with InGaN/GaN NWHs due to the hole transfer from the InGaN part to the NADH molecule was investigated. The results are shown in figure 3.11.

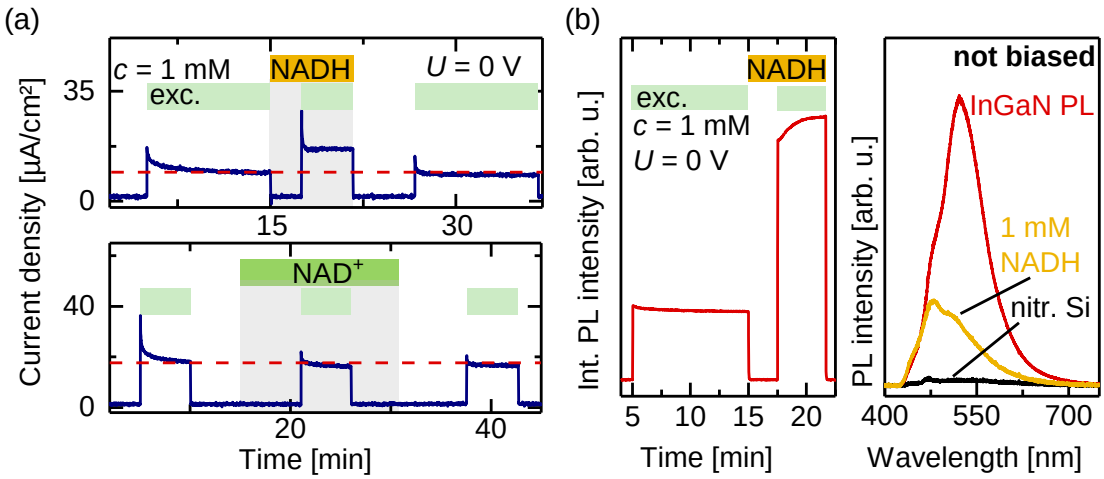

Figure 3.11: (a) Photoelectrochemical detection of 1 mM NADH in the buffer solution at $U = 0\,\mathrm{V}$. The PC increases in the presence of reduced NADH molecules due to the oxidative conversion by hole transfer, but not in the presence of the oxidized form NAD^+. (b) Integrated PL intensity in dependence of the NADH presence at $U = 0\,\mathrm{V}$. The PL intensity increases when NADH is present (left). On the right: Comparison of intrinsic luminescence of NADH with PL intensity of InGaN/GaN NWH electrodes (not biased) and the silicon substrate. The fluorescence of NADH interferes with the PL intensity of the InGaN/GaN NWH electrodes.

In figure 3.11(a) the evolution of current density in the presence of 1 mM NADH and 1 mM NAD^+ with and without photoexcitation is shown. The anodic PC increases in presence of 1 mM NADH. The PC in presence of 1 mM NAD^+ does not change. Since the anodic PC depends on the applied bias voltage and the concentration (cf. ref. [22]), the signal changes can be ascribed to the oxidation of the reduced NADH to NAD^+ according to

$$\mathrm{NADH} \rightarrow \mathrm{NAD^+} + \mathrm{H^+} + 2 \cdot \mathrm{e^-}. \tag{3.10}$$

Nevertheless, the drawback of the detection mechanism of this coenzyme is that the intrinsic fluorescence intensity of NADH overlaps the InGaN photoluminescence in the respective wavelength range (cf. figure 3.11(b)). The PL intensity increase in presence of NADH is mainly due to the NADH fluorescence. The changes of the InGaN PL intensity cannot be detected and only the detection of the photocurrent is possible.

In this section, the charge transfer processes across the InGaN/GaN NWH photoelectrode

and with ascorbic acid, uric acid and hydrogen peroxide being present in the electrolyte solution are studied by PL and PC measurements. In the course of these experiments, the dependence on bias, pH and concentration is investigated. The results of the charge transfer mechanisms between the NW electrodes and the molecules in the solution are discussed. Finally, the detection of AA with UA and H_2O_2 as background signals and the detection of H_2O_2 with AA and UA as background signals are presented.

The detection mechanism of AA, UA and H_2O_2 by simultaneous PC and PL measurements was investigated. With the pK_a values from section 3.2.2 the degree of dissociation of UA at pH = 7 is $\alpha_{UA} \approx 97.55\,\%$. Ascorbic acid, as a medium strength acid, is almost entirely dissociated under these conditions with $\alpha_{AA} \approx 99.90\,\%$ (pH = 7). As a result, AA exists as negatively charged molecule in the reduced form AA^- [104, 131]. H_2O_2 is a weak acid with a $pK_a = 11.62$ (cf. section 3.2.2). In water, a pH-dependent equilibrium of H_3O^+- and HO_2^--ions is present.

The molecules under study do all meet the specified requirements for photo-induced oxidation. The redox potentials and the conduction and valence band edges of InGaN are depicted in figure 3.12.

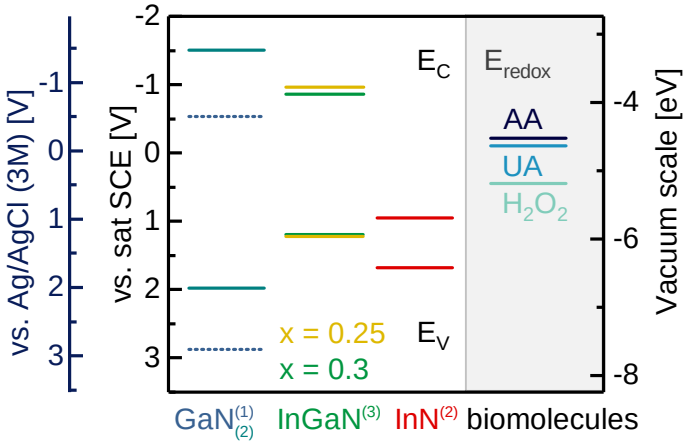

Figure 3.12: Band alignment of the valence and conduction band edges of GaN, InGaN and InN and the redox potentials of ascorbic acid, uric acid and H_2O_2 in units of the electrochemical [V] and vacuum scale [eV]. The values of the semiconductor band edge potentials are extracted or calculated according to refs. (1) [49], (2) [50] and (3) [51]. The redox potentials of ascorbic and uric acid are extracted from ref. [80] and the redox potential of hydrogen peroxide is extracted from ref. [96] with $E_0 = 1.776$ V.

First, the relative changes of the dark current in presence of AA, UA and H_2O_2 were analyzed in reference to the respective electrolyte solution without the molecules according to

$$\Delta I_{\mathrm{dark}} = [I_{\mathrm{dark}}(c = 1\,\mathrm{mM})/I_{\mathrm{dark}}(c = 0\,\mathrm{mM})] - 1.$$

The results are shown in figure 3.13.

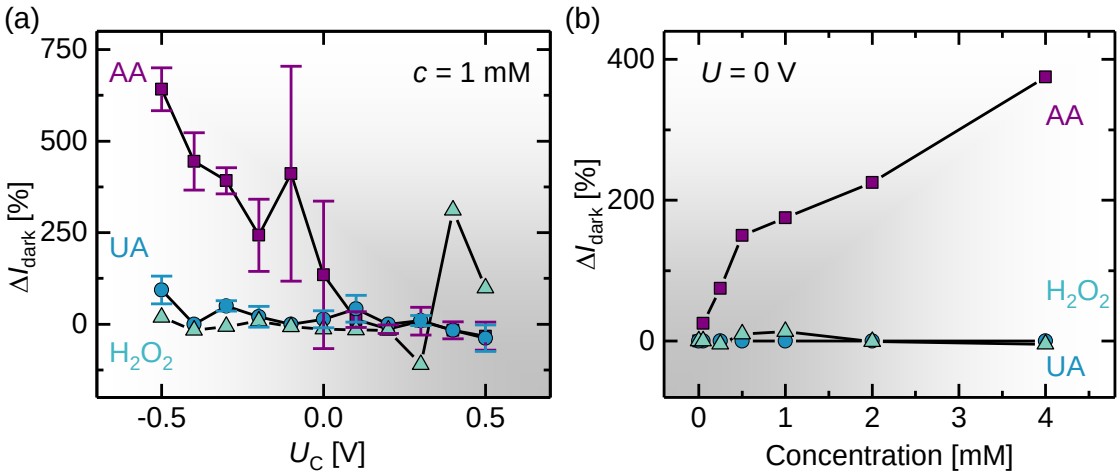

Figure 3.13: Changes of the dark currents in presence of the different molecules AA, UA and H_2O_2 normalized to the dark current for the solutions without molecules in dependence of (a) U_C for $c = 1\,\mathrm{mM}$ and $\mathrm{pH} = 7$ and (b) the respective concentration of the molecule at $U = 0\,\mathrm{V}$ and $\mathrm{pH} = 7$. The presence of AA and UA results in an increase of the anodic dark current which increases with U_A (and increasing AA concentration).

The presence of AA and UA results in an increase of the anodic dark current. The increase in presence of AA is enhanced for U_A and higher AA concentrations. The increase of the dark current in presence of UA is dependent on U_A, but it does not vary with c_{UA}. The maximal change of the dark current is $\Delta I_{dark,max} \approx 640\,\%$ for 1 mM AA and $\Delta I_{dark,max} \approx 100\,\%$ for 1 mM UA. The findings are in contrast to the results of hydrogen peroxide. H_2O_2 features a constant dark current independent of the investigated bias potentials and concentrations. Thus, the charge transfer processes to AA and UA are different from that to H_2O_2.

The dark current characteristics for a semiconductor electrode in contact with an electrolyte can be described analogous to the I/V characteristic of a Schottky diode (cf. section 3.1). The observed increase of the anodic current in presence of the molecules can be explained by a reduction of the barrier height since the barrier height is the parameter determining the electron charge transfer. This reduction can be caused by the adsorption of positive charges/dipoles such as protons or by the passivation of surface states which both reduce the present negative surface charge. Since the current density depends exponentially on the barrier height, a small reduction of φ_B results in a pronounced shift of the I/V curve towards higher current densities. Thus, the increase of the dark current with increasing anodic bias in presence of AA and UA can be explained with a reduction of the negative surface charge and hence, decreasing the barrier height. The bias- and concentration-dependent increase of the dark current can be associated with the dissociation constants of the investigated molecules. These constants show that the dissociation of AA and UA preferentially proceeds in aqueous solutions in comparison to hydrogen peroxide. Ascorbic acid is the strongest acid among these three. This tendency is in agreement with the findings. Thus, the dissociation of the acids results in an evolution of protons that act as positive surface charge at the interface decrease the barrier height.

To study the charge transfer mechanism between AA, UA and H_2O_2 and the InGaN/GaN

NWH electrode in more detail, the I/V characteristics before and after photoexcitation were analyzed. For this purpose, the PC and the PL intensity were transiently recorded when the electrolyte solution was exchanged. The electrolyte solutions contained the three biomolecules with $c = 1\,\mathrm{mM}$ each. To enable the simultaneous measurement of PC and PL, a bias voltage of $U = 0\,\mathrm{V}$ was applied. According to figure 2.6, this potential allows for the measurement of a sufficient PC and the detection of PL intensity changes. The working point was chosen to be in the sensitive bias range (cf. figure 2.7(b)). The results for the different molecules are shown in figure 3.14. Here, for better comparison, the normalized PC and PL intensity changes are displayed.

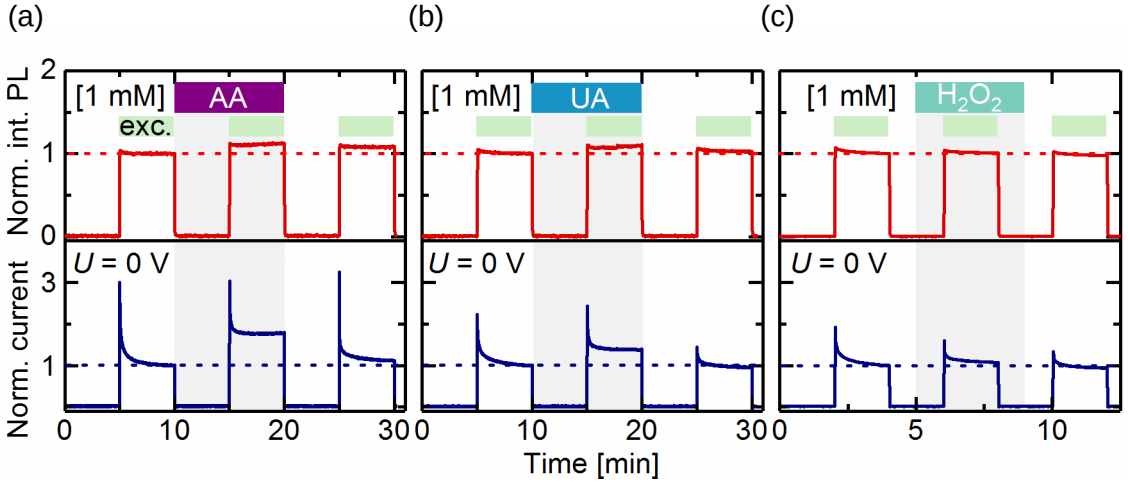

Figure 3.14: Transient PL and PC measurement in presence of 1 mM of (a) AA, (b) UA and (c) H_2O_2 at $U = 0\,\mathrm{V}$ and $\mathrm{pH} = 7$. Both PL and PC are normalized to the last value of the first excitation sequence. In presence of AA and UA, the PC and the PL intensity increase. In presence of H_2O_2, the PC slightly increases, but the PL intensity is not strongly altered.

In presence of 1 mM AA and UA, the PL intensity and the PC density increase. The PL intensity increase is about $\Delta\mathrm{PL}/\mathrm{PL}_0 \approx 12\,\%$ for ascorbic acid and $\Delta\mathrm{PL}/\mathrm{PL}_0 \approx 10\,\%$ for uric acid. The PC increase is more pronounced in the presence of AA. Here, the PC increase amounts to $\Delta\mathrm{PC} \approx 78\,\%$ whereas the increase of the PC in the presence of UA is $\Delta\mathrm{PC} \approx 38\,\%$. The PC increase in presence of hydrogen peroxide is $\Delta\mathrm{PC} \approx 7\,\%$. The PL intensity is hardly changing when the electrolyte solution is changed to a buffer solution with 1 mM H_2O_2 ($\Delta\mathrm{PL}/\mathrm{PL}_0 \approx 1\,\%$).

Both the PL intensity and the PC density can be modulated by the decrease or increase of the hole accumulation at the surface. The holes as minority carriers play a crucial role for the PL characteristics of n-type InGaN/GaN NWH electrodes (cf. section 2.2). Further, the increase in the anodic photocurrent indicates that holes are transferred into the electrolyte solution. The molecules in the electrolyte solution are oxidized and the electron transfer into the nanowires is detected. However, next to the increase of the anodic PC, an increase of the PL intensity is found. Thus, the PL increase is not based on the reduction of the accumulation of near-surface holes, but rather on a change of the SBB due to a modulation of the charge at the interface such as an increase of the proton concentration or

the saturation of interface states. As a result, the probability for radiative recombination reactions is raised and the PL intensity increases. AA as strong acid shows the largest PL increase, the PL increase of UA as the weaker acid is smaller and for hydrogen peroxide, which is the weakest acid, the increase is negligible by comparison.

The charge density at the interface can be varied by the change of the photon flux, the molecule concentration in the electrolyte solution and the applied bias resulting in a change of the barrier height and the SBB. Hence, the charge transfer mechanism between AA, UA and H_2O_2 and the InGaN/GaN NWH electrode was investigated by bias-dependent PL and PC measurements. This study enables the comparison of the modulation of the SBB for reverse and forward bias (U_A and U_C) before and after photoexcitation. In addition, the band alignment of the molecules can be correlated with their charge transfer rates of the oxidation reaction. This means - in terms of oxidation reaction - that the chemical conversion of the molecule with its redox potential closer to the conduction band edge of InGaN is energetically favored to transfer holes from the electrode to the molecule.
The measurements were conducted according to the transient measurement sequence shown in figure 3.14. Here, the PL intensity change is the difference between the PL intensity of the last data point in the sequence with 1 mM of the molecules and the PL intensity of the last data point in the first sequence with only 100 mM HEPES solution before the addition of the molecules ("ref."). The changes of the PL intensity are given as

$$\Delta\mathrm{PL}/\mathrm{PL}_0 \;=\; [\mathrm{int.\,PL(solution} + 1\,\mathrm{mM\ molecules})/\mathrm{int.\,PL(ref.\,solution)}]\text{-}1.$$

The changes of the PC densities are determined in an analogous manner, but additionally the PCs were calculated separately for the intervals with and without molecules from the current. The differences of the photocurrents are denoted as

$$\Delta\mathrm{PC} \;=\; \mathrm{PC(solution} + 1\,\mathrm{mM\,molecules}) \;-\; \mathrm{PC(ref.\,solution)}.$$

The resulting bias dependences of $\Delta\mathrm{PL}/\mathrm{PL}_0$ and $\Delta\mathrm{PC}$ for ascorbic acid, uric acid and hydrogen peroxide at $\mathrm{pH} = 7$ are displayed in figure 3.15.

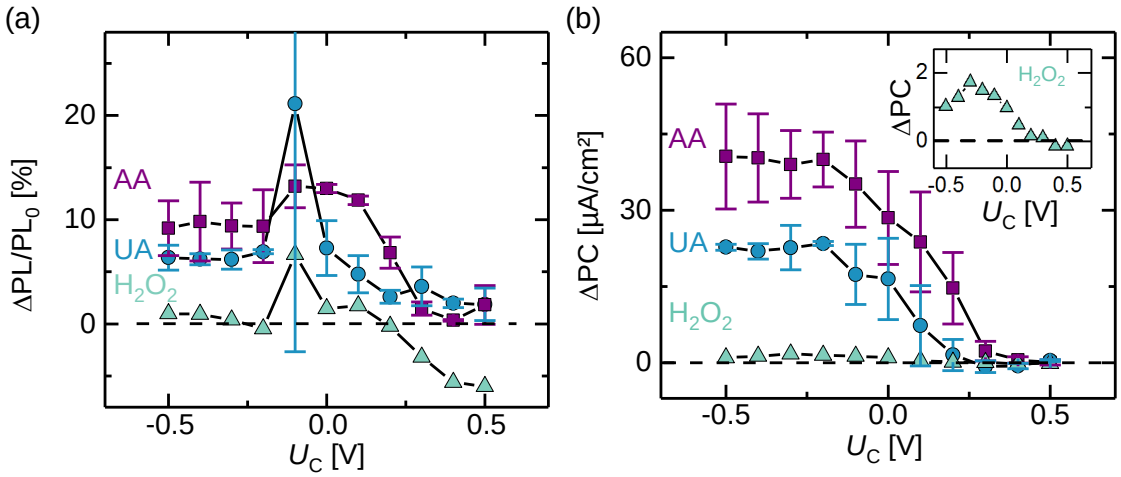

Figure 3.15: (a) Relative change of PL intensity due to the presence of 1 mM AA/UA/H_2O_2 in dependence of U_C at pH = 7. The PL intensity increases for AA and UA. The presence of H_2O_2 results in a PL intensity increase for $U_C < 0.2$ V. For $U_C > 0.2$ V, the PL intensity decreases for H_2O_2. (b) Change of the PC density due to the presence of the different molecules. The anodic PC increases for all molecules for $U_C \leq 0.3$ V. In presence of H_2O_2, the PC decreases for $U_C > 0.3$ V (inset).

For all U_C, the changes of the PL intensity in presence of 1 mM AA and UA are positive. The PL intensity increase for 1 mM AA and UA is found to be more pronounced for anodic bias. The presence of H_2O_2 results in a PL intensity increase for $U_C < 0.2$ V. The increase of the PL intensity in the presence of AA and UA with $\Delta PL/PL_0(AA) \approx 13\,\%$ and $\Delta PL/PL_0(UA) \approx 7\,\%$ is substantially larger than in the presence of H_2O_2 which is $\Delta PL/PL_0(H_2O_2) \approx 2\,\%$. For $U_C > 0.2$ V, the PL intensity decreases linearly for H_2O_2, *id est*, for $U_C = 0.2$ V the PL response for H_2O_2 is suppressed. Coincidentally, the photocurrent change due to 1 mM H_2O_2 (cf. inset in figure 3.15(b)) exhibits a change of the sign for $U_C > 0.3$ V: the PC density decreases in the presence of hydrogen peroxide. For H_2O_2, both oxidation and reduction of the molecule can occur, depending on the applied potential and the pH. In general, an anodic PC indicates an oxidation reaction whereas cathodic currents arise from reduction processes.

The PC increase in presence of AA is found for $U_C \leq 0.4$ V, the PC increase due to UA for $U_C \leq 0.1$ V and the PC increase due to H_2O_2 for $U_C \leq 0.3$ V. The increase of the PCs shows a linear dependence with decreasing U_C until ΔPC reaches a maximum. These are $U_{C,\Delta PC_{max}}(AA) = -0.2$ V, $U_{C,\Delta PC_{max}}(UA) = -0.2$ V and $U_{C,\Delta PC_{max}}(H_2O_2) = -0.3$ V. For $U_C > 0.3$ V, the PC does not change.

The magnitudes of the InGaN PL intensity and the PC of the n-type InGaN/GaN NWHs depend on the hole accumulation at the surface. By modulation of the minority carrier density at the surface, the PL or PC can be enhanced. Since PL and PC increase with increasing the SBB, the hole transfer from the NW electrode into the electrolyte solution as exclusive charge carrier transfer process can be excluded.

The results indicate a current increase due to the simultaneous reduction of the barrier height and the oxidation in presence in presence of AA and UA. Their dissociation and the concomitant generated protons alter the barrier height/SBB since the observed PL

increase is amplified for U_A which corresponds to the presentation in figure 3.2(c) (cf. figure 3.3). The PL increase is not caused by a reduction of the non-radiative transfer of holes from the NW into the electrolyte solution. The saturation of the PL increase can be explained by the statistical incidences of dissociation/proton release and oxidation. Both processes run in parallel and cannot be distinguished in this measurement.
The increase of U_A enhances the density of near-surface holes and non-radiative charge transfer rates, such as the anodic PC, increase. From the PC increase, one can draw the conclusion that with increasing number of photo-generated minority carriers at the surface (U_A), the oxidation of the molecules is promoted. This increase saturates due to an dynamic equilibration between oxidation and dissociation reaction. The PC increase is more distinct for AA than for UA and H_2O_2. This can partially be attributed to the band alignment (cf. figure 3.12) and it follows that the magnitude of the driving force decreases from AA over UA to H_2O_2.
The bias-dependent results show anodic PCs for ascorbic acid, uric acid and hydrogen peroxide. The onset potentials for AA and UA differ by approximately hundred millivolts ($U_{C,PC}(AA) = 0.4 \pm 0.1\,V$, $U_{C,PC}(UA) = 0.3 \pm 0.1\,V$) allowing a differentiation between these two acids by selecting the higher onset potential as working point.

Furthermore, the changes of PC and PL intensity were investigated as a function of the concentration of AA, UA and H_2O_2 at $U_C = 0\,V$ for a buffer solution at pH = 7. The results are shown in figure 3.16.

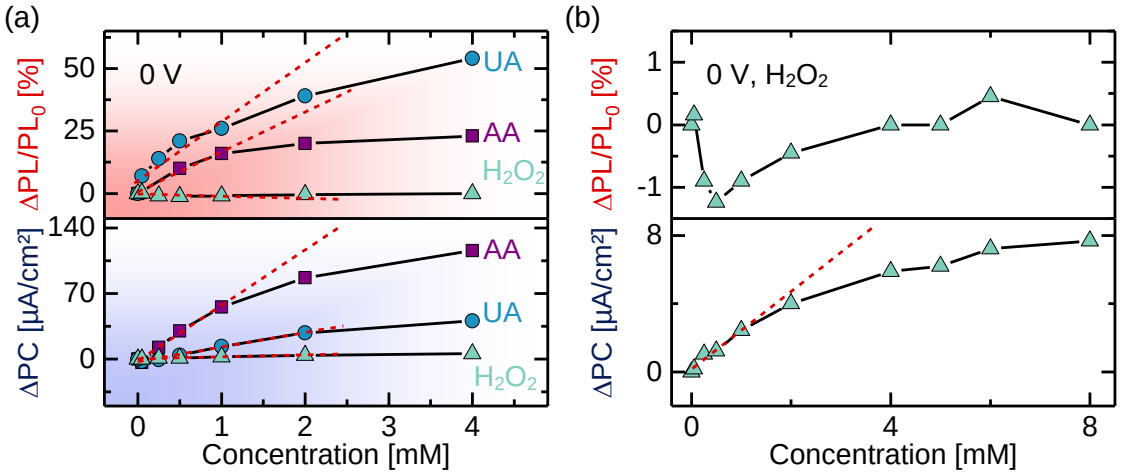

Figure 3.16: (a) Concentration-dependent PC and PL intensity changes due to the presence of AA, UA and H_2O_2 at $U = 0\,V$ and pH = 7. The PC dependence on the bias and the concentration of the molecules indicate the proceeding of photoelectrochemical oxidation. (b) Concentration-dependent PC and PL intensity changes due to the presence of H_2O_2 at $U = 0\,V$ and pH = 7.

The anodic photocurrents increase with increasing concentrations of AA, UA and H_2O_2. These findings indicate that the photoelectrochemical oxidations proceed according to

$$C_6H_8O_6 \rightarrow C_6H_6O_6 + 2 \cdot H^+ + 2 \cdot e^- \text{ for AA}, \tag{3.11}$$

$$C_5H_4N_4O_3 \rightarrow C_5H_2N_4O_3 + 2 \cdot H^+ + 2 \cdot e^- \text{ for UA} \tag{3.12}$$

and

$$H_2O_2 \rightarrow O_2\,(g) + 2 \cdot H^+ + 2 \cdot e^- \text{ for } H_2O_2. \tag{3.13}$$

The photocurrent density increase for ascorbic acid shows the highest sensitivity in the linear range with 59 μA/mMcm^2 compared to a sensitivity of 15 μA/mMcm^2 for uric acid. Both the smallest PC change and the smallest sensitivity are observed for hydrogen peroxide (cf. figure 3.16(b)). The calibration curve of H_2O_2 demonstrates a sensitivity of only 2 μA/mMcm^2 in the linear range ($c_{H_2O_2} < 1$ mM). The PL intensity changes are concentration-dependent and increase with increasing AA, UA and H_2O_2 concentrations. The decrease of the relative PL intensity in presence of H_2O_2 for small $c_{H_2O_2}$ (cf. figure 3.16(b)), first data points) is caused by photoelectrochemical oxidation of the nanowire surface during the transient measurements. As a consequence, the PL intensity response is reduced and conceals the actual small PL intensity increase. Actually, the increase of H_2O_2 concentration at the beginning of the measurement sequence results in an increase of the PL intensity. The increase of the PL is comparable for AA and UA in the range of small concentrations (c < 1 mM, cf. figure 3.16), but for concentrations c > 1 mM the PL change is more distinct for UA.

The quantity of molecules in the electrolyte solution increases as the concentration increases and thus, the concentration-dependent increase of the PC is related to the oxidation-dependent conversion of the molecules.

By contrast, the PL dependence on the molecule concentration cannot be described in detail, yet. The PL intensity increases with increasing concentration featuring the concentration of dissociated molecules and generated protons in the electrolyte solution. The observed reduction of the SBB can be caused by the local acidification of the elecrolyte solution in close proximity to the nanowire surface or by the suppression of non-radiative paths via surface passivation by the molecules or oxidatively converted molecule species in the elecrolyte solution. The details of the processes are not clear, yet. In general, the observed results are small. The PL increase is more distinct for UA than for AA. This cannot be directly correlated to the different acidity. Here, the situation becomes more complex. UA and AA are relatively big molecules which results in a hampering of diffusion so that the situation rapidly changes. Hydrogen peroxide is the smallest molecule of these three which is why this molecule shows the highest concentration until saturation. The emerging state at the interface is complex and the precise determination of the composition is not possible since the measurements allow for the monitoring of a mean dynamic equilibrium between the different reaction processes. However, the simultaneous PL and PC measurement allows the estimation of the change of charge density at the interface and thus, the change of the barrier height.

For hydrogen peroxide, both the oxidation and the reduction of the molecule are reported.

The type of conversion depends on the applied potential and the pH. In figure 3.17 the pH-dependent PC and PL changes are shown.

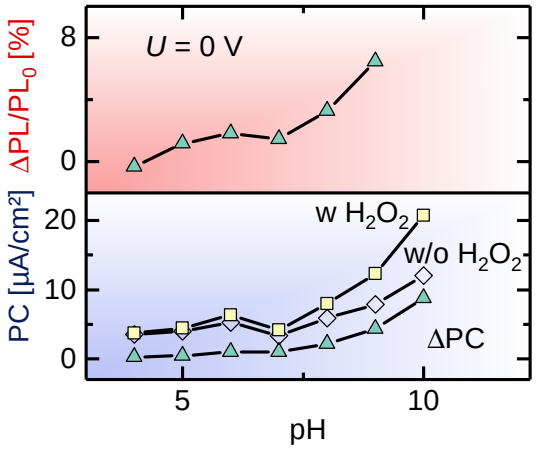

Figure 3.17: Photocurrent and PL intensity changes in dependence on the pH of the electrolyte solution at $U = 0$ V in presence of 1 mM H_2O_2.

The investigation of the pH-dependent PL changes in presence of H_2O_2 demonstrates that the photocurrent response increases with alkaline pH. In acidic solutions, the photocurrent increase is slightly attenuated because of the proton formation in the oxidative process. In contrast, the reduction reaction of hydrogen peroxide is promoted in acidic solution [132]. Here, only the oxidative (anodic) photocurrent was investigated. The current increase in alkaline solutions has already been reported for other sensor materials [133, 134]. The PL intensity response increases with increasing pH. Since in alkaline media and at U_A the oxidative conversion of hydrogen peroxide is promoted, the oxidized species, which reduce the barrier height, are related to the PL change increase. The mechanism is not known in detail.

The barrier height is reduced by the presence of the molecules realized by the dissociation of the molecules into anions and protons or by the modulation of surface states. To investigate the proposed mechanism, the influence of the molecules on the surface band bending was investigated by studying the open circuit potential in dark conditions and during excitation with $\lambda_{exc} = 405$ nm in reference to the RE. The measurement of the OCPs can provide an indication about the surface charge provided that the changes are relatively large. The open circuit potentials were measured time-dependent and the final values after 30 min are extracted. The results are depicted as shifts in reference to 100 mM HEPES solution pH = 7 without molecules in figure 3.18(a). Then, the OPC values were used for a comparison of the open circuit potentials after photoexcitation of 100 mM HEPES solution pH = 7 with 1 mM of AA, UA and H_2O_2. The results are shown in figure 3.18(b).

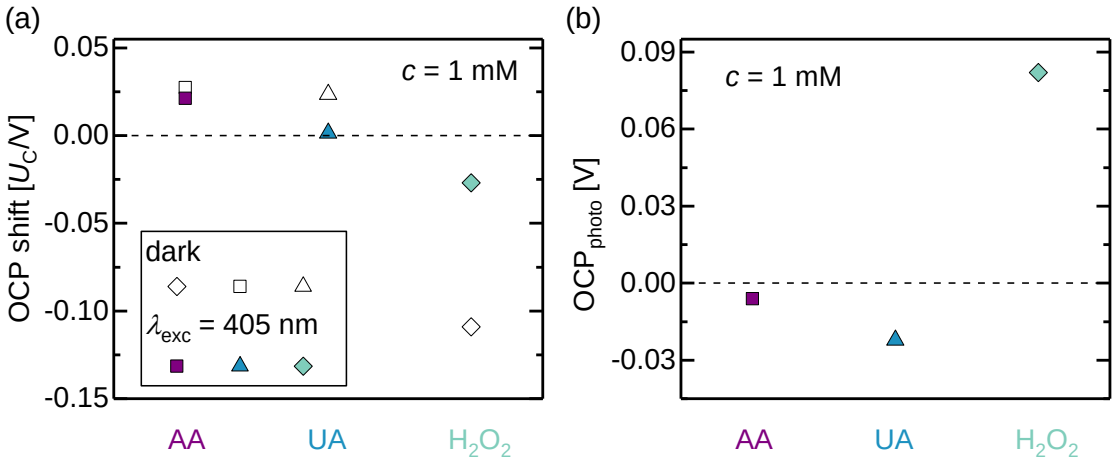

Figure 3.18: (a) Comparison of open circuit potentials in reference to RE in dependence of the presence of 1 mM AA, UA and H_2O_2. The values of the OCPs after 30 minutes of measurement were extracted. The shift of the OCP due to the presence of 1 mM AA or UA in the solution are negligible. The OCPs for dark conditions and $\lambda_{exc} = 405$ nm excitation of H_2O_2 are shifted towards anodic bias potentials. (b) The OCP_{photo} for AA and UA are comparable to the pure solution, but for the presence of H_2O_2, it is increased.

In general, the open circuit potentials show only a small shift. The differences for AA and UA with and without the molecules are negligible. A static change of the SBB cannot be evaluated. Furthermore, the OCP_{photo} of AA and UA are comparable to the solutions without molecules.
The OCPs of H_2O_2 measured in dark and after photoexcitation shifts to U_A indicating a decrease of the PC. Since the OCP_{photo} is increased, the two effects compete and do not allow the identification of a distinct change in photocurrent based on the influence on the surface band bending.

The excitation with an energy smaller than the band gap energy ("sub-band gap excitation") allows to investigate the contribution of the GaN base to the increases of the anodic photocurrents and photoluminescence intensities. The charge transfer between AA, UA and H_2O_2 and GaN NW electrodes were investigated by excitation with $\lambda_{exc} = 405$ nm. The current was measured at $U_C = -0.1$ V. At that bias potential, InGaN/GaN NWH electrodes showed a sufficient photocurrent and a surface sensitive PL intensity. The results are shown in figure 3.19.

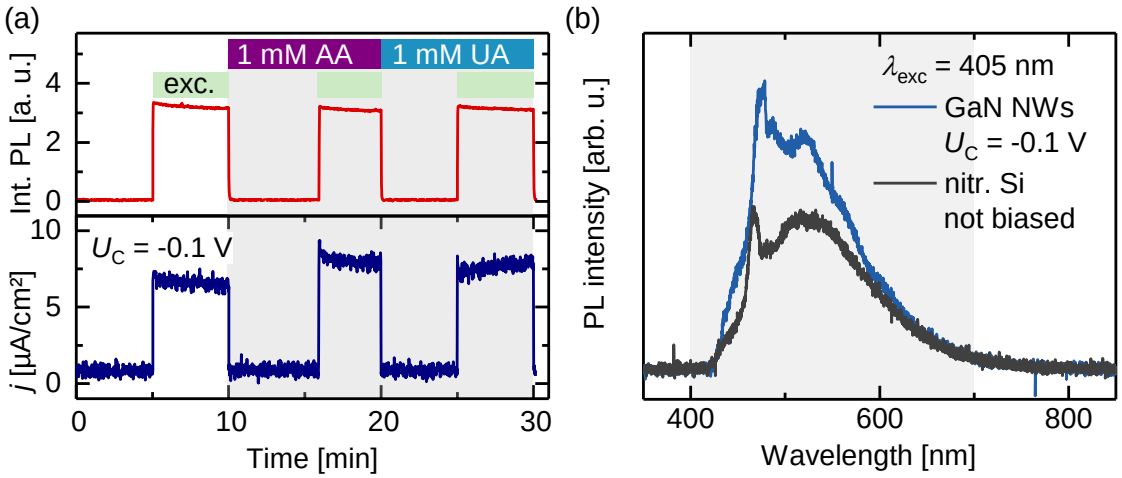

Figure 3.19: (a) Transient PL and PC measurement with a GaN NW working electrode. The samples were excited with a laser diode of $\lambda_{exc} = 405\,nm$ to investigate the origin of the PC and PL changes in the presence of 1 mM AA and UA. The presence of AA and UA results in an increase of the anodic PC. The intensity does not change in the presence of 1 mM AA and UA. The PL was integrated from $\lambda = 400$ - 700 nm analogous to the measurements with InGaN NWH electrode. (b) PL spectra of the nitridated silicon substrate and GaN NWs for excitation with a laserdiode of $\lambda_{exc} = 405\,nm$. GaN NWs show additional features in comparison to the spectrum of the substrate. The integrated wavelength range for the measurement in (a) is indicated in grey.

The sub-band gap excitation of GaN NW electrodes results in an anodic photocurrent that is increased in the presence of 1 mM AA and 1 mM UA. Additionally, the dark current was increased in the presence of ascorbic acid and uric acid (for $U_C = -0.5\,V$, data not shown) as it was found for InGaN NWH samples. The anodic PC as well as the increase of the anodic PC can be ascribed to a photocurrent by surface states.
The transient PL intensity is correlated to the PL of the substrate since the GaN PL is comparable to that of the silicon substrate (cf. figure 3.19(b)). The contribution of the PL intensity of the substrate to the PL spectra of GaN NW and InGaN/GaN NHW samples is insignificant. The presence of the AA and UA does not alter the substrate PL intensity. Thus, the oxidation of the molecules proceeds at the InGaN part.
Due to the sub-band gap excitation, the increase of the dark current as well as the increase of the PC in presence of the molecules can be explained by either a passivation of surface states or an acidic dissociation. As a result, the barrier height is reduced and the I/V-curve shifts which increases the reverse current.

The intensity modulation of the PL signal can only be ascribed to charge transfer mechanisms and the variation of radiative and non-radiative recombination processes since other reasonable mechanisms have been considered, but are not consistent with our findings. The shape and the energetic position of the PL intensity peak do not change in presence of the molecules. Furthermore, neither the addition of AA or of UA changes the transmission properties of the electrolyte solution in the relevant spectral region. Besides, for an absorption by the molecules the contrary effect, the decrease of the PL intensity, would be expected. Additonally, transients with nitridated silicon as working electrode reveal

that the observed increases of the PL intensity and the photocurrent are effects which are correlated to the use of InGaN/GaN NWHs electrodes. The PL intensity increase with the nitridated silicon in presence of AA and UA is less than 0.25 %. The changes of the PL intensity in presence of 1 mM UA and a buffer solution with 1 mM AA and 1 mM UA are even smaller. Thus, the contributions of the molecules´ luminescence to the InGaN luminescence can be excluded.

Simultaneous Detection of Ascorbic Acid, Uric Acid and Hydrogen Peroxide

Many biosensors allow the detection of only one biomolecule. InGaN/GaN NWHs with their surface sensitivity due to the surface band bending modulation enable the selection/adjustment of the working point. As a consequence, an almost molecule-independent detection of oxidation and reduction processes is possible. The bias-dependent results show that by defining the electrochemical working point, the pattern of sensitivity can be adjusted and thus, the selectivity can be increased.
AA can be detected with 1 mM UA and H_2O_2 in the background. According to the results in figure 3.15, $U_C = 0.1$ V is selected as working point as AA showed a larger PL intensity increase than UA at that potential. In contrast to that, the PL intensity in presence of H_2O_2 is constant. The results of the detection of ascorbic acid are shown in figure 3.20.

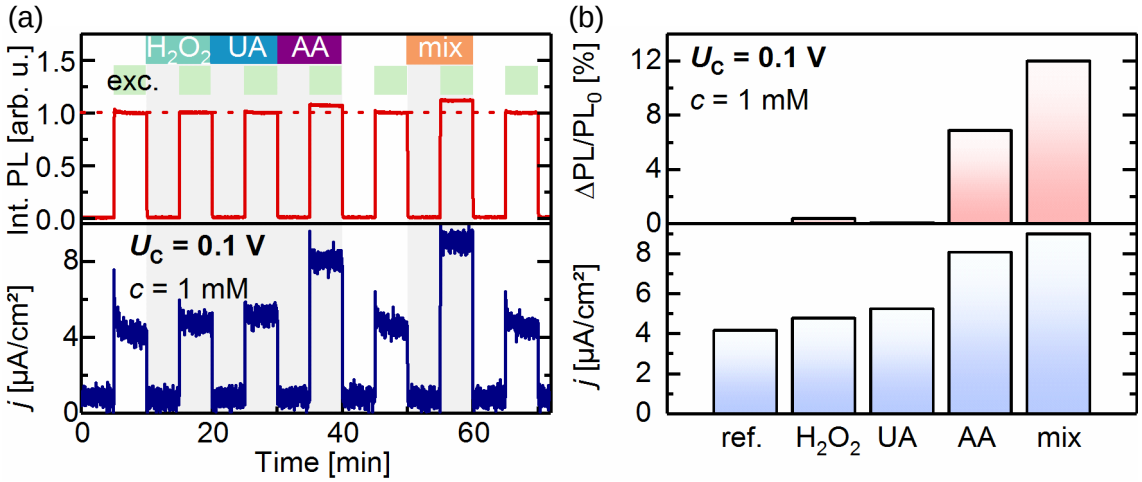

Figure 3.20: (a) Detection of AA in the presence of UA and H_2O_2. By adjusting the working point to $U_C = 0.1$ V, the PC density and the PL intensity increase only in presence of ascorbic acid. This allows the distinct signal change assignment of a mixture sample solution to AA. (b) Summary of changes of the ascorbic acid detection. The concentration of the molecules amounts to 1 mM each. The PL intensity is depicted as relative PL change. The current density is plotted as maximal current density. The mixture ("mix") contains 1 mM H_2O_2, UA and AA each.

In the transient measurement shown in figure 3.20, the PL intensity and the current are measured with and without the presence of 1 mM of the molecules in the buffer solution each and then as a mixture of 1 mM H_2O_2, 1 mM UA and 1 mM AA ("mix"). The current density increases in the presence of all the different molecules. The current density of the

mixture represents the sum of the single current densities. The detection of AA is accomplished by the PL intensity increase due to the presence of ascorbic acid. The summary in figure 3.20(b) indicates the unambiguous identification of 1 mM AA in the mixture due to the distinct PL change with UA and H_2O_2 in the background.

At a bias potential of $U_C = 0.1\,V$, the conduction and valence band possess an upward SBB, *i.e.*, there is only weak transfer of majority carriers between the NW electrode and the electrolyte solution without photoexcitation (cf. figure 3.13). In the case of photoexcitation, the electrons from the solution can be transferred into the NW, resulting in an anodic photocurrent. In contrast, accumulated holes at the surface enable oxidative reaction of near-surface molecules. The anodic PC enhancement in presence of AA, UA and H_2O_2 is attributed to the oxidative conversion of the molecules by photo-excited holes. The photocurrent increase is $\Delta PC(AA) > \Delta PC(UA) > \Delta PC(H_2O_2)$. In the discussion of figure 3.15, this finding was attributed to the respective differences in band alignment. The charge transfer rate is enhanced for those molecules with the redox level being higher in energy. As opposed to the photocurrent, the increase of the PL intensity cannot be explained by the hole transfer mechanism as the only non-radiative path. The dissociation of AA is enhanced in comparison to UA and H_2O_2 ($pK_a(AA) < pK_a(UA) < pK_a(H_2O_2)$). Thus, positive surface charges are introduced which reduce the SBB and increase the PL. To demonstrate that the nanowire heterostructures cover a wide range of molecule detection, the detection of hydrogen peroxide in the mixture of 1 mM H_2O_2, 1 mM UA and 1 mM AA is shown. For this purpose, the working point of the NWH electrode was adjusted to $U_C = 0.7\,V$ to enable the reduction of hydrogen peroxide (cf. figure 3.15). At this bias, the PL intensity increases in presence of AA and UA whereas it decreases in presence of H_2O_2. A PC decrease in the presence of H_2O_2 was found, whereas it did not change in the presence of AA and UA. The results are shown in figure 3.21.

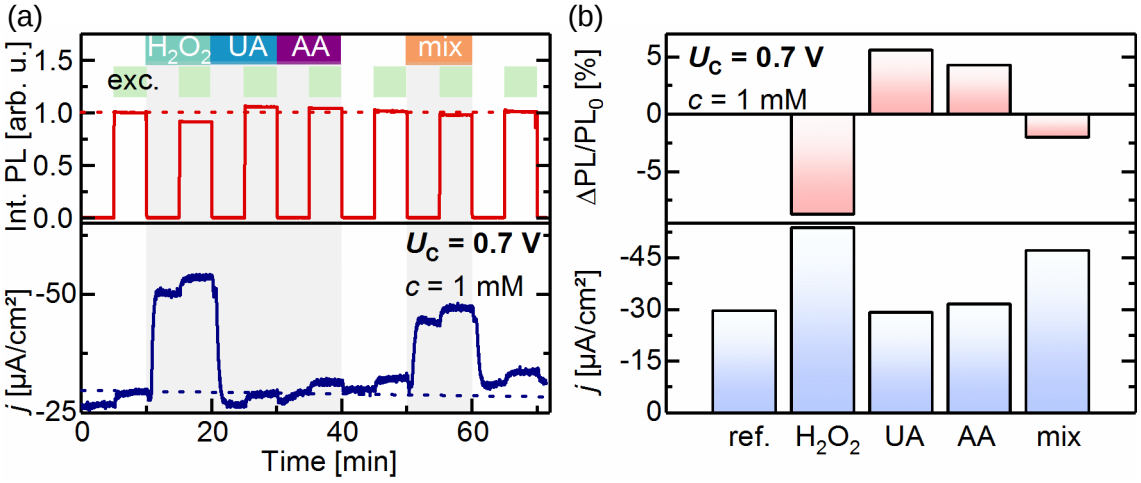

Figure 3.21: (a) Detection of 1 mM H_2O_2 in the presence of 1 mM AA and UA due to the adjustment of the working point. At $U_C = 0.7\,V$, a H_2O_2 tracing is possible due to shifting the electrodes´ potential from oxidation to reduction potential. (b) Summary of the changes of the H_2O_2 detection. The concentration of the molecules amounts to 1 mM each. The PL intensity is depicted as relative PL change. The current density is plotted as maximal current density. The mixture ("mix") contains 1 mM H_2O_2, UA and AA each.

At the selected bias of $U_C = 0.7\,V$, the presence of hydrogen peroxide results in an increase of the dark current. The dark current in presence of AA and UA does not alter. Due to the presence of H_2O_2, AA and UA the cathodic photocurrent increases. Here, this PC increase is significantly larger for H_2O_2 than that of uric acid and ascorbic acid: $\Delta PC(H_2O_2) > \Delta PC(AA) > \Delta PC(UA)$. The PL and current responses are summarized in figure 3.21(b). The summary reveals that the PL intensity shows a strong decrease in the presence of hydrogen peroxide while a weaker increase is found for the presence of UA and AA. Hence, for a mixture of all molecules being present, the PL also decreases, thus, the decrease of the PL intensity in the mixture can unambiguously be attributed to the presence of hydrogen peroxide.
At high U_C, the surface band bending is strongly reduced and the bands at the surface are almost flat. In this case, photo-excited minority charge carriers do not accumulate at the surface. Without photoexcitation, the charge transfer between the semiconductor NW electrode and the electrolyte solution can only be conducted by majority carriers. Electrons from the conduction band edge are transferred into the redox level of the molecules in the solution. This is the reason for the cathodic dark current without molecules in the buffer solution. The cathodic dark current increases in presence of hydrogen peroxide according to the following reduction reaction:

$$H_2O_2 + 2 \cdot e^- \rightarrow 2 \cdot OH^-.$$

Concurrently, the formed hydroxide ion can alter the surface band bending. The effective SBB increases and the radiative recombination of photo-excited carriers, *i.e.*, the PL intensity, decreases in analogy to a pH increase of the solution. In contrast to the findings for H_2O_2, the PL intensity in presence of AA and UA increases which can be explained by a positive surface charge due to proton adsorption after acidic dissociation that slightly decreases the SBB. The observed PL change is only below $\Delta PL < 0.05\,\%$ since for high U_C, an additional positive surface charge has little influence. The cathodic photocurrent is only slightly enhanced in comparison to the buffer solution without molecules during excitation. The cathodic current in presence of AA is already increased before the excitation which sustains the change of the barrier height due to proton adsorption or interaction with surface states.

3.2.4 Summary and Conclusion

InGaN/GaN NWHs as optochemical electrodes enable the application of an electrochemically well-defined working point with the result that oxidation and reduction processes can be induced in a controlled manner. As a consequence, these electrodes allow for the detection of ascorbic acid, uric acid and H_2O_2 by simultaneously quantifying the magnitude of photocurrent and photoluminescence intensity and for adjusting a bias-dependent sensitivity and selectivity pattern.
Even at a low potential of $U = 0\,V$, 1 mM ascorbic acid, uric acid and hydrogen peroxide

showed a sufficient increase of the anodic photocurrent due to an oxidative conversion. The anodic photocurrent with the highest sensitivity was found for ascorbic acid with about $59\,\mu\mathrm{A/mMcm^2}$. The sensitivity of uric acid was approximately $15\,\mu\mathrm{A/mMcm^2}$. Hydrogen peroxide demonstrated the smallest sensitivity of the anodic photocurrent with maximal $2\,\mu\mathrm{A/mMcm^2}$. The photocurrent of H_2O_2 was enhanced in alkaline solutions. In contrast, in acidic solutions the photocurrent of H_2O_2 was attenuated due to proton formation. The photocurrent increase in the presence of ascorbic acid, uric acid and hydrogen peroxide was increased for anodic bias voltages. The PL intensity enhancement in presence of ascorbic acid, uric acid and hydrogen peroxide slightly increased with anodic bias voltage.

The charge transfer between InGaN/GaN NWH electrodes and aqueous electrolytes is in analogy to a Schottky contact. It was demonstrated that the presence of AA, UA and H_2O_2 decreases the barrier height with the result that the dark current as well as the PL intensity increase. For this purpose, dark current measurements were performed which revealed that the magnitude of the change is related to the acidity characteristic of the molecule. This finding was investigated by simultaneous PL and PC measurements with the variation of the applied bias and the concentration. The results confirmed the modulation of the barrier height as cause of the PC increase by concurrent PL increase. The PL increase (SBB reduction) was found to be more pronounced at anodic bias and increased with the concentration of the respective molecules. For the variation of the bias, AA showed the largest increase in PC and PL whereas the presence of UA resulted in the largest PL increase with increasing concentration. The concentration-dependent PC increase was the largest in presence of AA. This shows that these measurements allow only for a static monitoring of the alteration of a complex interfacial composition. However, these measurements enable the determination of the change of the interfacial charge for a dynamic equilibration between oxidation and dissociation.

Next to the proton concentration as one parameter that defines the charge transfer between the NW electrode and the molecules, the reduction of the barrier height by the passivation of surface states is proposed to be a crucial non-radiative mechanism. The luminescence modulation of the PL intensity signal is ascribed to charge transfer mechanisms and the variation of radiative and non-radiative recombination processes since other reasonable mechanisms are not persistent with our findings.

Finally, the successful detection of AA and H_2O_2 in mixtures of AA, UA and H_2O_2 was demonstrated. The application of low cathodic bias voltage ($U_C = 0.1\,\mathrm{V}$) enables the detection of ascorbic acid in a sample solution with uric acid and H_2O_2 in the background. For these conditions, all three investigated molecules showed an increase of the anodic photocurrent which is attributed to an oxidative conversion. In contrast, only ascorbic acid led to a simultaneous increase of the PL intensity. As a result, by means of the coincident PL intensity and the PC increase, ascorbic acid can selectively be detected. Moreover, by the application of a large cathodic bias voltage ($U_C = 0.7\,\mathrm{V}$), the distinct detection of hydrogen peroxide with AA and UA as background molecules is possible. In presence of hydrogen peroxide, the cathodic current strongly increased which was accompanied by a decrease of the PL intensity. Here, the increase of the cathodic dark current was attributed

to the reductive conversion of hydrogen peroxide. The reduction of H_2O_2 without external photoexcitation results in the formation of hydroxide ions. The presence of hydroxide ions is comparable to a change of the local pH. Thus, the effective surface band bending increases and the PL intensity decreases. Since the cathodic photocurrent in presence of uric acid and ascorbic acid were similarly increased, the different signs of the PL intensity changes ensure the discrete detection of H_2O_2 since the PL intensity increased in presence of ascorbic acid and uric acid. The bias-dependent measurements demonstrated that the determination of AA in a solution with UA is possible by the adjustment of the working point since the molecules possess different onset potentials.

The simultaneous PL and PC measurement with InGaN/GaN NWH electrodes enables the detection of AA, UA and H_2O_2. The change of the SBB by the modulation of surface charge was attributed to the introduction of positive surface charges such as the adsorption of protons. For the chemical identification of the original cause further experiments involve the PC and PL determination for a variation of the exchange speed of the electrolyte solution that changes the equilibrium of chemical species and reaction products in the vicinity of the surface, *id est*, the composition of the interphase. Assuming that the proton concentration due to dissociation is the determining parameter, the observed effects should be more (less) prominent with slower (higher) speed. In addition, the passivation of the surface states by the investigated molecules can be studied by the deposition of passivation layers of ultra-thin oxides such as TiO_2 or CeO_2 [23]. TiO_2 demonstrated to passivate the surface states with the result that the PC enhances whereas the CeO_2 coating resulted in reduction of the PC due to defect recombination within the passivation layer [23].

3.3 Novel Photoresponsive Materials Based on Charge Separation Molecules and GaN Nanowires

The development and engineering of molecular photovoltaic devices has attracted much attention in chemistry, physics and interdisciplinary research [135, 136]. In terms of device design, the number of new and advanced approaches is continuously increasing. As essential requirement for an efficient photovoltaic unit with a high quantum yield and high efficiency, a long-distance charge separation (CS) within the molecules with simultaneously slow charge recombination kinetics is required. To study photo-induced electron transfer processes, usually donor-acceptor (D-A) linked frameworks are investigated under well-defined conditions by analysis in electrolyte solutions. In that line, systems with porphyrin units for the electron donation after photoexcitation and fullerene units as electron acceptors have been proven to present an appropriate charge separation system with a long life time ($t_{\text{life}} = 0.57$ - $34\,\mu$s [137]) and high quantum yields ($\Phi_{\text{quantum}} = 0.42$ - 1 [137]). The very efficient photo-induced electron transfer (ET) between the porphyrin and the fullerence is realized due to the small reorganization energies of the fullerene unit. In contrast, D-A systems based on aromatic systems have higher reorganization energies [137, 138] which diminish the CS performance. Long-distance CS is only realizable in ET systems with multiple transfer steps [137] that allow of at least three charge transfer processes within the molecule. Here, a life time of $34\,\mu$s ($t_{\text{life}}(\text{ZnP}^{\bullet+}\text{-H}_2\text{P-C60}^{\bullet-}) = 34\,\mu$s, $t_{\text{life}}(\text{Fc}^{\bullet+}$-ZnP-C60$^{\bullet-}) = 16\,\mu$s) is achieved and the quantum yield can be increased to $\Phi_{\text{quantum}} = 0.99$ ($\Phi_{\text{quantum}}(\text{ZnP}^{\bullet+}\text{-H}_2\text{P-C60}^{\bullet-}) = 0.40$, $\Phi_{\text{quantum}}(\text{Fc}^{\bullet+}\text{-ZnP-C60}^{\bullet-}) = 0.99$) [137].
Among the different approaches of molecular photovoltaic devices, a very promising attempt was demonstrated with fullerene-zinc porphyrin-ferrocence (C60-ZnP-Fc) triad molecules covalently attached on indium tin oxide (ITO) electrodes [52]. The photoelectrochemical analysis yielded a life time of the charge separation state of $16\,\mu$s and a quantum yield of 11 % for photocurrent generation [52].
In this work, GaN nanowires (NWs) with self-assembled monolayers of C60-ZnP-Fc triad molecules are studied as photovoltaic electrodes and new photoresponsive material with advanced readout mechanisms. The influence of the charge separation of the covalently linked molecule on the GaN photocurrent as well as on the PL intensity are investigated. Group III-nitride materials are ideally suited for molecular photoresponsive devices since they demonstrate a high electrochemical stability [13–15] which enables the analysis in electrolyte solutions representing well-defined conditions. Furthermore, as three-dimensional material, nanowires have an increased surface-to-volume ratio in comparison to two-dimensional materials. The electric field in the SCR of GaN NWs can be adjusted by the selection of a proper electrochemical working point and they allow the operation in a broad bias range [12]. The GaN surface enables the covalent linkage of organic molecules on the surfaces by immobilization [16, 18, 19].
It is shown that triad molecules can be covalently immobilized on GaN NW surfaces. A new multi-step modification method was developed and the success of the immobilization was confirmed for GaN substrates by different methods such as contact angle analysis,

atomic force microscopy and X-ray photoelectron spectroscopy (XPS). The GaN NW electrodes feature a stable photocurrent generation without the use of an electron sacrificer. In addition, the simultaneous measurement of photocurrent density and PL intensity allows the relation of signal magnitudes to the individual steps of charge separation reactions.
In the following sections, the properties of the C60-ZnP-Fc molecules as well as the surface modification route and the setup for the photoelectrochemical characterization are presented. The first part of the results includes the verification of the surface modification by optical absorption and XPS measurements. In the second part, the photoelectrochemical characterization with simultaneous transient PL and photocurrent measurements is presented.

3.3.1 Charge Separation of Donor-Acceptor Linked Molecules

The charge separation requires a donor-acceptor molecule pair. For this purpose, photosensitizers as electron donors and electron acceptors are neccessary. Porphyrins and porphyrin derivates are known to be appropriate sensitizers regarding their absorption properties in the visible spectral range of light. Additionally, by the modulation of the molecular design, the redox properties can be tuned [135]. Phorphyrins are large molecules with π-aromaticity. They possess both, proper electron donor and acceptor characteristics, and are used as sensitizers for photoelectrochemical applications such as solar cells [139] and also for biological sensing [135, 140]. Porphyrin units show a distinct absorption with a strong Soret band from around $\lambda_{\text{Soret}} \approx 400$ - 450 nm and a weaker Q-band at $\lambda_{\text{Q}} \approx 500$ - 650 nm [139]. These absorption bands originate from $\pi \rightarrow \pi^*$-transitions [139].
While porphyrins are used as electron donors, fullerenes (C60) act as electron acceptors. They possess a large and rigid carbon cage. This is the reason why C60 molecules have small internal reorganization energies [138]. As a consequence, the electron acceptance is accelerated and the charge recombination (CR) is decelerated so that a stable charge separation state develops [141].
The photoexcitation of the fullerene core causes a charge separation between the zinc porphyrin unit and the C60 singlet state or the C60 triplet state [137]. By excitation of C60 with UV light or light of wavelengths in the visible range, the singlet states are occupied ($E = 1.13$ V vs Ag/AgCl [142]). The singlet excited state only possesses a short life time of nanoseconds ($t_{\text{life}} = 1.2$ - 1.4 ns [143]). After population, C60 converts to the triplet excited state via intersystem crossing [144] which has a life time of tens to hundreds of μs ($E = 0.84$ V [142], $t_{\text{life}} = 20$ - 140 μs [143]). The electron transfer from the donor molecule to the fullerene as acceptor is reversly accompanied by a hole transfer from C60 [145].
In general, photoexcitation of fullerenes results in the formation of $C60^{\bullet -}$ [146] and $D^{\bullet +}$ where D is the donor molecule [146]. There are two different charge transfer paths for the generation of this excited state which are shown in figure 3.22.

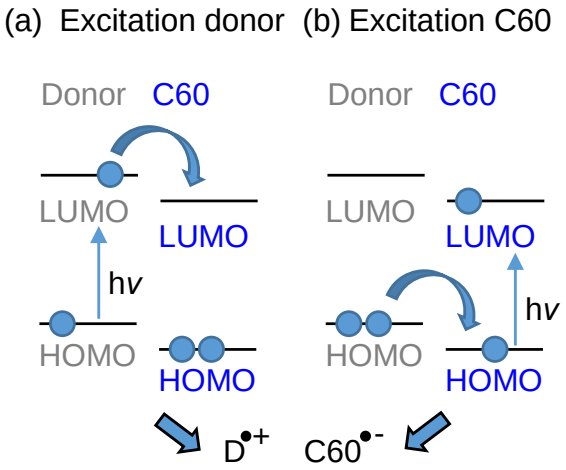

Figure 3.22: Schematic presentation of the photo-induced electron transfer for the donor/C60 system for the photoexcitation of (a) the donor molecule or (b) the fullerene.

In the case of photoexcitation of the donor molecule (cf. figure 3.22(a)), the donor molecule is excited and the electron on the HOMO level is transferred to the LUMO level [146]. Then, the electron from the donor LUMO level is transferred to the LUMO level of C60 [146]. In contrast, for direct excitation of C60, the electron of the HOMO level of C60 is excited into the LUMO level of C60 and electrons of the HOMO level of the donor can be transferred into the half-vacant HOMO level of C60 [146]. Both photo-induced electron transfer processes result in the radical ion generation of $D^{\bullet+}$ and $C60^{\bullet-}$, but the transfer path is different and, among others, depends on the polarity of the solvent [146].
The excitation of C60 causes a broad absorption band in the spectrum. The absorption of C60 in hexane solution was reported to span the range from $\lambda_{abs} = 200\text{-}800\,nm$ and in benzene solution from $\lambda_{abs} = 200\text{-}650\,nm$ [147]. In ref. [148], the maximum at $\lambda_{abs,max} = 329\,nm$ is explained by a transition from the degenerate level at $E = -0.861\,eV$ to the ninefold degenerate level at $E = 3.019\,eV$ or from the fourfold degenerate level at $E = -0.451\ eV$ to the fivefold degenerate level at $E = 3.298\,eV$. An absorption at $\lambda_{abs} = 410\,nm$ is assigned to transitions from levels with a shell number of $L = 7\text{-}8$. Thus, with the absorption of C60 in the UV and visible range ($\lambda_{abs,max} = 329\,nm$ and $\lambda_{abs,max} = 404\,nm$), the photoexcitations of GaN and Zn porphyrin, involve an excited state of C60.
Triad molecules with a Zn porphyrin unit as photosensitizer, C60 as electron acceptor and ferrocene for the electron donation was chemically linked to the GaN NWs since this triad molecule shows a high quantum yield with almost 100 % efficiency and a life time of some microseconds [149, 150]. The molecule structure is shown in figure 3.23.

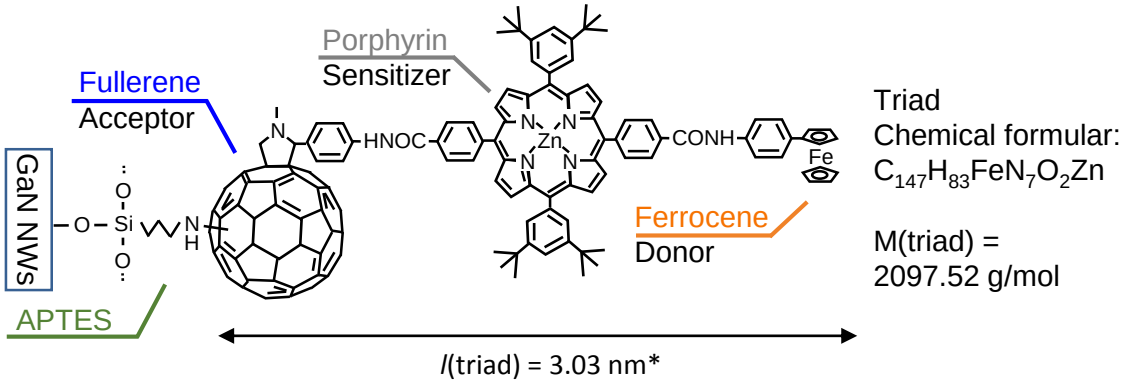

Figure 3.23: Molecule structure of C60-ZnP-Fc triad molecule coupled with APTES to the GaN NW surface. The length of the triad is $l_{\text{triad}} = 3.03\,\text{nm}$ * [137].

The triad molecule has a lenght of $l_{\text{triad}} = 3.03\,\text{nm}$ [137]. The molar mass is $M(\text{triad}) = 2097.52\,\text{g/mol}$. The excitation of these triad molecules results in a long-lived charge-separated state with $t_{\text{life}} \approx 16\,\mu\text{s}$ and a CS efficiency of $\Phi_{\text{quantum}} = 0.99$ [137]. The mechanism of the charge separation by excitation of the triad molecules linked to the GaN NW surface is schematically shown in figure 3.24.

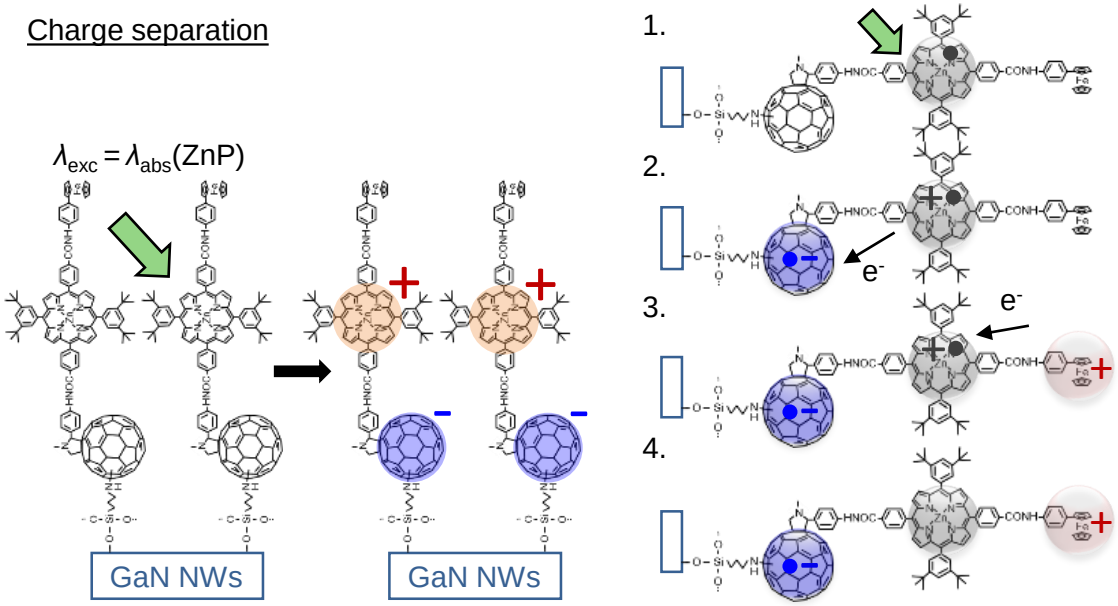

Figure 3.24: Schematic presentation of the charge separation mechanism by photoexcitation of the triad molecules linked to the GaN NW surface. On the left, the schematic shows the resulting charge separation after photoexcitation. On the right, the details on the charge separation mechanism are visualized.

For charge transfer processes between the triad molecules and the GaN NW electrodes, the alignment of the respective conduction or valence band energies with the HOMO/LUMO levels of the respective units in the triad molecules is essential. The band diagram with the valence and conduction band edges of GaN, InGaN and InN and the redox potentials of C60, ZnP and Fc are shown in figure 3.25.

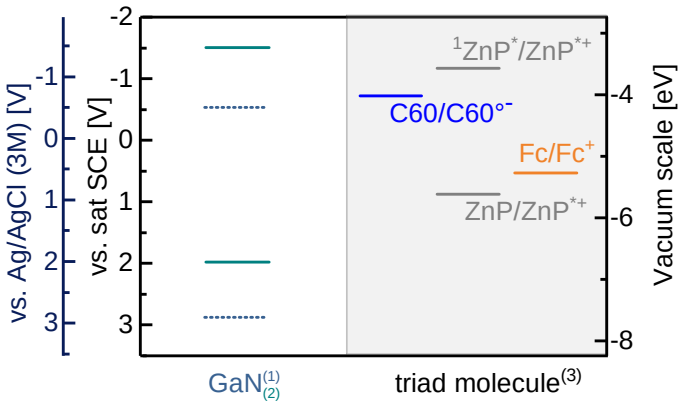

Figure 3.25: Band alignment of the valence and conduction band edges of GaN and the energy levels of the individual molecules of the charge separation donor-acceptor linked triad molecule C60, ZnP and Fc in units of the electrochemical [V] and vacuum scale [eV]. These values of the band edge and redox potentials are extracted or calculated according to refs. (1) [49], (2) [50] and (3) [52].

The band alignment shows that the electron transfer from the GaN conduction band to the redox level of C60 is possible. Furthermore, the photoexcitation of GaN allows the hole transfer from the GaN valence band into the redox level of C60.

3.3.2 Chemical Modification of GaN NW Electrodes with C60-ZnP-Fc

GaN NWs as group III-nitrides allow for surface functionalization by chemically linking of functional molecules via silanization after hydroxilation [18–21, 151]. GaN NWs were chemically modified using a multi-step modification route. The preparation of the samples was carried out in collaboration with the research group of Prof. Hiroshi Imahori in Japan (iCeMS, Dept. of Molecular Engineering, Kyoto University, Kyoto, Japan) where Dr. Gesche Müntze and Assoc. Prof. Yuta Takano improved the silanization processes. Assoc. Prof. Yuta Takano and M.Sc. Kazuya Nakao developed the synthesis reaction schemes for the charge separation molecules and carried out the chemical modification of the electrodes. Afterwards, they performed the basic characterization such as contact angle measurements (for GaN substrates), atomic force microscopy (for GaN substrates) and optical absorption measurements to confirm the successful functionalization.
The synthesis scheme is schematically shown for the GaN NW surfaces in figure 3.26. The real orientation is not considered as it could not be identified in the experiments carried out here.

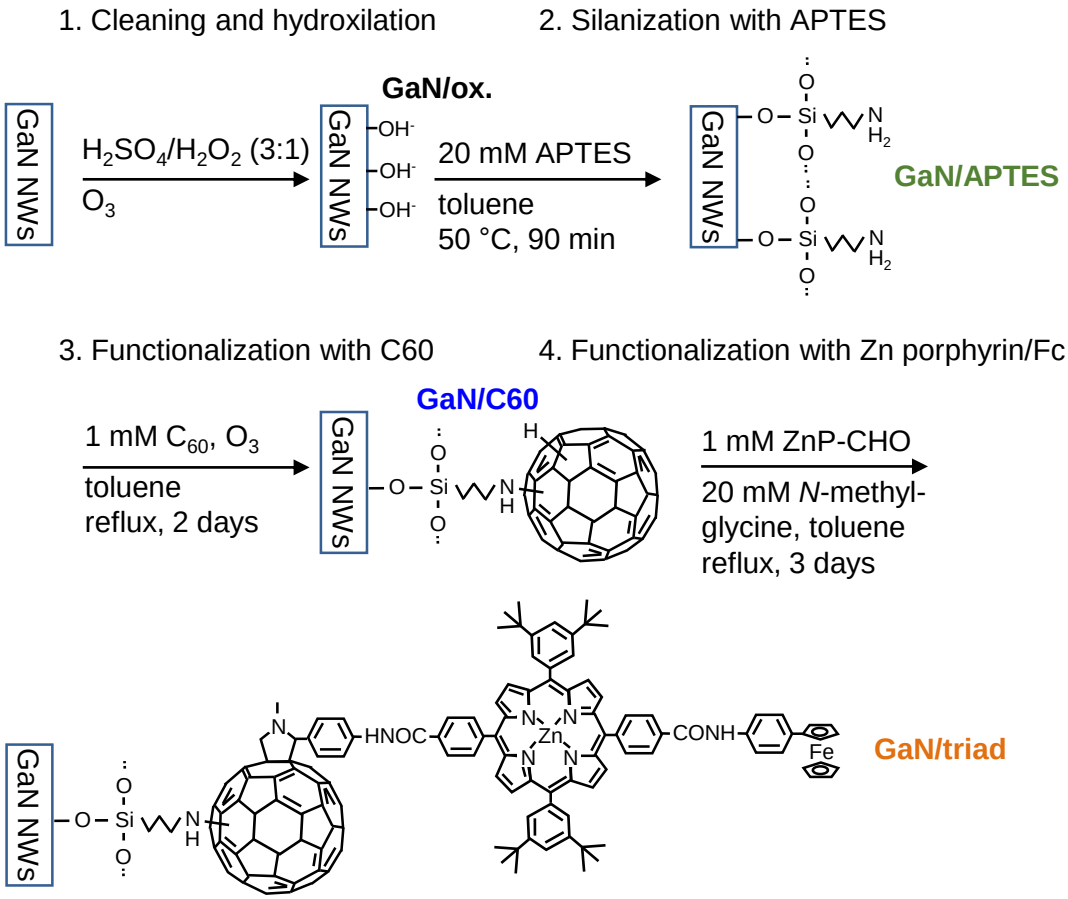

Figure 3.26: Synthesis scheme of charge separation molecules on GaN NW surfaces.

1. Cleaning and hydroxilation of the surface

An ultrasonic bath was used for cleaning. The GaN surface was cleaned by immersion of the samples in acetone and isopropyl alcohol each. Semiconductor materials possess a thin homogeneous native oxide layer in atmosphere [41,42]. The oxide layer as well as organic and inorganic contamination were removed and hydroxyl groups were introduced at the surface by wet chemical etching with piranha solution (a mixture of H_2SO_4:H_2O_2, 3:1) for $t = 20$ min. Finally, a purification with ozone for 30 min promoted the hydroxilation. The samples were dried and stored in a desiccator for $t \geq 2$ h before silanization. The resulted structure is GaN NWs-ox., denoted as "GaN/ox.".

2. Silanization with (3-Aminopropyl)triethoxysilane (APTES)

With their hydrophilic group, silane molecules bind covalently to the hydroxilated surfaces. (3-aminopropyl)triethoxysilane (APTES) with an alkyl chain length of 8.5 Å [152] was used. The silanization procedure was carried out according to the protocols in refs. [18,19]. The details of the silanization are described in appendix C. The silanization was carried out at a temperature of $\vartheta = 45\,°C$ for $t = 90$ min in an ultrasonic bath using a 20 mM APTES solution in anhydrous toluene. The thin water film on the sample surfaces at ambient air is sufficient to split off the ethoxy side chains and to hydroxylate the silicon atoms. A higher water concentration can lead to a premature polymerisation [41]. After silanization, the temperature was reduced to room temperature to stop the reaction. Subsequently,

the samples were cleaned using anhydrous toluene and isopropyl alcohol. To remove physisorbed APTES molecules, the samples were immersed in a solution of diluted acetic acid and mounted on a vortexer. After rinsing with water to remove the acid, the samples were dried and stored in a light protected sample box in a desiccator for $t \geq 12\,\mathrm{h}$. The resulted structure is GaN NWs-ox.-APTES, denoted as "GaN/APTES".

3./4. Functionalization with C60/C60-ZnP-Fc
The preparation was according to the procedure described in the preparation protocols of ref. [52]. First, the silanized samples were immersed into toluene solution with 1 mM C_{60} for two days under reflux. The resulted structure was GaN NWs-ox.-APTES-C_{60} and is denoted as "GaN/C60".
As second step, the addition of the ZnP part followed by the immersion of the samples in 1 mM ZnP-CHO and 20 mM *N*-methylglycinein in toluene for three days under reflux. The reaction resulted in GaN NWs-ox.-APTES-C60-ZnP-Fc which is denoted as "GaN/triad".

3.3.3 Photoluminescence and Photocurrent Measurement Setup

The photoelectrochemical characterization was performed using the electrochemical cell described in section 2.2.1. The three-electrode setup with GaN NWs as working electrode, a platinum tube as counter electrode and an Ag/AgCl (3 M KCl) reference electrode was used. The electrolyte solution was a 10 mM phosphate buffered saline (PBS) solution at pH = 7.
For the investigations of GaN NWs electrodes with photoresponsive molecules a microscope-enhanced PL (μ-PL) setup is used which allows the study of only small areas of the sample ($d_{\text{laser spot}} \approx 100\,\mu\mathrm{m}$ [39]). Different positions on the sample can be measured consecutively which preserves the surface functionalization. A photograph of the μ-PL setup is shown in figure 3.27.

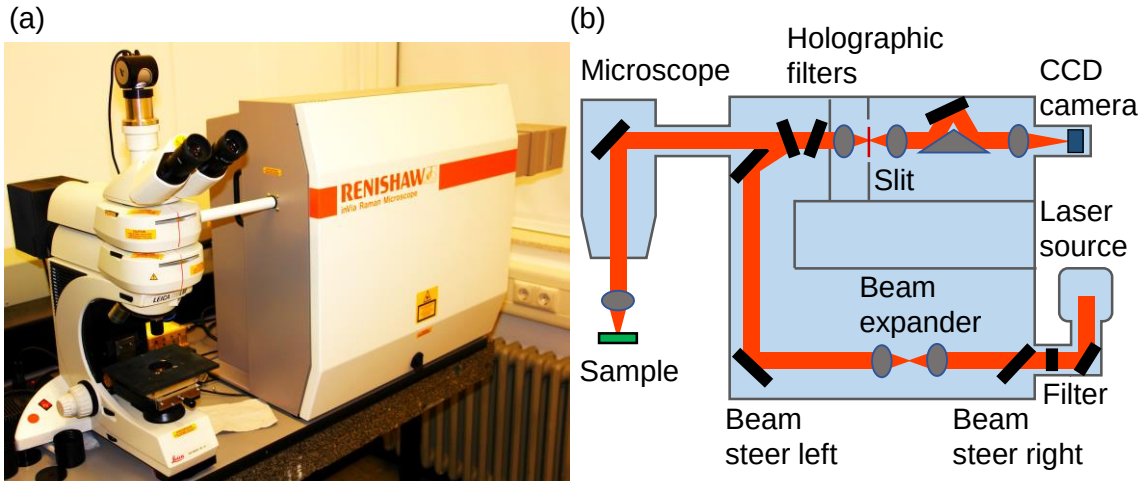

Figure 3.27: (a) Photograph of μ-PL setup. (b) Schematic presentation of μ-PL setup with indicated beam paths. The excitation wavelength was $\lambda_{\text{exc}} = 325\,\mathrm{nm}$. The light was focused with a tenfold UV objective lens.

The setup consists of an inVia Raman microscope from "Renishaw" (Renishaw, Birmingham, Great Britain) and an incident light microscope from "Leica" type "DM LM/P" (Leica Microsystems GmbH, Wetzlar, Germany). For excitation a HeCd laser with a wavelength of $\lambda_{\text{exc}} = 325\,\text{nm}$ in continuous wave mode was used.
The measurements were performed with a tenfold UV objective lens with a numerical aperture of $NA = 0.25$ and an effective focal length of $f = 20\,\text{mm}$. The working distance was $WD \approx 8\,\text{mm}$ [39]. After passing the window and the electrolyte solution in the measurement cell, the laser light is focused on the sample. As a result the laser spot has a size of $d_{\text{laser spot}} \approx 100\,\mu\text{m}$ [39]. The output power of the laser is $P_{\text{output}} = 30\,\text{mW}$ and the power on the sample is $P_{\text{sample}} = 25\,\text{mW}$. For the measurements, the incident laser power was reduced to 0.5 % and 5 %. For a reduction of the incident laser power to 5 %, the laser excitation power is calculated to $P_{\text{exc}} \approx 16{,}000\,\text{mW/cm}^2$.
The laser light was focused perpendicular to the sample surface and the PL intensity was collected in reflexion. The excitation light was filtered using an interference filter. For spectral analysis a spectrometer with a grating of 3600 lines/mm was used. Then the light was collected by a CCD camera.
There are two different measurement modes: The extended mode allows for energy-dependent measurement of the PL intensity. The static mode enables the measurement of PL transients. Here, the energy that correlates to the maximum of the PL intensity in the spectrum is used as a center of an integrated energy range. With $E_{\text{center}} = 3.41\,\text{eV}$, the PL intensity in the interval from $E = 3.355$ - $3.478\,\text{eV}$ was collected over time.
For the excitation of the charge separation molecules, a laserdiode with an excitation wavelength $\lambda_{\text{exc}} = 405\,\text{nm}$ was used. The laser head was fixed and the laserspot was focused on the sample surface. The distance from the laserspot to the sample was the same for each measurement sequence.
The transient PL data were evaluated using a Labview program written by a former member of the working group (Dr. Jörg Teubert).

3.3.4 Results and Discussion

In the following section, the analysis of the surface functionalization and the photoelectrochemical characterization of the hybrid system are presented. The latter is discussed in reference to the charge transfer within the triad molecules and between the triad molecules and the GaN NWs.

Verification of the Successful Surface Modification

The surface functionalization of the GaN NWs was carried out based on the procedure developed for GaN substrates [19]. Here, only results of the modified process for functionalization of GaN NWs are presented.

Ultraviolet-visible (UV/Vis) diffuse reflectance spectra [3] of the surface-modified GaN NWs with APTES, C60 and triad were measured using a "JASCO Corporation V-670" spectrometer (Jasco Deutschland GmbH, Pfungstadt, Germany) equipped with an integrating sphere. The baseline corrected spectra are shown in figure 3.28.

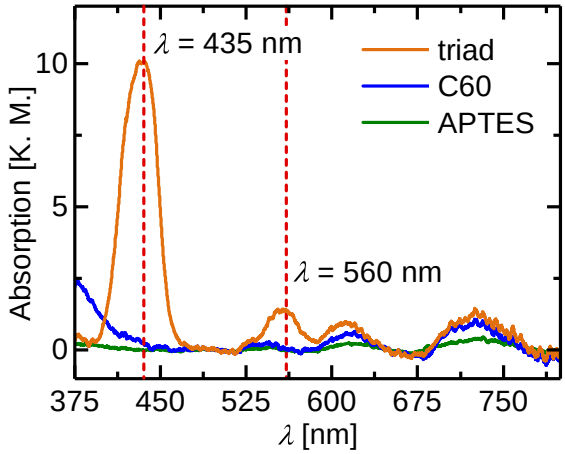

Figure 3.28: Baseline corrected reflective UV/Vis absorption spectra of GaN NWs with APTES, GaN NWs with C60 and GaN NWs with triad molecules. Absorption peaks of the Zn porphyrin part at $\lambda_{abs} = 435\,nm$ and at $\lambda_{abs} = 530\text{-}630\,nm$ are observed.

The absorption maxima of the Soret band at $\lambda_{Soret} = 435\,nm$ ($\lambda_{Soret} = 400\text{-}450\,nm$ [139]) and the Q-band from $\lambda_{Q} = 530\text{-}630\,nm$ ($\lambda_{Q} = 500\text{-}650\,nm$ [139]) were detected for the GaN NW samples modified with triad molecules according to the multi-step method. A quantitative comparison of the intensities is not possible due to different samples sizes. The absorption spectrum of the triad molecules on GaN NW electrodes is a superposition of the single components on GaN NW electrodes. The respective absorption maxima of C60 and ZnP are observed at the same wavelengths as the absorption maxima of the triad molecules. Thus, it can be concluded that there is no electronic interaction [137].
X-ray photoelectron spectroscopy (XPS) measurements were performed to evaluate and quantify the chemical composition of the modified surfaces of GaN NWs [4]. The zinc porphyrin part was investigated by the measurement of the $Zn2p_{3/2}$ signal and the ferrocene part in the molecule by the measurement of the Fe2p signal. The C1s signal allows the quantification of organic molecules on the surface such as it is the case for APTES or C60. The measurement of the $Ga2p_{3/2}$ indirectly shows the amount of the organic elements since it represents the shielding of the GaN surface atoms by these molecules. The signals were normalized to the Si signal at $E = 154\,eV$ and to the C1s signal at $E = 285\,eV$. The results are shown in figure 3.29. The intensities of the signals are stacked to illustrate the differences between the surface modifications.

[3] The reflectance spectra were measured by Assoc. Prof. Yuta Takano who worked in the group of Prof. Hiroshi Imahori (iCeMS, Department of Molecular Engineering, Kyoto University, Kyoto, Japan) by then.

[4] The XPS measurements were performed by Fabian Michel who is a member of the research group of Prof. Angelika Polity (Institute of Experimental Physics I, Justus Liebig University, Giessen, Germany). The evaluation of the results was made by Dr. Gesche Müntze, a former member of the research group of Prof. Martin Eickhoff (Institute of Experimental Physics I, Justus Liebig University, Giessen, Germany).

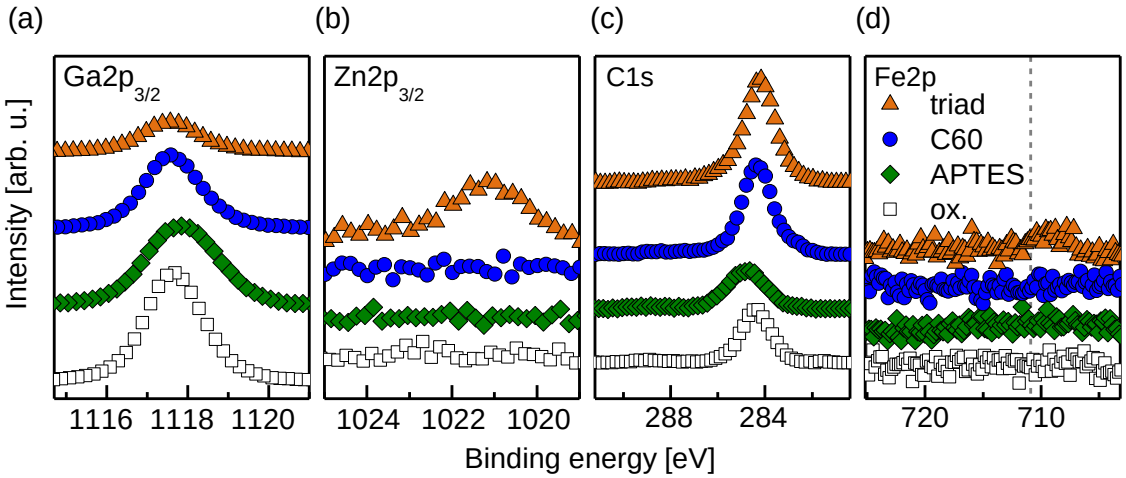

Figure 3.29: XPS measurements of GaN NWs (ox.), GaN NWs with APTES, GaN NWs with C60 and GaN NWs with triad molecules displayed in the binding energy intervals of interest of the (a) $Ga2p_{3/2}$ signal, (b) $Zn2p_{3/2}$ signal, (c) C1s signal and (d) Fe2p signal. The results verify the surface modification of GaN NWs with APTES,C60 and the triad molecules.

The highest intensity of the $Ga2p_{3/2}$ signal is found for the oxidized sample which serves as reference for the modified samples. The intensity of this peak decreases as the concentration of organic molecules on the surface increases: $I_{Ga2p_{3/2}}(\text{ox.}) > I_{Ga2p_{3/2}}(\text{APTES}) > I_{Ga2p_{3/2}}(\text{C60}) > I_{Ga2p_{3/2}}(\text{triad})$. Simultaneously, the peak intensity of C1s increases with increasing concentration of organic molecules, $I_{C1s}(\text{triad}) > I_{C1s}(\text{C60}) > I_{C1s}(\text{APTES or ox.})$, whereas the oxidized sample shows an intensity comparable to the APTES modified sample. The Zn porphyrin (cf. figure 3.29(a)) and the ferrocene part (cf. figure 3.29(d)) in the molecules were detected in the triad sample. The calculated quantities for GaN/ox., GaN/APTES, GaN/C60 and GaN/triad are summarized in table 3.2.

Table 3.2: Calculated quantities for GaN/ox., GaN/APTES, GaN/C60 and GaN/triad from the XPS measurements.

Surface modification	[Ga] [%]	[C] [%]	[Zn] [%]	[Fe] [%]
GaN/ox.	47.81	52.13	0.06	0
GaN/APTES	44.76	55.17	0.07	0
GaN/C60	24.69	75.24	0.07	0
GaN/triad	9.04	89.49	0.71	0.76

Based on the observed XPS binding energy distribution, the elemental quantities of the GaN NW electrodes can be determined. Since the calculated zinc ratio for GaN NW reference samples as well as for the samples modified with APTES and C60 is lower than 0.1 %, the presence of zinc is not likely. Due to the noise, the iron Fe2p peak is not identifiable for GaN/ox., GaN/APTES and GaN/C60 in the measured spectra and thus, cannot be detected. With surface concentrations of zinc and iron on the triad modified sample of [Zn] = 0.71 % and [Fe] = 0.76 %, the successful modification is determined.
Modified nitridated silicon surfaces, which were used as growth templates of the GaN

NWs, were also analyzed. These electrodes are investigated to evaluate the charge transfer between the working electrode and the triad molecules. Just as was is the case for the GaN NWs, the $Zn2p_{3/2}$ peak, the C1s peak and the Fe2p peak were analyzed [5]. Here, due to the absence of the GaN NWs, the $Ga2p_{3/2}$ region is not considered. The results of oxidized and triad modified samples are depicted in figure 3.30. The intensities of the signals are stacked to illustrate the differences between the surface modifications.

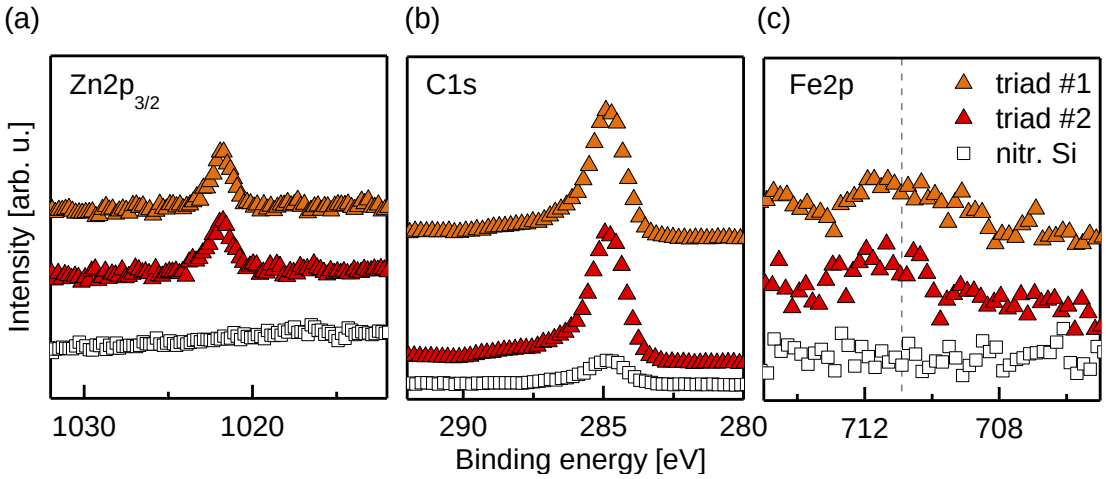

Figure 3.30: XPS measurements of nitridated silicon electrodes without surface modification as reference ("nitr. Si") and with triad molecules ("triad") displayed in the binding energy intervals of interest of the (b) $Zn2p_{3/2}$ signal, (b) C1s signal and (c) Fe2p signal. The presence of the ZnP and Fc part indicate the successful surface modification of the nitridated silicon samples with triad molecules.

The C1s peak intensity is increased for the triad modified samples due to the organic molecular composition of the triads. In addition, Zn and iron were detected in the triad modified sample. As a consequence, the surface functionalization of nitridated silicon electrodes as samples for reference measurements to investigate the role of GaN NWs for the charge transfer was accomplished. The calculated quantities of carbon, zinc and iron are summarized in table 3.3.

Table 3.3: Calculated quantities for nitridated silicon/ox. and nitridated silicon/triad from the XPS measurements.

Surface modification	[C] [%]	[Zn] [%]	[Fe] [%]
nitridated silicon/ox.	99.94	0	0.06
nitridated silicon/triad 1	99.32	0.52	0.16
nitridated silicon/triad 2	99.18	0.61	0.21

The surface concentrations of zinc and iron on the samples with triad molecule modification were quantifiable of the XPS spectra. The surface concentration of zinc and iron on the triad modified sample are quantified to $[Zn] = 0.57 \pm 0.06\,\%$ and $[Fe] = 0.19 \pm 0.04\,\%$.

[5] The XPS measurements were performed and evaluated by Fabian Michel who is a member of the research group of Prof. Angelika Polity (Institute of Experimental Physics I, Justus Liebig University, Giessen, Germany).

The calculated iron ratio for the nitridated silicon sample is again too low to take into account and the Zn content could even not be determined due to noise. For the triad sample a small iron content is observable in the spectra of the triad modified samples, especially in reference to the unmodified substrate. This concludes the presence of the triad on the nitridated silicon samples.

The surface modification of GaN NW and nitridated silicon samples could both be verified by optical absorption and XPS measurements. The detailed orientation of the triad molecules on the GaN NW surfaces is not clear, yet. Aggregation was observed by the shift of the porphyrin absorption maxima between molecules in solution and on ITO [52].

Photoelectrochemical Characterization of GaN Nanowires Modified with C60-ZnP-Fc

In the following section, the charge transfer between the donor-acceptor linked molecules and the GaN NWs is investigated.
Incident photon-to-current efficiency (IPCE) measurements were performed using the measurement system "Zahner TLS03" (ZAHNER-Elektrik, Kronach-Gundelsdorf, Germany) [6]. The intensity of the incident light was adjusted to $I = 95\,\%$. The results of the IPCE measurements at $U_C = -0.3\,\mathrm{V}$ in combination with the respective absorption spectra [7] are shown in figure 3.31.

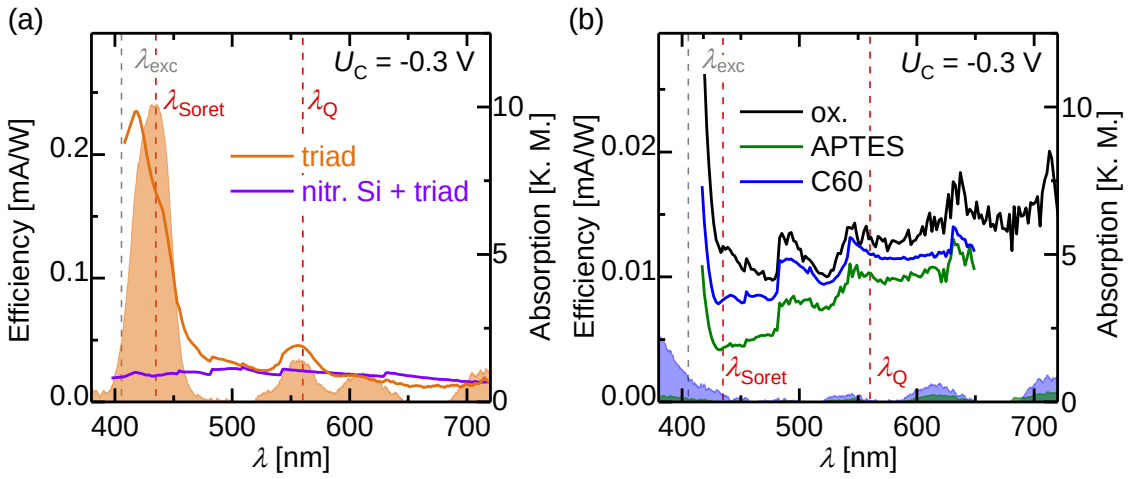

Figure 3.31: (a) Correlation of photon-to-electron conversion (efficiency) of GaN/triad and nitridated Si substrate with triad with the absorption spectrum of GaN/triad (filled curve) at $U_C = -0.3\,\mathrm{V}$. (b) Correlation of photon-to-electron conversion (efficiency) of oxidized GaN NW samples, GaN/APTES and GaN/C60 combined with the absorption spectra of GaN/APTES and GaN/C60 (filled curves) at $U_C = -0.3\,\mathrm{V}$. Note the different efficiency scale. At anodic bias potentials, the porphyrin units are the photoactive species and the charge transfer proceeds across the GaN NWs.

[6] The IPCE measurements were performed using the experimental setup from the research group of Dr. Roland Marschall (Institute of Physical Chemistry, Justus-Liebig-University, Giessen, Germany).

[7] The absorption spectra were measured by Assoc. Prof. Yuta Takano who worked in the group of Prof. Hiroshi Imahori (iCeMS, Department of Molecular Engineering, Kyoto University, Kyoto, Japan) by then.

The highest photon-to-electron conversion efficiency is found for the GaN NW samples with triad molecules. The GaN NW samples from the first synthesis step (ox. ≡ cleaning and hydroxilation) possess substantially lower efficiency without any spectral features. For this reason, the photocurrent generation is assigned to the presence of the triad molecules. Since the nitridated silicon substrates which were functionalized with triad molecules show a negligible efficiency in the relevant wavelength range ($\lambda_{\mathrm{Soret}} = 435\,\mathrm{nm}$ and $\lambda_{\mathrm{Q}} = 560\,\mathrm{nm}$), the photo-generated charge transfer processes take place across the GaN NW surface. The alignment of the absorption spectrum with the IPCE curve of GaN NWs with triad molecules from $\lambda = 380$ - $800\,\mathrm{nm}$ evidences that the porphyrin units are the photoactive species responsible for the photocurrent generation at anodic bias potentials. The IPCE measurements of GaN/C60 and GaN/APTES (cf. figure 3.31(b)) exclude the participation of the photoelectrochemical activity of either C60 or APTES to the photocurrent generation at this potential.

In addition, the correlation of photocurrent generation with the surface modification of GaN was investigated for cathodic bias potentials. The assignment of IPCE and absorption measurement in this bias range is relevant since the simultaneous PC and PL measurement shown below were performed at cathodic bias potentials. In figure 3.32, the IPCE curves and the absorption spectra of GaN/C60 and GaN/triad in reference to nitr. Si/triad and an oxidized GaN NW samples at cathodic bias voltages are shown.

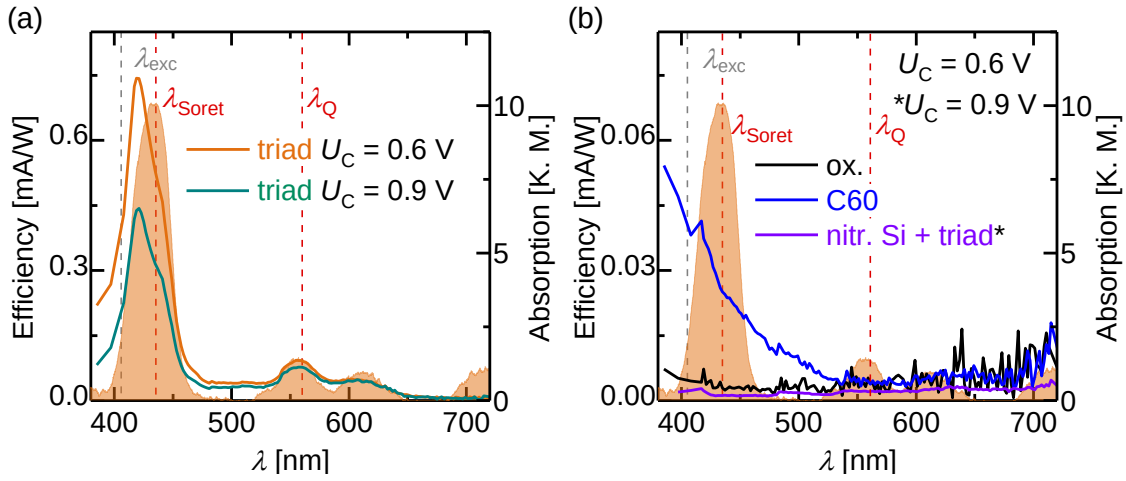

Figure 3.32: (a) Correlation of photon-to-electron conversion (efficiency) of GaN/triad at $U_{\mathrm{C}} = 0.6/0.9\,\mathrm{V}$ with the absorption spectrum of GaN/triad (filled curve). (b) Correlation of photon-to-electron conversion (efficiency) of oxidized GaN NW samples, GaN NWs with C60 and nitridated Si substrate with triad molecules as reference at $U_{\mathrm{C}} = 0.6/0.9\,\mathrm{V}$ with the absorption spectrum of GaN/triad (filled curve). Note the different efficiency scale. At cathodic bias, the porphyrin units are the prominent photoactive species and the charge transfer proceeds across the GaN NWs.

Also in this case, GaN NWs with triad molecules have the highest photon-to-electron conversion efficiency. In comparison, the efficiency of GaN/ox. is negligibly small. In contrast to the IPCE at anodic bias, at cathodic bias, the GaN NW samples modified with GaN/C60 indicate a photoactivity of C60 unless the efficiency is significantly smaller than that of the samples modified with triad. The IPCE measurement of GaN/triad aligns with

the absorption spectrum of the GaN NWs with triad molecules. Thus, at cathodic bias potentials, the porphyrin units are also the photoactive species and responsible for the cathodic photocurrent generation. With increasing U_C from $U_C = 0.6\,V$ to $U_C = 0.9\,V$, the incident photon-to-current conversion efficiency decreases. The IPCE curve of nitridated silicon samples with triad molecules proves that charge transfer occurs across the GaN NW surface.

Although C60 shows photoactivity at cathodic bias, the triad molecules generate the largest photocurrent at cathodic as well as at anodic bias. In this process, GaN NWs are important for the charge transfer. The IPCE measurements show an efficiency η of at least $\eta \geq 0.23\,mA/W$ at anodic potentials of $U_C = -0.3\,V$ and of $\eta \geq 0.74\,mA/W$ at cathodic potentials of $U_C = 0.6\,V$. These values are underestimated due to an incorrect calibration of the measurement device. The comparison of oxidized GaN NWs samples before and after the implementation of the new calibration yielded actual higher efficiencies. Since the changes are wavelength- and bias-dependent, the data shown above cannot be adjusted. However, the qualitative comparison of the samples with different surface treatment remains correct. The deviations are calculated to $\Delta IPCE(U_C = -0.3\,V) = 0.020$ - $0.055\,mA/W$ and $\Delta IPCE(U_C = 0.6\,V) =$ -0.010 - $0.016\,mA/W$. Based on the maximal efficiencies for the triad modified samples, this results in a percentage variance of the maximal deviation of approximately 24 % at $U_C = -0.3\,V$ and of approximately 2.16 % at $U_C = -0.6\,V$. Thus, the impact on the results at cathodic bias can almost be neglected, but for anodic bias the deviation is significant.

Chopped-light voltammetry (CLV) measurements were performed for photoelectrochemical characterization. For this purpose, the photocurrent density was measured as a function of the applied bias. The excitation light was chopped with a period of $t_{period} = 10\,s$ with a measurement frequency of 10 samples/s. The excitation power was adjusted to $P_{exc} = 90\,W/m^2$. The CLV results for excitation with a wavelength of $\lambda_{exc} = 429\,nm$, which is close to the absorption wavelength of the Zn porphyrin unit ($\lambda_{abs} = 435\,nm$), are shown in figure 3.33.

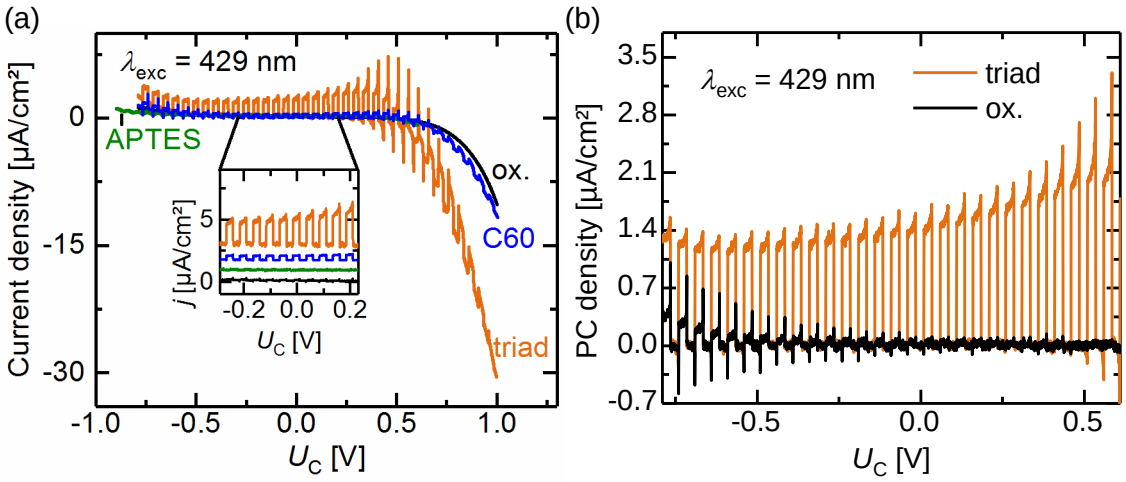

Figure 3.33: (a) CLV measurements of GaN/ox., GaN/APTES, GaN/C60 and GaN/triad from $U_C = -0.75 - 1\,V$ with $\lambda_{exc} = 429\,nm$. The GaN NW sample with triad molecules has a distinct anodic PC. The GaN NW sample modified with triad as well as the GaN NW sample modified with C60 do also show a cathodic PC. The current densities in the inset are stacked to illustrate the differences between the surface modifications. (b) Calculated PC density from the CLV measurements in (a) for GaN/ox. and GaN/triad. The dark current was fitted and subtracted for each sample modification. The anodic PC is enhanced for the triad modified sample.

The GaN NW sample with triad possesses a distinct anodic photocurrent which is significantly higher than the PC of the oxidized GaN NW sample. The PC of the oxidized sample is caused by a transfer of electrons into the electrolyte solution via surface states since sub-band gap excitation was used. In contrast to the findings of the IPCE measurement at anodic bias, the GaN NW sample modified with C60 also reveals an anodic PC. The anodic PC for the samples with APTES it is negligible (cf. inset in figure 3.33(a)). The photocurrent was calculated by the subtraction of the fitted dark current for the GaN NWs with triad molecules and the oxidized GaN NW samples (cf. figure 3.33(b)). The anodic photocurrent of the oxidized sample shows a small bias dependence. Here, the PC increases with increasing U_A starting at approximately $U_C \approx -0.2\,V$. The anodic PC of the GaN NWs with triad molecules is more pronounced for small values of U_C. The PC density yielded $PC_{max} \approx 2.20\,\mu A/cm^2$ at a bias potential of $U_C = 0.58\,V$ for the triad modified GaN NW samples.

The anodic PC of GaN modified with C60 demonstrates that C60 is photoactive. In this case, electrons are transferred from the fullerene to the GaN NW electrode. A stable anodic photocurrent for $\lambda_{exc} = 403\,nm$ was reported for gold electrodes that were chemically modified with self-assembled monolayers of C60, but with the use of ascorbic acid as electron sacrificer [142]. In that case, the electron transfer proceeded from the triplet states of C60, which are produced via intersystem crossing from the excited singlet state, to the metal electrode [142]. The details of mechanism of the charge transfer using GaN NWs as electrodes are not clear, yet. However, the PC generated by the fullerene is significantly smaller than the PC generated by the photoexcitation of the triad molecules. The anodic PC of the triad molecules can be caused either by a direct charge transfer via the fullerene

into the GaN NW electrode similar to the PC generation by C60. In addition, the current increase can be explained by the generation of a dipole at the interface due to the charge separation within the triad molecule which reduces the effective barrier height.
It is noticeable that the triad modified sample as well as the C60 modified sample do also show a cathodic photocurrent with PC(triad) > PC(C60). The anodic PC increases slightly with cathodic bias until the maximal charge transfer rate is achieved (point of change) and a cathodic current can be observed for higher cathodic voltages. The maximum cathodic current density in the investigated bias range was determined for the GaN NW electrodes with triad molecules to $j_{max} \approx$ -30.64 μA/cm^2 at $U_C = 1$ V. The increase of the cathodic PC increases with cathodic bias up to $U_C \approx 0.8$ V for the sample modified with triad molecules. The reference sample did not show a cathodic photocurrent. Only a dark current in the cathodic bias range is detectable which is due to an electron transfer from the conduction band into the electrolyte solution due to the reduced SBB. The cathodic photocurrent sustains that both the triad and the C60 modified sample are photoactive. The cathodic PC of the fullerene can be generated by the direct charge transfer of electrons. In the case of the triad molecules, the photoexcitation results in a charge separation state similar to a dipole. The formation of these dipoles decreases the effective barrier height and thus, the carrier transfer enhances. It is also possible that the charges from the triad molecule and the fullerene directly transfer since the excitation of the latter does not result in a dipole generation. However, the details on the reaction scheme are not clear yet, since this is the first time that photoactive molecules at the GaN NW surface are investigated.

To monitor and analyze the charge transfer between the GaN NWs and the triad molecules, a novel measurement procedure was introduced which is based on the simultaneous measurement of PL and PC. The idea is to modulate the PL and PC signal with the charge separation state of the triad molecule established by the use of an additional excitation source. The experiment is schematically shown in figure 3.34.

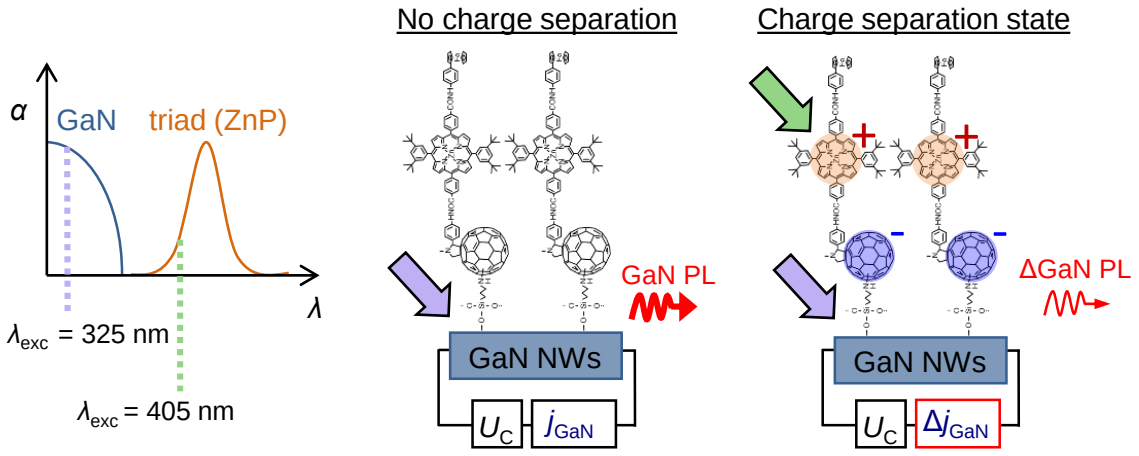

Figure 3.34: Schematic presentation of simultaneous PL and PC measurements with signal modulation due to charge separation by the triad molecules. The PL intensity and the current density j are transiently measured during generation of the charge separation state by additional excitation of the triad molecules.

In contrast to semiconductor materials such as GaN NWs, which feature an onset of absorption at a specific energy that in first approximation corresponds to the band gap energy, molecules possess resonant absorption characteristics that allow for excitation at specific wavelengths. The photoexcitation mainly of the GaN NWs, but also of C60, is realized by the use of an excitation wavelength of $\lambda_{\mathrm{exc}} = 325\,\mathrm{nm}$. A modulation of the PL and PC signal by the generation of a charge-separated state by excitation of the triad molecules (Zn porphyrin units) was performed by an additional excitation source with $\lambda_{\mathrm{exc}} = 405$ nm. The PL measurements were conducted at cathodic bias to avoid the anodic oxidation of GaN and the possible detachment of the triad molecule (cf. ref. [153]). The current density and the integrated (int.) PL intensity were transiently analyzed for different surface modifications and different excitation wavelengths. The results are depicted in figure 3.35.

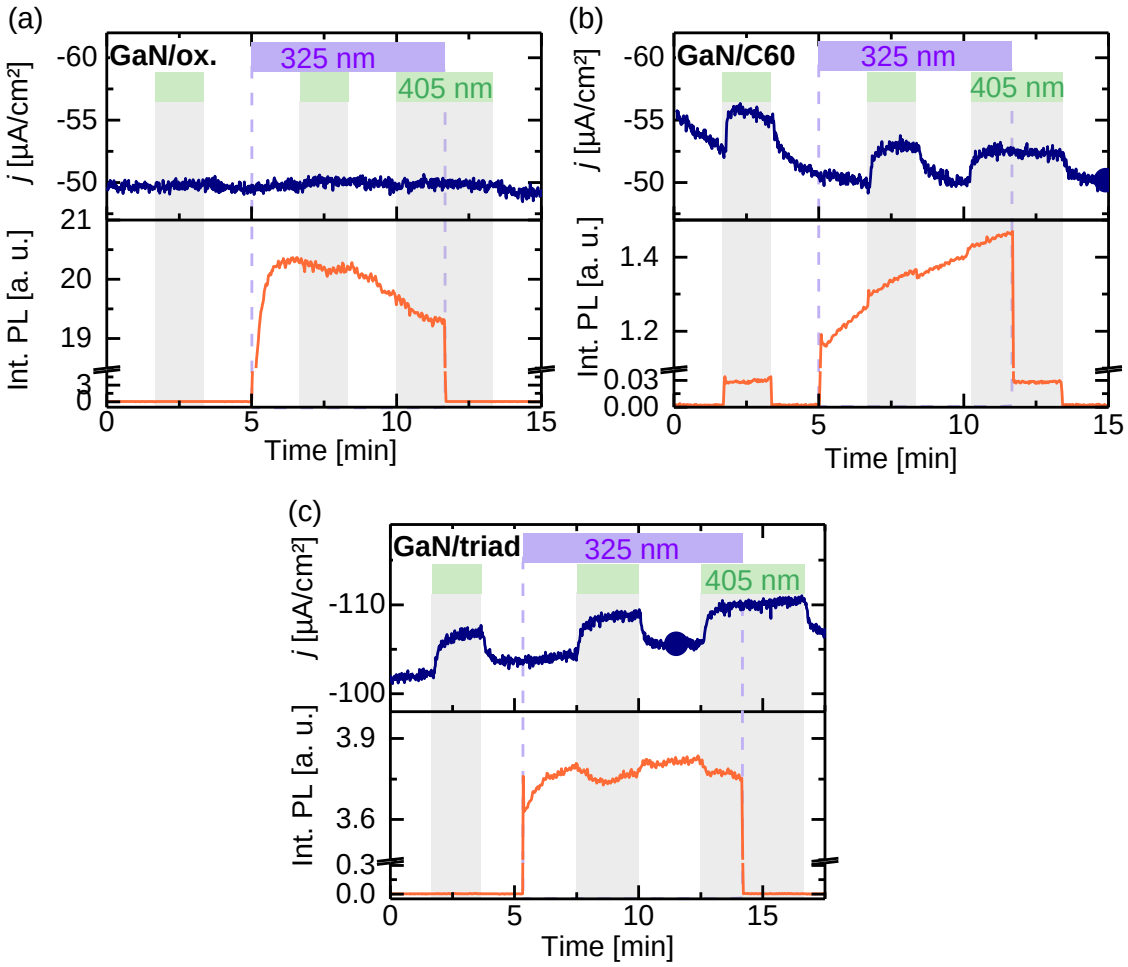

Figure 3.35: (a) Current density and integrated PL intensity of GaN/ox. at $U_C = 0.85\,V$ for different λ_{exc}. Only a dark current and no cathodic PC is observable. The PL intensity does not show a systematic change. (b) Current density and integrated PL intensity of GaN/C60 at $U_C = 0.85\,V$ for different λ_{exc}. A cathodic PC is observable for the excitation with $\lambda_{exc} = 405\,nm$. No PC is observed for the above band gap excitation. Additionally, the PL intensity increases for excitation with $\lambda_{exc} = 405\,nm$, possibly due to absorption/excitation of C60 and a charge transfer to the GaN NWs. (c) Current density and integrated PL intensity of GaN/triad at $U_C = 0.9\,V$ for different λ_{exc}. A cathodic PC is observable for the excitation with $\lambda_{exc} = 405\,nm$. No PC is noted for the above band gap excitation. The PL intensity decreases for excitation with $\lambda_{exc} = 405\,nm$, *i.e.*, when a cathodic PC is created.
The incident laser power ($\lambda_{exc} = 325\,nm$) was reduced to 5 % and the integration time was $t_{int} = 1\,s$.

The oxidized GaN NWs show a very small photocurrent when excited with above or sub-band gap excitation. The mean changes of the photocurrent are calculated for different transient measurements according to:

$$\overline{\Delta PC} = j(\lambda_1 \text{ and } \lambda_2) - j(\lambda_1).$$

with the excitation wavelengths $\lambda_1 = 325\,nm$ and $\lambda_2 = 405\,nm$.
The changes are $\overline{\Delta PC(GaN/ox.)} = -0.52 \pm 0.44\,\mu A/cm^2$ at $U_C = 0.8$ - $0.9\,V$. A dark current

of $j_{\mathrm{dark}} = $-50 μA/cm^2 is present. The mean relative GaN PL changes for the additional excitation with $\lambda_{\mathrm{exc}} = 405\,\mathrm{nm}$ are calculated according to

$$\overline{\Delta \mathrm{PL}_{\mathrm{rel}}} = [\mathrm{PL}(\lambda_1 \,\mathrm{and}\, \lambda_2)/\mathrm{PL}(\lambda_1) - 1] \cdot 100$$

for the different surface modifications with the excitation wavelengths $\lambda_1 = 325\,\mathrm{nm}$ and $\lambda_2 = 405\,\mathrm{nm}$.

For the investigated reference samples it is $\overline{\Delta \mathrm{PL}_{\mathrm{rel}}}(\mathrm{GaN/ox.}) = 0.48 \pm 1.72\,\%$ at $U_{\mathrm{C}} = 0.8$ - 0.9 V. However, the PL intensity does not systematically change for excitation with $\lambda_{\mathrm{exc}} = 405\,\mathrm{nm}$.

In contrast, a systematic change of the current density and the PL intensity is observed for both surface modifications (C60, triad molecules). For the GaN NWs modified with C60, a cathodic photocurrent due to the excitation with $\lambda_{\mathrm{exc}} = 405\,\mathrm{nm}$ is notable, in agreement with the CLV measurements reported above. In contrast, there is no photocurrent for excitation with $\lambda_{\mathrm{exc}} = 325\,\mathrm{nm}$. The change of the current density is $\overline{\Delta \mathrm{PC}(\mathrm{GaN/C60})} = -3.12 \pm 0.58\,\mu\mathrm{A/cm}^2$ at $U_{\mathrm{C}} = 0.85\,\mathrm{V}$ for the investigated samples. The PL intensity increases with additional sub-band gap excitation. This increase is attributable to the sub-band gap excitation and can possibly be related to the excitation of the C60 molecules. The PL intensity increases with $\overline{\Delta \mathrm{PL}_{\mathrm{rel}}}(\mathrm{GaN/C60}) = 2.54 \pm 1.21\,\%$.

The triad modified GaN NWs demonstrate a current increase for the excitation with $\lambda_{\mathrm{exc}} = 405\,\mathrm{nm}$ as also found in the CLV measurements. The change of the current density is $\overline{\Delta \mathrm{PC}(\mathrm{GaN/triad})} = $-7.32 $\pm$ 5.04 μA/cm^2. As it was also found for the C60 modified sample, there is no PC for pure above band gap excitation. In contrast to the result for GaN/C60, the PL intensity of GaN/triad decreases for additional excitation with $\lambda_{\mathrm{exc}} = 405\,\mathrm{nm}$ by $\overline{\Delta \mathrm{PL}_{\mathrm{rel}}}(\mathrm{GaN/triad}) = -1.40 \pm 0.62\,\%$ for the investigated samples at $U_{\mathrm{C}} = 0.8$ - 0.9 V.

These experiments reveal different results. First, the photoactivity of the attached C60 molecule is unambiguously demonstrated. The cathodic PC indicates an increase of the charge transfer after photoexcitation whereas the increase of the PL intensity indicates a reduction of the confinement for holes. The photoexcitation may alter the effective SBB. Since the intensity increase is observed before above band gap excitation, this charge transfer does not involve photo-generated carriers from the GaN NW electrode. In contrast, the modification of GaN NWs with triad molecules implies a different mechanism. A PC is observed only for sub-band gap excitation while the PL intensity does not change.

The PL spectra of GaN NW electrodes with (GaN/triad) and without triad modification (GaN/ox.) sustain these findings. The PL intensity at $U_{\mathrm{C}} = 0.35\,\mathrm{V}$ (0.3 V) and $U_{\mathrm{C}} = 0.7\,\mathrm{V}$ (0.8 V) with pH = 7 was measured. The results are shown in figure 3.36.

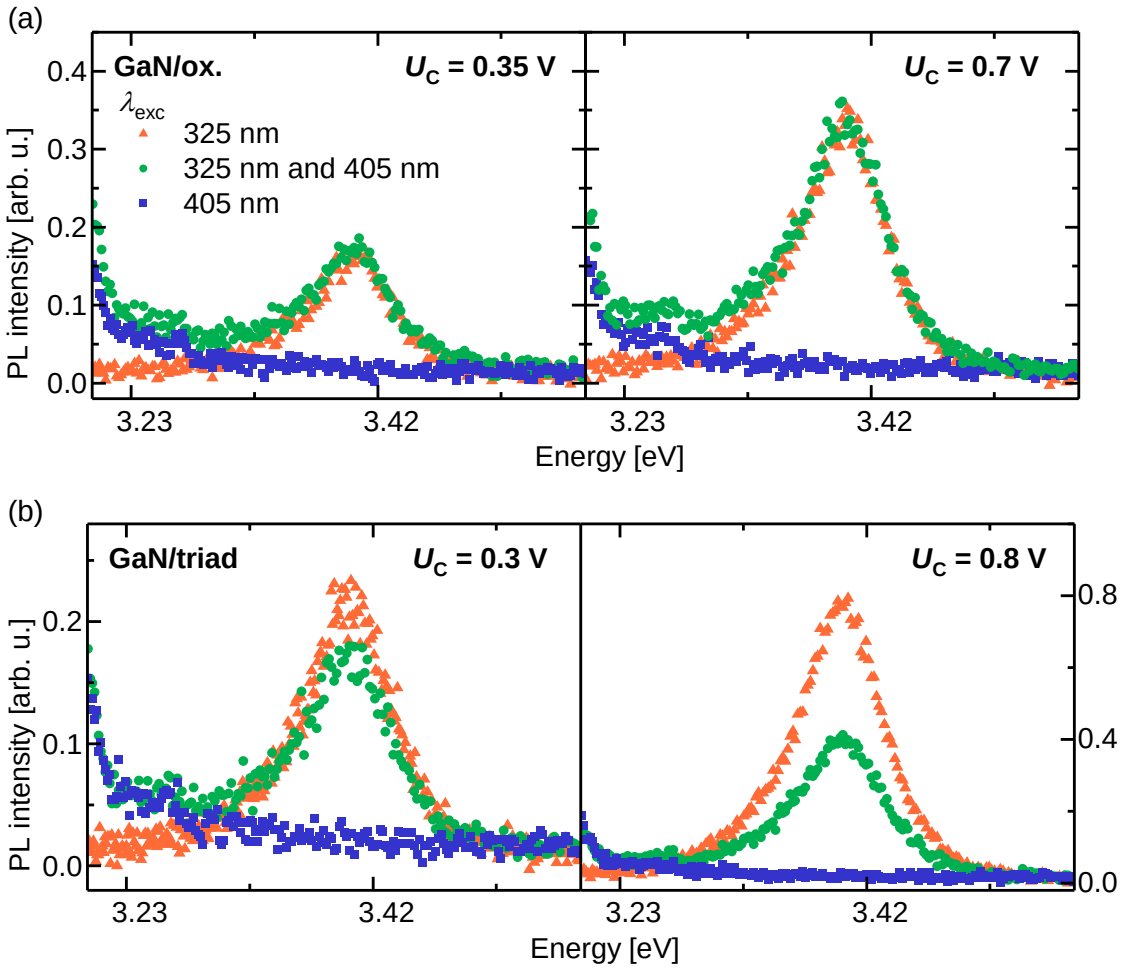

Figure 3.36: (a) PL intensities of GaN/ox. at $U_C = 0.35\,V$ and $U_C = 0.7\,V$ in dependence of the excitation wavelengths. The excitation with the second source does not alter the PL spectra. (b) PL intensities of GaN/triad at $U_C = 0.3\,V$ and $U_C = 0.8\,V$ in dependence of the excitation wavelengths. The excitation of the triad molecules results in a decrease of the GaN PL intensity.
The incident laser power ($\lambda_{exc} = 325\,nm$) was reduced to 0.5 % and the integration time was $t_{int} = 10\,s$.

The above band gap excitation ($\lambda_{exc} = 325\,nm$) of the GaN NW samples with and without surface modification causes the GaN near-band edge PL at $E_{gap}(GaN) = 3.41\,eV$. The PL intensity increases with increasing U_C. Additional excitation with $\lambda_{exc} = 405$ nm does not alter the peak position or shape of the GaN PL for the unmodified sample. In contrast, the PL intensity is quenched for the excitation of GaN NWs modified with triad.
This behavior can be assigned to photoexcitation and photoactivation of the triad molecules that results in the development of a surface dipole with a negative charge at the interface qualitatively similar to a pH increase and results in an increased SBB. As a consequence, the PL intensity is decreased due to the enhanced hole transfer into the electrolyte which is reflected by an increased photocurrent. The CLV measurements showed an increased PC at U_C for the triad modified GaN NWs compared to the NW electrodes with C60. In addition, a charge transfer between the triad molecules and the NWs was confirmed by IPCE measurements at cathodic bias.

The simultaneous PL and PC measurements were also performed with surface modified nitridated silicon to analyze the role of the working electrode. The intensity was integrated over the same energy range, but here, this is the luminescence of water (cf. section 2.1.1). The current density and the integrated PL intensity of triad modified silicon are shown in figure 3.37.

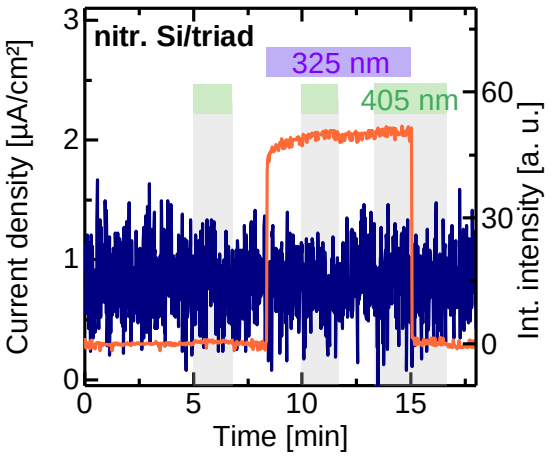

Figure 3.37: Current density and integrated intensity of GaN template modified with triad molecules at $U_C = 0.9\,V$ in dependence of λ_{exc}. Only a very low dark current is measurable. The intensity shows a very small increase for the excitation with $\lambda_{exc} = 405\,nm$. The incident laser power ($\lambda_{exc} = 325\,nm$) was reduced to 5 % and the integration time was $t_{int} = 1\,s$.

The current density is not altered by the photoexcitation with above or sub-band gap excitation. The luminescence intensity is slightly increased for $\lambda_{exc} = 405\,nm$. Since the luminescence intensity shows an opposite effect compared to GaN NWs electrodes, the findings strongly suggest a charge transfer between the triad molecules and the electrode across the GaN NWs due to an appropriate band alignment as the origin for the results shown above.

The open circuit potentials for dark conditions, for the excitation with $\lambda_{exc} = 405/325\,nm$ and the simultaneous use of $\lambda_{exc} = 405\,nm$ and $\lambda_{exc} = 325\,nm$ in reference to the RE were analyzed in view of the effective surface band bending. In table 3.4 the results are summarized as mean values and standard deviations of the different measurements.

Table 3.4: Calculated mean values for open circuit potentials (OCPs) with standard deviation for GaN/ox., GaN/APTES, GaN/C60 and GaN/triad for the different excitation wavelengths.

OCPs [U_C/mV]	dark	$\lambda_{exc} = 405\,nm$	$\lambda_{exc} = 325\,nm$	$\lambda_{exc} = 325\,nm$ & $\lambda_{exc} = 405\,nm$
GaN/ox.	37 ± 141	294 ± 83	504 ± 83	495 ± 94
GaN/APTES	67 ± 83	303 ± 21	495	479
GaN/C60	-46 ± 155	258 ± 40	455 ± 73	478 ± 40
GaN/triad	11 ± 84	269 ± 34	498 ± 57	469 ± 94

The sub-band gap excitation ($\lambda_{exc} = 405\,nm$) was demonstrated to excite C60 and the

triad molecules on the modified GaN NW electrodes. The OCPs of the different surface modifications during illumination are comparable. In general, there is a difference in the OCP values between OCP(dark) and OCP($\lambda_{exc} = 405\,nm$) independent from the surface modification. Even the OCPs of the GaN NW electrode without surface modification (GaN/ox.) increases. This finding suggests the involvement of surface states that shift the effective surface band bending. The OCPs for the excitation with $\lambda_{exc} = 325\,nm$ and with $\lambda_{exc} = 325\,nm$ and $\lambda_{exc} = 405\,nm$ do not vary. This shows that these latter surface states are not relevant for the effective SBB when excited with $\lambda_{exc} = 325\,nm$. The OCP enhancement of APTES for dark conditions and $\lambda_{exc} = 405\,nm$ compared to the other surface modifications is possibly caused by the reduction of the SBB due to the saturation of surface states.
The observed shifts of the OCPs for both the GaN/ox. and the GaN/triad samples demonstrate that the SBB is not altered by the surface modification and hence cannot explain the observations of PL and PC modulations.
From the values of the OCPs, the open circuit potentials after photoexcitation (OCP_{photo}) were calculated for sub-band and above band gap excitation ($\lambda_{exc} = 405\,nm$ and $\lambda_{exc} = 325\,nm$, respectively) in reference to the dark conditions. The values of OCP_{photo} in U_C are summarized in table 3.5 for the reference samples and the three surface modifications of the GaN NW electrodes.

Table 3.5: Calculated OCP_{photo} with standard deviation for GaN/ox., GaN/APTES, GaN/C60 and GaN/triad between the OCP in dark condition and the different excitation wavelengths.

OCP_{photo} [mV]	$\lambda_{exc} = 405\,nm$	$\lambda_{exc} = 325\,nm$
GaN/ox.	257 ± 61	405 ± 46
GaN/APTES	237 ± 62	370
GaN/C60	304 ± 139	498 ± 146
GaN/triad	257 ± 52	455 ± 32

OCP_{photo} of all surface modifications of GaN NW electrodes for $\lambda_{exc} = 405\,nm$ are comparable. In contrast, the above band gap excitation ($\lambda_{exc} = 325\,nm$) results in higher OCP_{photo} of GaN/triad and GaN/C60 samples compared to the reference samples. Usually, an increase in OCP_{photo} results in an increase of the photocurrent. As the potentials are similar for the excitation with $\lambda_{exc} = 405\,nm$ for all sample modifications, the changes of photocurrent density or PL intensity cannot be ascribed to the change of the surface modification. The value of OCP_{photo} for this excitation is an evidence that surfaces states are present in the surface of the working electrode. This coincides with the results for the OCP values. Since the photocurrent was not found to increase for the above band gap excitation (cf. figure 3.35), the small increases due to the OCP_{photo} are suppressed by more prominent effects such as the charge transfers and do not affect the photocurrent generation.

The charge transfer processes between the GaN nanowires and the triad molecule is elaborated. In figure 3.38 the reaction steps are displayed in detail.

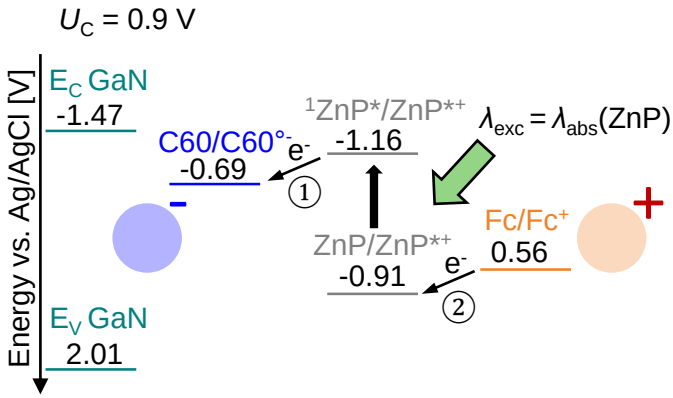

Figure 3.38: Reaction mechanism of PC generation and PL modulation of the GaN NWs and the molecular units of fullerene-ZnP-ferrocene triad molecules with the respective band energies and redox levels in units of the electrochemical scale [V].
E_C is the conduction band energy, E_V is the valence band energy, and E_{redox} is the energy level of the redox couple. The values of the semiconductor band edge potentials are according to refs. [50, 52].

First, the ZnP unit is photoexcited which results in the electron transfer from the ZnP to the C60 molecule. The excited state of ZnP is released by the electron transfer from the ferrocene to the ZnP. The charge transfer within the photo-activated triad molecule results in a dipole-like charging of the triad molecule. The negative charge of the dipole is located at the interface and thus, causing an increase of the SBB. This allows for an enhanced charge transfer between photo-generated carriers from the NW and the electrolyte and increases the photocurrent and concurrently decreases the PL intensity.

3.3.5 Summary and Conclusion

GaN nanowire electrodes with charge separation fullerene-Zn porphyrin-ferrocene triad molecules covalently linked to the nanowire surface are well-suited as a photoresponsive hybrid structure. The electrical and optical readout of these sensor electrodes allows for detailed investigation of charge transfer processes by simultaneously measuring the photocurrent generation and the modulation of the GaN photoluminescence intensity caused by the photo-excited triad molecules. In contrast to other electrode materials such as gold or ITO which are commonly used up to now, the capability of externally adjusting the surface band bending in the NW electrode, and thus, the working point, allows the operation in a broad bias range with high sensitivity in acidic and neutral aqueous environments. Thus, the charge transfer characteristics of the molecules and the GaN electrodes can be analyzed in well-defined conditions.
The absorption spectra of the triad molecules on the GaN NWs are a superposition of the single components on the electrode which means that there is no electronic interaction. The alignment of the absorption spectrum with the spectrum of the IPCE (incident photon-to-electron conversion) measurements of GaN NWs with triad molecules from $\lambda = 380$ - 800 nm indicates that the porphyrin units are the prominent photoactive

species which are responsible for the photocurrent generation at anodic and cathodic bias potentials. The IPCE measurements show an increased efficiency at cathodic potentials. An anodic photocurrent for photoexcitation with $\lambda_{exc} = 429\,nm$ was found for the reference sample and for the samples modified with triad and C60 where the photocurrent was unambiguously increased for the triad modified sample. A cathodic photocurrent was found to increase with U_C for the GaN NW electrodes with C60 and the triad molecules. The PC generated by the fullerene probably involves a direct charge transfer from the molecule in the electrode. This may promote the PC observed for the photoexcitation of the triad molecule. Nevertheless, the PC of the triad molecule is much larger than that of the fullerene which can possibly be explained by another mechanism which is the formation of dipoles at the surface.

Simultaneous current and PL measurements in an electrolyte solution at $pH = 7$ at cathodic potentials were analyzed with regard to the role of the functional group linked to the GaN nanowire surfaces. The GaN NW electrodes were excited with UV light and within the measurement procedure an additional photoexcitation with the use of a laserdiode was implemented that has an excitation wavelength in the same range of the absorption maximum of the ZnP unit ($\lambda_{exc} = 405\,nm$). This analysis allowed to determine the contribution of the different units to the total signal magnitude. Here, a distinct behavior of the different functionalization steps was observed. The oxidized GaN NW electrodes served as reference and no photocurrent nor a systematic PL signal change could be observed. In contrast, the analysis of the GaN NW electrode with fullerene showed a cathodic photocurrent for the excitation with $\lambda_{exc} = 405\,nm$. No photocurrent was observed for photoexcitation with UV light. The GaN PL intensity as well as the intensity before above band gap excitation increased for photoexcitation with $\lambda_{exc} = 405\,nm$ by the same magnitude. In addition, the GaN NW electrodes modified with triad molecules showed a cathodic photocurrent for the excitation with $\lambda_{exc} = 405\,nm$. Again, no photocurrent was observed for the photoexcitation with UV light. By the photoexcitation with laser light using a wavelength in the same range of the absorption maximum of the ZnP unit, the PL intensity of the GaN electrode was modulated. In contrast to the intensity increase that was observed for the fullerene, here a distinct decrease of the GaN PL intensity was monitored. The increase was only found for the simultaneous excitation of the GaN NW PL with UV light. The shape of the GaN PL spectra and the energetic position remained. The photoexcitation of the ZnP results in the electron transfer from the ZnP to the C60 molecule. The excited state of ZnP is released by the electron transfer from the ferrocene to the ZnP. The charge transfer within the photo-activated triad molecule results in a dipole-like state with a negative charge located at the interface. The negative surface charge increases the SBB and enhances the charge transfer between photo-generated carriers from the NW and the electrolyte. Thus, the photocurrent increases whereas the PL decreases. Next to the charge transfer between the electrode and the electrolyte solution, the results showed that the presence of surface states is relevant for the performance of the electrode.

The use of GaN nanowire electrodes with immobilized charge separation molecules allows

for a detailed study of charge transfer mechanims that could possibly be transferred to biological systems such as lipid bilayers or biomembranes. In ref. [135], it was shown that neuronal firing could be optically controlled by photo-induced electron transfer in triad molecules. In doing so, the elaborated patch-clamp technique was used. In contrast, GaN NW electrodes provide simplicity in the readout. Furthermore, they enable an electrical detection with a supplemental optical sensing mechanism by the GaN PL. The novel photoactive electrode can help to improve the understanding of many research areas in the biological field such as the monitoring of neural activity [154] or the artificial enzyme catalysis [155].

Chapter 4

InGaN/GaN NWH Arrays as Optochemical Electrodes for Imaging with Biochemical Contrast

The development of semiconductor electrodes as signal transducers for the detection of biochemical processes has improved. However, there is still the need of an electrode material that does not only detect, but enables spatially resolved imaging of these processes with simultaneous quantification since this of great interest for biological and medical research [1–3].

For this technique, it is essential that both optical excitation and detection of the response can be provided by the use of a standard optical microscope system. As a consequence, this approach offers a simple infrastructure, but demands an electrode material that is stable under physiological conditions and possesses a sufficient response at room temperature. In this way, the superposition of the chemical contrast with the optical images obtained by the microscope is possible and thus, providing supplemental functionality. This is in contrast to present sensor arrays that are based on solution-gated field-effect transistors. Solution-gated field-effect transistors based on silicon dioxide were designed that achieved spatial and temporal resolution [9]. However, the silicon dioxide surfaces suffer from photo-generated carriers which is why these sensor systems are incompatible with optical microscope technologies. Currently published research demonstrated the possibility to use transistors as sensing platform for local pH changes that have been caused by the activity of certain ion channels [156]. However, their biosensing application is limited to the detection. The visualization and localization of the changes within one sample are impossible. Since the concurrent high luminescence efficiency and spatial resolution requires the reduction of the minority carrier life time, only nano-structured electrode material systems are suited for this (bio-)imaging application.

Nanostructures hold a large surface-to-volume ratio that improves the detection of surface-related processes. Fluorescent nanoparticles (NPs) such as gold particles or semiconducting quantum dots (QDs) attracted attention as optical semiconducting transducer material [157, 158]. Semiconducting NPs are prominent due to their stable luminescence

intensity which is tunable by adjusting the particle size [159]. As the detection mechanism of semiconductor quantum dots is based on luminescence/fluorescence, the detection and monitoring of biological processes was realized [158, 160, 161]. The applications also included recording of the motion of the cytoplasm [160]. Furthermore, the surface of the NPs allows of modification to enhance water solubility [162,163], achieve functionalization for cell labelling [164] or improve the stability under physiological conditions [162, 165]. Quantum dots can be used for in vitro studies and intracellular pH sensing [166]. Furthermore, the fluorescence resonant energy transfer to molecules specifically binding to the functionalized NP surface could be observed in an optical microscope due to the change of the fluorescence intensity [167].

The use of NPs for the imaging of neuronal activity is under discussion [168], but a successful experimental realization is affected due to low signal-to-noise ratios (SNRs) [169, 170]. However, the most significant drawback of the NPs is that these particles to not allow the definition of an electrochemical working point in reference to the surrounding electrolyte solution. As a consequence, the direct relation and quantification of localized pH changes to changes in the surface potential is not possible. Furthermore, the toxicity of the CdSe/ZnS NPs [171], as the most commonly used NPs, are not yet clarified which negatively affects in vivo applications.

InGaN/GaN nanowire heterostructures (NWHs) are grown via molecular beam epitaxy which is a controlled growth process on a silicon substrate. As a result, the nanowires possess a high degree of crystallinity and only a low density of structural defects. Due to their excellent optical and electrochemical properties, these NWHs are predestined for pH detection [12] and biochemical sensing [22].

InGaN/GaN NWH arrays demonstrate a stable room temperature photoluminescence (PL) intensity that can be modulated by altering the lateral surface band bending. This modulation can be realized by external bias application or the generation of surface charges due to the modification of the pH of the electrolyte solution for instance [12]. On that account, each single nanowire individually probes the changes in the surface potential and thus, the chemical properties of the nanoscopic environment. With the electrolyte solution forming the front side contact, silicon as conductive substrate allows the application of an external bias voltage. Thus, the InGaN/GaN NWH electrode can be operated at a well-defined electrochemical potential. As a result, the sensitivity and stability can be optimized. By the use of InGaN/GaN nanowire heterostructures, the excitation with a light source with wavelengths in the visible range allows the investigation of cells and biological tissues. As they allow for an adjustment of the In content, a maximal yield of the emitted PL intensity can be achieved. A detailed description of the InGaN/GaN NWH arrays and the fundamental mechanisms and properties are presented in chapter 2.

Group III-nitride materials were demonstrated to be an ideal material system for biochemical applications since they possess a high electrochemical stability [13–15], are non-toxic for living cells [15], and feature a high pH sensitivity of about 55 mV/pH [15–17]. The GaN surface allows the chemical functionalization by covalent immobilization of biomolecules [16,18,19] and also the application as biosensor by using ion-sensitive field-effect transistors

that were modified with enzymes, such as penicillinase-modified AlGaN/GaN field-effect transistors [20] and acetylcholinesterase-modified AlGaN/GaN solution-gate field-effect transistors [21], has already been demonstrated.
In the proceeding paragraphs it is demonstrated that InGaN/GaN NWH probes allow the realization of optochemical electrodes (OCEs) with spatially resolved and quantitative analysis of local pH variations caused by cellular processes. In this setup, the InGaN/GaN NWHs are employed as electrode material in combination with a standard fluorescence microscope, enabling imaging of bias and pH changes. These changes are investigated by recording fluorescence images as function of the bias, pH or time. The bias and pH resolution limits are studied and the signal-to-noise ratios are assessed.
On the basis of these findings, local detection and imaging of biochemical activity of cells were realized with isolated intestinal crypts from Wistar rats serving as model system. For that purpose, these cells were deposited onto the nanowire surface and the activity of the sodium/proton exchanger (NHE), an ion transport channel that can externally be stimulated, was investigated. These experiments yielded that the NHE activity is reduced by indirect deactivation and blocking with specific binding inhibitors and the effect of direct activation via NH_3 uptake can be monitored. Additionally, the operation of the InGaN/GaN NWH arrays as OCEs allows the localization of the intensity changes which then could be attributed to the NHE activity.
In the following sections, the experimental fundamentals are presented. This includes the imaging setup, processing of the images and the preparation of commonly used nanoparticles and dyes (polycationic solution of poly(allylamine) hydrochloride conjugated with fluorescein, PAH-FITC and cadmium selenide quantum dots, CdSe QDs) that were compared with regard to time and pH stability. Then, the intestinal crypts of Wistar rats are described. The function and the transport mechanism are explained and the sodium/proton exchanger is discussed in more detail. In the following section, the results are presented and discussed. Finally, the findings are briefly summarized and specified with regard to prospective applications.
The basic characterization and the analysis of the InGaN/GaN NWH samples was started in collaboration with the research group of Prof. Wolfgang J. Parak at the Philipps-Universität, Marburg and the advanced studies including the experiments with biochemical imaging using isolated intestinal crypts were performed in collaboration with the research group of Prof. Martin Diener of the Institute for Veterinary Physiology and Biochemistry, Justus Liebig University, Giessen.
This research was supported by the contributions of Dr. Mikhail V. Zyuzin and Dr. Jens Wallys. The work presented in this chapter is published in ref. [172].

4.1 Experimental

In the following section, the imaging setups, the biochemical imaging and the preparation of nanoparticles are presented.

4.1.1 Imaging Setups

The NW samples were characterized and investigated using a three-electrode setup to allow photoelectrochemical analysis. The NW array that was deposited on a conductive silicon (Si) substrate was used as working electrode (WE) with Al/Ag back side contacts (cf. section 2.2.1), a small platinum tube was the counter electrode (CE) together with a Ag/AgCl (3 M KCl) reference electrode (RE). The setup is similar to that setup described in section 2.2.1 with the difference that the experimental measurement chamber used for the biochemical imaging experiments allows the immersion of microscope objective lenses. This measurement system does not involve a closed cyclic perfusing system. Here, the electrolyte solution is exchanged by stopping the pump for changing the buffer solution, then the solution runs over the sample and removes the residues of the earlier solution. It is not reutilized, but removed afterwards. The electrolyte solution perfusion allowed establishing well-defined conditions. The speeds of the peristaltic pump in the experiments were $v_{\mathrm{pump}} = 4.84\,\mathrm{ml/min}$ and $v_{\mathrm{pump}} = 6\,\mathrm{ml/min}$. The externally applied bias potentials versus the Ag/AgCl reference electrode are given as cathodic bias voltages and are denoted as U_{C}.
In figure 4.1 a technical drawing and a photograph of the measurement chamber for fluorescence imaging experiments is shown.

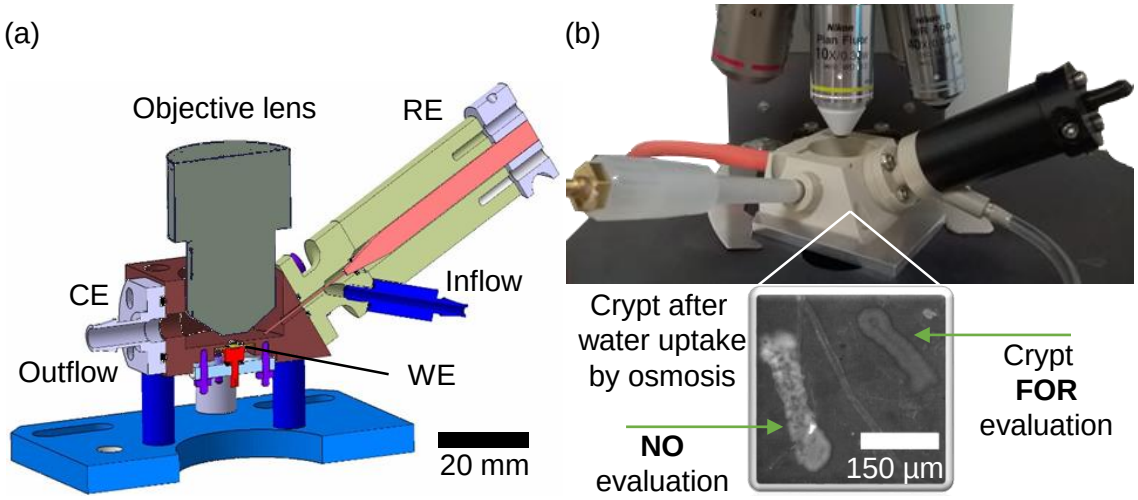

Figure 4.1: (a) Technical drawing and (b) photograph of the measurement chamber for fluorescence imaging experiments. The fluorescence image in (b) shows a zoom of the sensor surface with two isolated intestinal crypts. The fluorescence image was recorded with a tenfold lens, an integration time of $t_{\mathrm{int}} = 250\,\mathrm{ms}$ and at $U_{\mathrm{C}} = 150\,\mathrm{mV}$.

The technical drawing of the measurement cell shows the immersed objective lens, the platinum tube, the RE and the adapters for inflow and outflow of the electrolyte solution. In figure 4.1(b) the fluorescence image shows two isolated intestinal crypts. The crypt on the left is bloated due to water uptake by osmosis which inhibits the proper function of the NHE activity. Hence, these cells were excluded from fluorescence studies. In contrast, it is assumed that isolated crypts such as the one on the right exhibit proper activity. This sort of crypt cell was further investigated by fluorescence analysis.

As electrolyte solution, a 10 mM phosphate-buffered salt (PBS) solution with a sodium chloride (NaCl) concentration of $c_{\mathrm{NaCl}} = 137$ mM and a potassium chloride (KCl) concentration of $c_{\mathrm{KCl}} = 2.7$ mM was used (cf. appendix B.1). Modified Tyrode´s solution of pH = 7.4 was used for biochemical experiments (cf. appendix B.3). This electrolyte solution enables the imitation of the physiological surrounding of living tissues and cells. All experiments were performed at room temperature. The fluorescence images were recorded using two different incident light fluorescence microscopes. In the following, the instruments and settings are explained and related to the respective experimental setup.

1. **Carl Zeiss, Axiotech with electronic control gear FluoArc, AxioCam**
   A mercury vapor lamp was used for excitation where the wavelength was filtered to $\lambda_{\mathrm{exc}} = 530$ - 585 nm and the detection wavelength was $\lambda_{\mathrm{det}} = 615$ nm. The incident light was focused on the sample surface using W Plan-Apochromat 63x/1.0 M27 and W Plan-Apochromat 10x/0.5 M27 75 mm objective lenses. These objective lenses allowed for immersion into the aqueous solution and provided sufficient working distances.

2. **Eclipse 80i microscope, Nikon, s/w camera digital slight DS 2 M BWc, Nikon**
   A mercury vapor lamp was used for excitation and the excitation wavelength was filtered using the FITC filter set to $\lambda_{\mathrm{exc}} = 465$ - 495 nm with a detection wavelength of $\lambda_{\mathrm{det}} = 515$ - 555 nm. The indicident light was focused on the NW surface using a Nikon Plan Fluor 10x/0.30 W or a Nikon Plan Fluor 40x/0.80 W objective lens. These objective lenses allowed for immersion into the aqueous solution and provided sufficient working distances with $WD = 3.5$ mm and $WD = 2$ mm.

4.1.2 Biochemical Imaging - Processing

The fluorescence images were analyzed using the "ZEN 2009" software (Carl Zeiss AG, Oberkochen, Germany). The setting was the same for all measurements. The images were evaluated by integration of the intensity in the whole area. The integrated intensity which is plotted as a function of time, pH and U_{C} represents the sum of the fluorescence intensities of all pixels divided by the pixel number (mean intensity).
The experiments with cells required the following preparation. After the isolation procedure of the intestinal crypts (details cf. appendix D), a small volume ($V = 2$ - 3 ml) of the concentrated solution was pipetted on a petri-dish ($d = 35$ mm). Then, with the aid of a transmission-light microscope, individual crypts were collected to obtain a stock solution. A volume of $V \approx 20\,\mu$L of the stock solution with individual crypts was deposited on the dry electrode surface for a period of $t \geq 15$ min, necessary to allow the crypts to adhere on the surface and to come close to the nanowire surface. After incubation the modified Tyrode´s solution perfusion over the NWH arrays was started, which enabled the removal of unbound crypts and replaced the residual stock solution. The pump was only

stopped for the exchange of the buffer solution to another solution with different pH or composition. A continuous circulation of the electrolyte solution was not applied and the previous solution was collected separately. The objective lenses were carefully immersed into the electrolyte solution and focused on the nanowire surface. Before recording of the fluorescence images, a test procedure that assured the proper function of the cell and the setup was performed. It was realized by checking the change of the nanowire fluorescence intensity with the modulation of the surface potential by bias application. Provided that the test was positive, the fluorescence images were recorded every 30 s.
The chemical contrast illustrates the fluorescence intensity increase and decrease. The images that were used for these calculations are the raw images (numbers 1, 2, 3) of the transient measurement shown in figure 4.16(b). For this purpose, the raw fluorescence images were converted into grayscale images. To obtain the image representing the increase of the fluorescence intensity, the differences between the images with amiloride or NH_4Cl and the image recorded in the presence of the modified Tyrode´s solution without additives were calculated (difference of images 2 or 3 and the reference image 1). In contrast to the calculation of the increase of the intensity, the intensity decrease is obtained from the difference of the reference image 1 and image 2 or 3. For making the changes more clear only the brightness values of the resulting difference images were modified. To adjust the brightness, the tonal values of the images were multiplied with an appropriate factor of 1/38. Since the same factor was used for multiplication of all images, the information is not altered. Following this procedure, the images representing the intensity increase (decrease) are displayed in red (blue). These colored images were superimposed to allow the spatially resolved identification of the pH-induced changes.
Besides the calculation of the chemical contrast, the fluorescence intensities in the biochemical experiments were integrated and determined as mean value of the analyzed area. Nevertheless, the area was individually determined for each image to take the crypt motion into account. For this purpose an image mask was created that defined the outline of the crypt. The mask generation was as follows: the images were blurred, then the processed images were binarized and finally filtered by a morphological opening. The denotation "with crypt" (w crypt) represents the consideration of the nanowire optoelectrode´s area which is defined by the mask with the outline of the cell as a border. The denotation "without crypt" (w/o crypt) represents the area of the inverted mask and shows the results of the nanowire OCE alone. The integrated intensities were divided by the calculated area to allow a clear signal attribution towards changes of the pH and to avoid area-dependent shifts.

4.1.3 Nanoparticle Preparation on Silicon Substrate

Fluorescent nanoparticles such as quantum dots or dyes are commonly used as optical transducers which change their absorption or fluorescence properties on detection. For the comparison of the stability of InGaN/GaN NWH arrays as optochemical electrodes with such state of the art optical transducer materials, silicon substrates were coated with

CdSe quantum dots (QDs) and polycationic solution of poly(allylamine) hydrochloride conjugated with fluorescein (PAH-FITC) [1].
The synthesis of CdSe QDs followed previously described preparation protocols [163, 173]. For deposition of the nanoparticles on the silicon substrate, the spin coating technique was used with a volume of $V = 20\,\mu$L of CdSe QDs and PAH-FITC solutions ($t = 15$ min incubation time for polycationionic solution) at a speed of $v = 6000$ rpm for $t = 1$ min. The CdSe concentration was $c_{\mathrm{CdSe}} = 15.45\,\mu$M (toluene) and the PAH-FITC concentration was $c_{\text{PAH-FITC}} = 2$ mg/ml (pH = 6.5).
For the preparation of the proctection layers, the layer-by-layer assembly technique [174] with two bilayers of polyanionic poly(sodium-4-styrene sulfonate) (PSS) and polycationic poly(allylamine) hydrochloride bilayers ($V = 20\,\mu$L, $c = 2$ mg/ml, pH = 6.5) was applied with PAH forming the final layer. In this process the solutions were spin-coated for $t = 1$ min after $t = 15$ min of incubation each [132]. The nanoparticle structures are denoted as Si/QDs/$(\mathrm{PSS/PAH})_2$ and Si/PAH-FITC/$(\mathrm{PSS/PAH})_2$ where the number "2" indicates the total number of deposited polyelectrolyte bilayers.

4.2 Colon and Intestinal Crypts from Wistar Rats

In the following section specific parts of the rat colon are briefly described. The structure is presented and the various functions and transport mechanisms that are important for the biochemical imaging study are illustrated. Furthermore, the transport via the sodium/proton exchanger (NHE) is explained and its activity and the correlation with the oxidative phosphorylation (OXPHOS) is explained. The NHE inhibition is described and the effect of the indirect deactivation of the NHE with 2,4-Dinitrophenol (DNP) solution is presented. Finally, the different types of NHE channels are introduced and correlated with the presented investigations.

4.2.1 Functional Design and Structure

The colon (*intestinum crassum*) denotes the intermediate and also largest part of the large intestine of mammals. From the macroscopic level, the large intestine can be divided into three [175] or rather five [176] segments: the cecum, the proximal colon (*colon ascendens*), the big colon flexur (*colon transversum*), the distal colon (*colon descendens*) (and the rectum).
As the last stage in the digestive system, the large intestine has one major function: it is responsible for the transport of digested food and in this process, the colon resorbs water, bacterially segregates carbohydrates and stores the residual undigested material as faeces. The large intestine of human is able to resorb a volume of $V = 1.3$ - 1.8 l of electrolytic solution per day and has a resorption capacity of a volume of $V = 5$ - 6 l/day. With the

[1] The surface modification of the Si substrates with fluorescent dye and QDs were prepared by Nadeem Sabir, a former member of the working group of Prof. Wolfgang Parak (Philipps University of Marburg, Marburg, Germany).

daily electrolyte solution uptake, more than 90 % of the water from the proximal colon is resorbed [177].
The main processing of the different functions is ensured by the intestinal wall. The structure of the intestine wall with the main layers (details cf. [178]) is schematically depicted in figure 4.2.

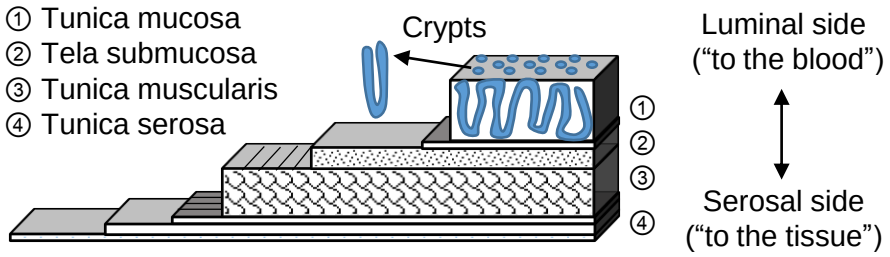

Figure 4.2: Schematic presentation of the colon wall structure according to ref. [178].

From the luminal outwards to the serosal inwards, the first layer is the *tunica mucosa*, then the *tela submucosa* and the *tunica muscularis* follow and finally, the *tunica serosa* forms the final layer. The *tunica serosa* (**4**, figure 4.2) as outermost layer is comprised of squamous epithelium and connected with the *tunica muscularis* via soft tissues [179]. The *tunica muscularis* (**3**, figure 4.2) consists of two layers. One of these layers has cell lines that are longitudinally aligned to the intestinal axis and the other layer, which is the inner layer, has a circular alignment to the intestinal axis. These layers are called *stratum longitudinal* and *stratum circular*. The *tela submucosa* (**2**, figure 4.2) is composed of elastic fibres and locates blood and lymph vessels [180]. The *tunica mucosa* (**1**, figure 4.2) is comprised of three parts: the *lamina epithelialis*, the *lamina propria* and the *lamina muscularis*. The intestinal crypts are found in the *lamina epithelialis*.
The *tunica mucosa* has a smooth surface, but deep invaginations with a high density, the *glandulae intestinales* which are also called Lieberkühn crypts [181], that increase the surface area by a factor of ~ 30 [176]. The *lamina propria* mainly consists of enterocytes that are responsible for the increase of the surface area. The cell nucleus of enterocytes is located in the lower third of the cell [176]. On the surface, enterocytes possess movable microvilli [176]. These micrivilli are also located on the whole surface of the colon. Next to this cell type, goblet cells are found in that layer which are responsible for the segregation and transport of ingesta and to protect the surface [181]. In addition, there are enteroendocrine cells located in that layer that segrete hormons such as serotonin [182].
The epithelial layer of the intestine is subject to a constant cell renewal. The epithelial cells of rats regenerate every two to three days [183]. The structure of epithelial cells is shown in figure 4.3.

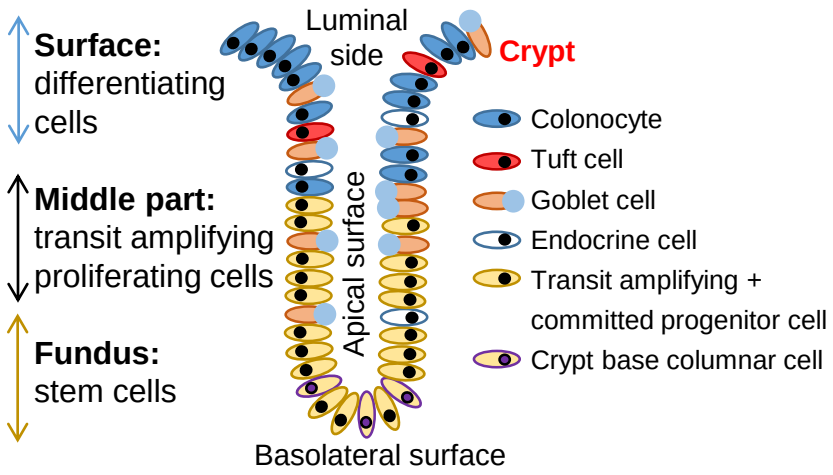

Figure 4.3: Schematic presentation of the large intestine/colon with crypt structure and the various cell types of the large intestine according to [184].

Undifferentiated cells migrate from the base of the crypts (fundus) over the middle part to the surface where they are shed off into the intestinal lumen and undergo apoptosis [185,186]. During the migration these epithelial cells differentiate and develop their specific functionality. Depending on the degree of maturity, the intestinal epithelial cells are divided into the segments: fundus, middle and surface (cf. figure 4.3). The expression of the transporters which exchange ions and establish a chemical equilibrium between the basolateral and apical part of the cell depends on the stage of the cell renewal process.

4.2.2 Functions and Transport Mechanisms in the Intenstinal Epithelium

The intestinal epithelial cells form a barrier and seperate the ingesta from the mucosal surface of the body. The cells regulate the intracellular and extracellular environment by establishing a chemical equilibrium between resorbtion and secretion [177]. Resorption or secretion occur by certain semiochemicals such as neurotransmitters or hormons that trigger the exchange of ions by binding to corresponding receptors.
The resorption process includes the absorption of water, NaCl and short-chain fatty acids (SCFA), whereas the secretion includes KCl, bicarbonate and mucus [177].

Resorption

The resorption is the main task of the colon. Here, transepithelial paths are used to exchange the different components by ion exchange over various ion exchange channels. The resorption processes are summarized in figure 4.4.

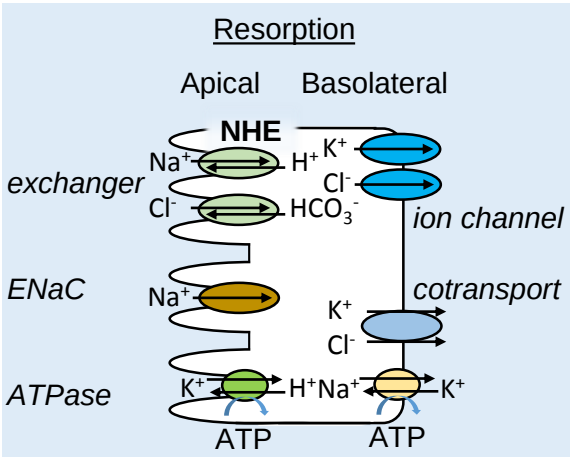

Figure 4.4: Schematic presentation of resorption processes in the colon.

The resorption and absorption mechanisms are different and depend on the particular species. However, the general mechanisms are qualitatively similar [187]. Here, the resorption process of rats is considered.
There are special transport channels and mechanisms for each ion. Some channels do only allow the transport of one ion species whereas others work via exchange or cotransport. A special transport protein is the ATPase (Adenosine triphosphate, ATP) which energizes further transport pathways by creating an ion-dependent chemical gradient. The resorption of Na^+ and Cl^- is an electroneutral transport [177]. The apical sodium/proton exchanger (Na^+/H^+-exchanger, NHE) runs parallel to the apical Cl^-/HCO_3^--exchanger which results in an uptake of Na^+ and Cl^- into the cell and a simultaneous release of H^+- and HCO_3^--ions from the cell into the intestinal lumen. With Na^+/K^+-ATPase the sodium ions and with Cl^--channels chloride ions are basolaterally secreted [177, 188]. K^+ is resorped via two different Na^+/K^+-ATPase membranes (the membranes are located in the surface- and also in the crypt epithelia). An electrogenic resorption per epithelial Na^+-channels (ENaC) is found only in the surface epithelium of the distal colon [177].

Secretion

Next to the resorption of ions, the secretion acts as the counter part to the resorption which facilitates the transport of the digested materials, such as the secretion of Cl^--ions as KCl and NaCl. The main secretion processes are summarized in figure 4.5.

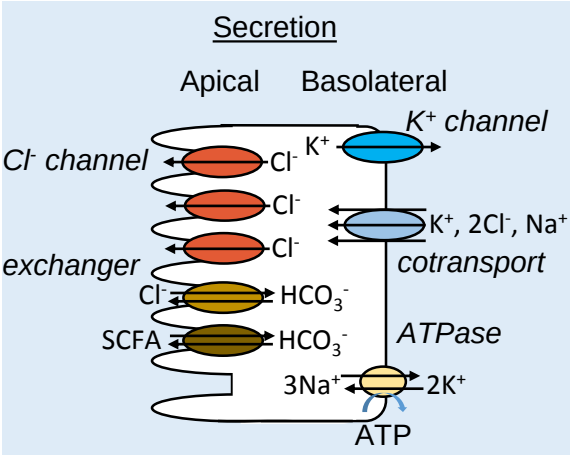

Figure 4.5: Schematic presentation of secretion processes in the colon.

The secretion is a sequence of single transport processes. The initially required energy for the secretion processes is provided from the basolateral Na^+/K^+-ATPase. Here, a disequilibrium is caused by the exchange of three Na^+-ions with two K^+-ions. This chemical gradient drives the $Na^+/K^+/2Cl^-$-cotransport with the result that the number of K^+- and Cl^--ions is increased [189]. The K^+-ions are secreted via K^+-channels and as a result a Cl^--gradient (high Cl^--concentration) is established. The Cl^--accumulation degrades by the release via apical Cl^--channels caused by the driving force of the negative membrane potential. Simultaneously, Na^+-ions secrete by paracellular transport to maintain the charge balance in the cell. HCO_3^--ion secretion occurs electrogenically by different channels. On the one hand, there are apical HCO_3^-/Cl^-- and $SCFA^-/HCO_3^-$-exchanger and also cystic fibrosis transmembrane conductance regulator-Cl^--channels (not shown in the schematic). The transport via HCO_3^-/Cl^--channel is parallel to the NHE as mentioned above. On the other hand, the HCO_3^--ion secretion can occur via apical Cl^--channels [190]. The secretion of ions results in a osmotic gradient and as a consequence, water is absorbed into the lumen to decrease this osmotic pressure [191].

Na^+/H^+-Exchanger

The sodium/proton exchanger (NHE) is an integral plasma membrane protein which mediates the electroneutral transport [192, 193] of sodium and hydrogen by stoichiometrical exchange of an extracellular Na^+-ion with an intracellular H^+-ion [192, 194]. Among others, this exchanger regulates the intracellular pH and the cell volume. Up to now nine different isoforms of NHEs are identified [195]. Only the isoforms NHE-2, NHE-3 and NHE-4 are expressed in the colon of rats [196]. The NHEs consist of 10 - 12 transmembrane segments which are enclosed by an N-terminal and a COOH-terminal that is integrated into the cytosol [195]. These segments contain the binding sites for ions and inhibitors. The different isoforms have a diverse occurance and all isoforms possess specific properties. The NHE isoforms of type NHEs-2 and NHEs-3 depend hyperbolically on the extracellular sodium concentration and NHE-4 shows a sigmoidal dependence [196]. The

affinity constants are 50.0 mM for NHE-2 and 4.7 mM for NHE-3 [196].
In general, the proper function of sodium/proton exchange is maintained by the Na^+/K^+-ATPase [194,197] where Na^+/K^+-pumps release three Na^+-ions with simultaneous uptake of two K^+-ions which causes a concentration gradient. To maintain the chemical balance, the NHE is activated and sodium ions are resorbed from the lumen. In parallel hydrogen is exchanged (cf. section 4.2.2; resorption/secretion). Since the transport is a gradient-dependent process, that does not directly depend on metabolic energy, it is termed a "secondary active transport" [198].
The NHE activity, that is the exchange rate of sodium/proton, dependening on an extracellular allosteric binding site, can be altered. A decrease of the intracellular pH was demonstrated to increase the NHE activity [196] whereas the pH alkanization is known to deactivate the NHE activity [199]. Independent from the isoform type, NHEs show a position-dependent activity. The undifferentiated cells near the crypt fundus show a low activity of Na^+/H^+-exchange and more differentiated cells from the middle part of the crypt to the surface demonstrate to have a higher NHE activity [199] (cf. figure 4.3(a)). Additionally, a reduction of the NHE activity was observed in processes that reduced the ATP production [200, 201]. This finding is attributed to a reduction of the sensitivity towards the intracellular proton concentration [197].
ATP (adenosine triphosphate) is used as energy carrier in cells that is produced during the oxidative phosphorylation and plays a major role for the NHE activity. The OXPHOS is a metabolic pathway that is based on an electron transport chain which involves various transmembrane movements of ions (chemiosmosis). In this process energy is stored which in return yields ATP in the final step.
The ATP reduction demonstrated to alter the NHE activity [200,201]. The ATP depletion can externally be established by the use of a proton transporter that acts as uncoupler of the oxidative phosphorylation such as 2,4-Dinitrophenol. The uncoupler 2,4-Dinitrophenol composes proton gradients and the energy stored for the ATP releases as thermal energy. Transport channels depending on ATP, such as the Na^+/K^+-ATPase, show reduced activity. Usually, Na^+/K^+-ATPase secretes three Na^+-ions simultaneously intaking two K^+-ions and this chemical gradient initiates the NHE activity. As a result of the ATP depletion, this concentration gradient is lacking Na^+-ions and as a consequence, the NHE activity is indirectly deactivated [202].
The NHE activity can also be reduced in another way. The sodium/proton exchanger is an amiloride-sensitive transport protein that can be inhibited by amiloride and its derivates. The inhibition of amiloride is ascribed to the occupation of Na^+-binding sites in the extracellular space since a high sodium ion concentration showed a reduced inhibitory potency of amiloride [196]. These binding sites are located in the transmembrane-spanning segments [197]. The inhibitory potencies of different NHE inhibitors in dependence of the isoforms are summarized in [196]. In table 4.1, the data of amiloride, that is used in the present experiments, are shown for the different NHE isoforms in rat colon.

Table 4.1: Inhibitory potency (K_i) of amiloride for different NHE types.

NHE-1	NHE-2	NHE-3	NHE-5
1-1.6 μM (from rat)	1.0 μM (from rabbit)	>100 μM (from rat)	21 μM

For the colon of the rat, only NHE-2 and NHE-3 are sensitive to amiloride and the activity allows for inhibition. The inhibitory potency for NHE-2 is a much higher than for NHE-3 (more than a hundred times) assuming that extracellular pH changes can be assigned to the inhibition of NHE isoforms of type NHE-2.
Next to the binding mechanism, the reduction of physiological pH to approximately pH ≈ 6 can result in a reduction of the amiloirde inhibition as well [196].

4.3 Results and Discussion

In the following section, InGaN/GaN NWH arrays are investigated as optochemical electrodes (OCEs) with the use of an incident light fluorescence microscope. The bias and pH dependences of the NW PL intensity are investigated and the resolution limits are studied. The performance of the NWHs is compared to two other standard methods that are usually used for the optical detection of pH changes in the biomolecular environment. Furthermore, the signal-to-noise ratios as function of the cathodic bias voltage and the time resolution of the InGaN/GaN NWH electrodes are investigated. Finally, the NWH electrodes are studied as OCEs for the detection of extracellular pH in dependence of the activity of isolated intestinal crypts from Wistar rats. These cells represent a first model system for imaging studies. The pH change is quantified and compared to the findings obtained by intracellular pH measurements in literature.

4.3.1 Basic Characterization - Long-term and pH Stability

The InGaN/GaN NWH arrays used in the basic characterization/bioimaging experiments ("1."/"2.", cf. section 4.1.1) are $l = (307 \pm 29)$ nm (bioimaging: $l = (640 \pm 18)$ nm) in length and $d = (56 \pm 13)$ nm (bioimaging: $d = (45 \pm 11)$ nm) in diameter. Details on the sample structure and the preparation are presented in chapter 2.1.2. The characteristic photoluminescence spectra of the two InGaN/GaN NWH array types in 10 mM PBS solution for pH $= 7$ at $U_C = 0.5$ V are shown in figure 4.6.

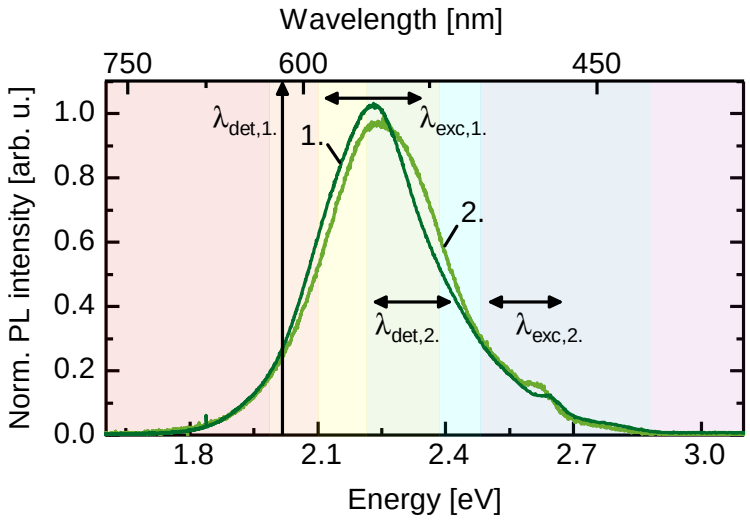

Figure 4.6: Normalized PL spectra of InGaN/GaN NWH array electrodes in 10 mM PBS solution for pH = 7 at $U_C = 0.5$ V at room temperature. The excitation and detection wavelength ranges of the two experimental setups as well as the InGaN/GaN NWH arrays are indicated with numbers "1." and "2." referring to section 4.1.1, respectively. InGaN/GaN NWHs were excited with a laserdiode of $\lambda_{exc} = 405$ nm.

The InGaN PL emission at room temperature ranges from $\lambda = 450$ - 700 nm ($E = 2.7$ eV - 1.8 eV) due to the inhomogeneous In distribution (cf. section 2.1.2) and sensitively depends on the lateral band profile which can be altered by the application of an external bias voltage or a change of the solution pH (details cf. section 2.2). Based on these unique properties of InGaN/GaN NWH arrays, the electrodes are investigated as OCEs for biochemical applications. Here, the customized electrochemical cell described in section 4.1.1 is used which allows the immersion of the different objective lenses into the electrolyte solution.

For the bioimaging applications, the stability of the sensor in aquaeous solutions is a basic prerequisite. Time- and pH-dependent fluorescence measurements were performed by recording fluorescent images of the NWH array samples with a standard optical microscope. These results were compared to the most frequently used pH sensitive sensors such as fluorescent probes and semiconductor quantum dots since these methods are commonly employed probes for biosensing applications [203–205]. The improved performance of QDs regarding their stability against photobleaching was recently reported [206].

The stability of the InGaN/GaN NWH arrays, poly(fluorescein isothiocyanate allylamine hydrochloride)-fluorescein isothiocyanate (PAH-FITC) and CdSe quantum dots were compared [2]. In figure 4.7, the fluorescence spectra of the investigated pH probes are shown.

[2]The surface modification of the Si substrates with fluorescent dye and QDs were prepared by Nadeem Sabir, a former member of the working group of Prof. Wolfgang Parak (Philipps University of Marburg, Marburg, Germany).

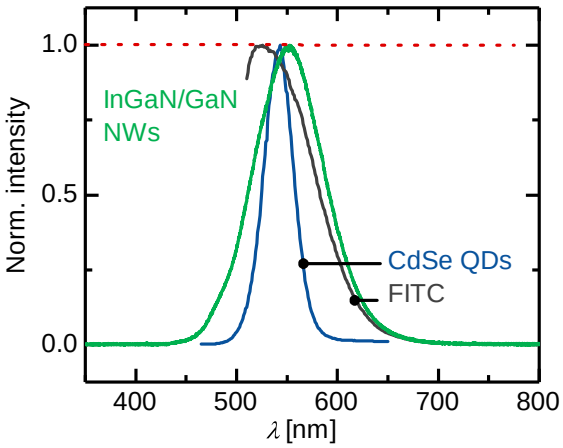

Figure 4.7: Normalized fluorescence/photoluminescence spectra of InGaN/GaN NWH (green line), CdSe QDs (blue line) and dye FITC (grey line) at room temperature. InGaN/GaN NWHs were excited with a laserdiode of $\lambda_{exc} = 405\,nm$ and measured with the setup presented in section 3.7. The fluorescence spectra were measured with a fluorometer using excitation wavelengths of $\lambda_{exc} = 520\,nm$ (CdSe QDs) and $\lambda_{exc} = 490\,nm$ (FITC). The spectra of InGaN/GaN NWHs were measured without electrolyte, and the spectra of the CdSe QDs and FITC in water (pH = 6.5). All spectra were measured at not biased conditions.

The spectra of InGaN/GaN NWHs, CdSe QDs and of the dye FITC show similar emission maxima at $\lambda_{em} = 523\,nm$ for FITC, $\lambda_{em} = 534\,nm$ for InGaN/GaN NWHs and $\lambda_{em} = 543\,nm$ for CdSe QDs.

For the stability analysis, the fluorescence intensities of the InGaN/GaN NWs, CdSe QDs and PAH-FITC were measured as a function of the time in 10 mM PBS at pH = 7 and under continuous excitation. Both CdSe QDs and PAH-FITC were immobilized on a natively oxidized silicon substrate as electrode support and then coated with two bilayers of poly(sodium 4-styrenesulfonate)/poly(allylamine hydrochloride) (PSS/PAH) that are applied for stabilization [132] according to the protocols described in section 4.1.3. In the following, the two protection bilayers are denoted as $(PSS/PAH)_2$. The fluorescence images were recorded every two minutes for a period of $t = 45$ minutes of continuous irradiation. The fluorescence image analysis is described in section 4.1.2. All intensities are normalized to the initial value for better comparison. The results are shown in figure 4.8.

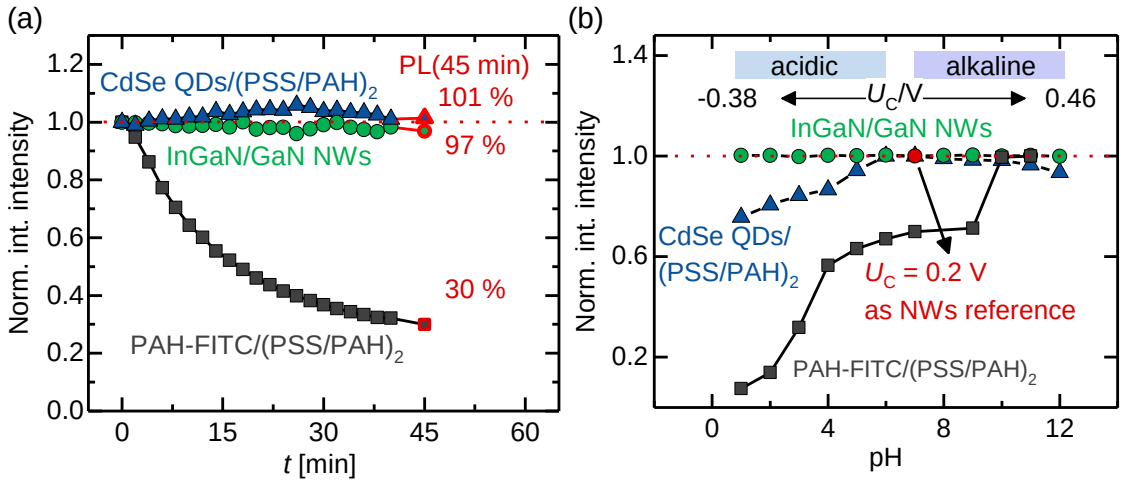

Figure 4.8: Time-dependent analysis of fluorescence images for InGaN/GaN NWHs in comparison with CdSe QDs and the fluorescent dye PAH-FITC. (a) Integrated fluorescence intensities as function of the time t of InGaN/GaN NWHs, CdSe QDs and PAH-FITC in buffer solution. The NWH electrode was biased to $U_C = 1\,V$ whereas the other probes were measured without external bias application. The intensities of the NWHs and the QDs are almost constant in the investigated period whereas the intensity of PAH-FITC decreased by 70 % of the initial value. (b) Fluorescence image analysis as a function of the pH. The pH stability of InGaN/GaN NWHs is compared to the pH stability of CdSe QDs and PAH-FITC. The bias was adjusted from $U_C = $-0.38 V to $U_C = 0.46\,V$ to the InGaN/GaN NWHs PL intensity at $U_C = 0.2\,V$ at pH = 7.

Both the InGaN/GaN NWHs and the CdSe QDs demonstrate a long-term stability of the PL intensity with a decrease of only $\Delta PL = $-3 % of the initial PL intensity value after $t = 45$ min. The intensity increase of CdSe QDs from approximately $t = 10$ - 40 min is noticeable. This effect has already been reported and is known as "photobrightening" [162]. In contrast, for PAH-FITC it becomes apparent that the dye is not stable in the investigated time interval with a decrease of $\Delta I = $-70 % of the initial fluorescence intensity.
The stability of InGaN/GaN NWHs, CdSe QDs and PAH-FITC was additionally investigated as a function of the pH (cf. figure 4.8(b)). The pH was varied between pH = 1 and pH = 12. To compensate the pH-induced changes of the PL intensity of the NWH electrodes, the bias voltage was simultaneously adjusted by a variation of the bias from $U_C = -0.38\,V$ to $U_C = 0.46\,V$. Thus, the PL intensity was kept at the same value as initially recorded for $U_C = 0.2$ V and pH = 7. Consequently, the surface band bending remained unmodified so that a degradation by oxidation processes was suppressed from alkaline to acidic pH. In contrast, the PL intensity of the CdSe QDs decreases in the acidic sequence with pH = 7 as starting point to pH = 1 by $\Delta PL = 24$ % and in the alkaline sequence with pH = 7 as starting point to pH = 12 by $\Delta PL = 7$ %. The instability in solutions other than neutral pH has been reported for CdSe QDs and their application is restricted to only a small pH range of $6 < pH < 8$ [91] and $6 < pH < 9$ [90]. Beyond these pH ranges, a corrosive process may start [90]. The fluorescence of PAH-FITC is stable in the alkaline pH range and slightly decreases with increasing pH (note that the intensities are normalized to the intensity at pH = 11). In contrast, PAH-FITC is not stable for neutral to acidic pH values. The intensity decreases with decreasing pH by $\Delta PL \approx 92$ % from pH = 11 to pH = 1.

The results from the stability studies show that InGaN/GaN NWH arrays demonstrate a time stability with only three percent decrease of the PL intensity after 45 minutes. Due to the possibility to adjust the bias voltage, the electrodes are stable from strong acidic to alkaline pH. In comparison, the most frequently used approaches for optical pH sensing such as CdSe QDs and FITC possess only small operable pH ranges. The limitation of the measurable pH ranges of these probes can only be extended by surface functionalization or the deposition of protective layers [206].

4.3.2 Analysis of InGaN/GaN NWHs as OCEs - Bias, pH and Time Resolution and Investigation of the Signal-to-Noise Ratio

InGaN/GaN NWH ensembles operated as OCEs were investigated with respect to the application as a biosensor. These are the detection and the localization of pH and bias changes that are caused and accompanied by molecular cell processes. The intensities of the recorded fluorescence images were integrated so that the results equal a mean intensity of an area of $A \approx 15{,}000\,\mu\text{m}^2$. The area is calculated for a NW density of $\rho_{\text{NW}} = 180\,\text{NWs}/\mu\text{m}^2$ which is equivalent to an excitation of $2.7\,\text{x}\,10^6$ NWs.
For the pH- and bias-dependent analysis, the integrated fluorescence intensities were studied as a function of both the pH and the bias voltage. The pH was varied between $\text{pH} = 2$ and $\text{pH} = 10$ in steps of $\Delta\text{pH} = 1$ and the bias voltage was altered from $U_{\text{C}} = 0\,\text{V}$ to $U_{\text{C}} = 1.2\,\text{V}$ in in steps of $\Delta U_{\text{C}} = 100\,\text{mV}$. The results are shown in figure 4.9.

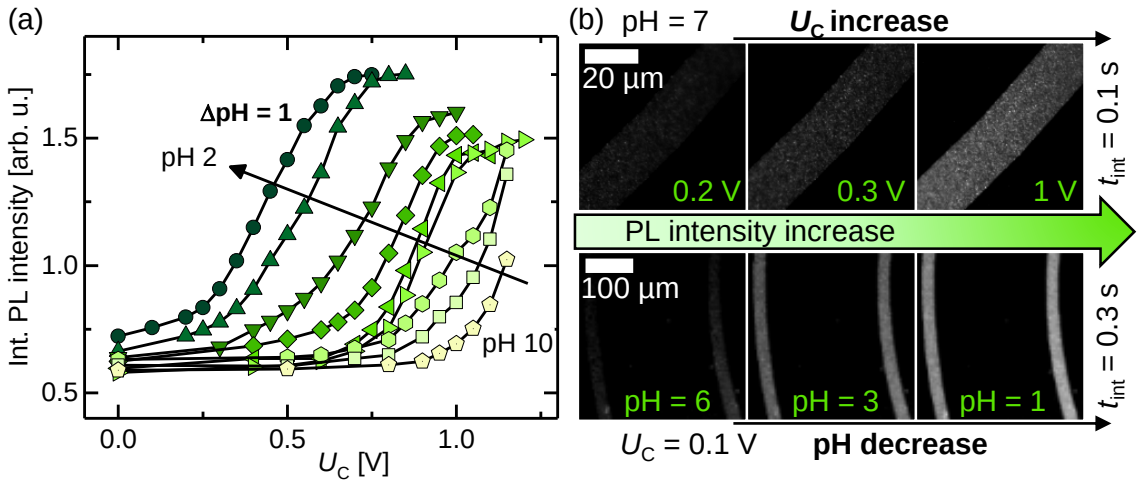

Figure 4.9: (a) Integrated fluorescence intensity as function of the cathodic bias and the electrolyte solution pH. Indicated as black arrow, the electrochemical working point with maximal PL sensitivity is marked. The integration time was $t_{\text{int}} = 100\,\text{ms}$ and the magnification was 63-fold. (b) Fluorescence images for a bias variation with $\text{pH} = 7$ and for the pH variation at $U_{\text{C}} = 0.1\,\text{V}$. The integration time was $t_{\text{int}} = 100\,\text{ms}$ (300 ms) and a 63-fold (tenfold) magnification was used for the bias increase (pH decrease).

The investigation of the fluorescence intensity as a function of pH and bias resulted in an increase of the intensity with increasing U_{C} for each pH value showing the same S-shape behavior as can be seen in figure 2.7. The intensity increases by $\Delta\text{PL} \approx 140\,\%$ from the

initial value at $\Delta U_C = 0\,V$ to the PL intensity at $\Delta U_C = 1.2\,V$ for acidic pH. In the alkaline pH range that intensity increase amounts to approximately $\Delta PL \approx 70\,\%$. The sensitivity is approximately 40 mV/pH for high pH values and approximately 200 mV/pH for low pH values. These slopes equal a pH difference of $\Delta pH = 0.025$ - 0.005 for a bias resolution of $\Delta U_C = 1\,mV$. The linear relation of PL intensity and U_C shifts to smaller U_C values with decreasing pH.

The fluorescence images in 4.9(b) demonstrate that the intensity increase due to the bias application of $U_C = 0.2/0.3/1\,V$ at $pH = 7$ and the pH changes by using $pH = 6/3/1$ at $U_C = 0.1\,V$ can be displayed even with the use of small integration time of $t_{int} = 100/300\,ms$. The distinction is possible without the need of image editing.

To study the achievable bias and pH resolution limits of the InGaN/GaN NWH arrays, the bias resolution was investigated by variation of $U_C = 600\,mV$ to $U_C = 700\,mV$ in $\Delta U_C = 10\,mV$ steps and then from $U_C = 670\,mV$ to $U_C = 680\,mV$ with a step size of $\Delta U_C = 1\,mV$. For this study, a 10 mM PBS solution with $pH = 7.2$ was used. The bias resolution was studied applying bias potentials of the linear range at $pH = 7.2$, demonstrating the highest sensitivity which is from $U_C = 600$ - 700 mV according to the calibration curve in figure 4.9. The achievable pH resolution was studied in dependence of the time with $pH = 7$ and at a bias potential of $U_C = 400\,mV$. Then, the solution was exchanged with maximal speed of $v_{pump} = 19.26\,ml/min$ to $pH = 6.84$ and $pH = 6.97$, respectively. The images were recorded every second with an integration time of $t_{int} = 500\,ms$ and $t_{int} = 300\,ms$. The results are shown in figure 4.10.

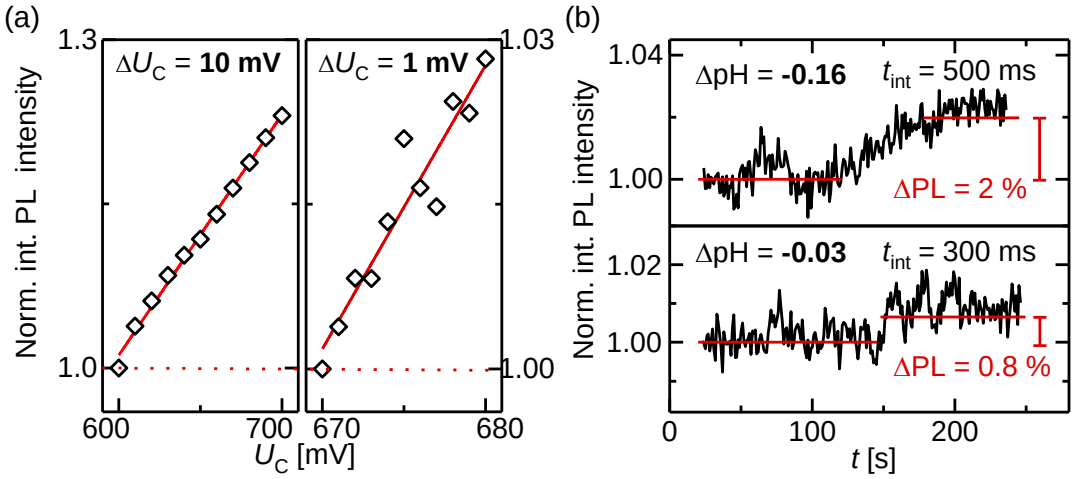

Figure 4.10: (a) Normalized integrated PL intensity of an InGaN/GaN NWH array for a PBS solution with $pH = 7.2$ in dependence of U_C from $U_C = 600$ - 700 mV with $\Delta U_C = 10\,mV$ and from $U_C = 670$ - 680 mV with $\Delta U_C = 1\,mV$. 1 mV bias steps can be clearly resolved. The linear regressions (displayed in red) serve as guide to the eye. The integration time $t_{int} = 100\,ms$ and an objective lens with 63-fold magnification were used. (b) Normalized integrated fluorescence intensity as a function of the time and the pH at $U_C = 400\,mV$. Both the pH step of $\Delta pH = -0.16$ and $\Delta pH = -0.03$ can be resolved. The integration times were $t_{int} = 500\,ms/300\,ms$ and a tenfold objective lens was used.

The investigation of the bias resolution reveals that bias steps of $\Delta U_C = 1$ mV with the use of only $t_{int} = 100$ ms for integration can be clearly resolved. The change of the PL

intensity with U_C is $(0.220 \pm 0.005)\,\%/\mathrm{mV}$ for $\Delta U_C = 10\,\mathrm{mV}$ and $(0.258 \pm 0.029)\,\%/\mathrm{mV}$ for $\Delta U_C = 1\,\mathrm{mV}$. The maximal difference between the bias voltage of the experiment with steps of $\Delta U_C = 1\,\mathrm{mV}$ and the bias voltage obtained from the linear regression is $\Delta U_{C,\mathrm{max}} = 2.4\,\mathrm{mV}$.

The transient fluorescence measurements investigating the pH resolution demonstrate that pH changes of $\Delta\mathrm{pH} \leq 0.03$ with an integration time of $t_{\mathrm{int}} = 300\,\mathrm{ms}$ can be resolved. The PL intensity increases by $\Delta\mathrm{PL} = 2\,\%$ with a pH decrease of $\Delta\mathrm{pH} = \text{-}0.16$ and by $\Delta\mathrm{PL} = 0.8\,\%$ with a pH decrease of $\Delta\mathrm{pH} = \text{-}0.03$.

The resolution limits that can be achieved depend on the sample structure and primarily on the measurement settings. For the resolution, the integration time t_{int} plays a crucial role as this parameter determines the maximum potential signal-to-noise ratio (SNR). Hence, the SNRs of the fluorescence images of the InGaN/GaN NWH samples were investigated as a function of the integration time t_{int} and of the applied cathodic bias voltage U_C. The fluorescence intensities were transiently recorded when U_C was varied between 0 V and U_C and then again back to 0 V. The bias steps ΔU_C were $\Delta U_C = 100\,\mathrm{mV}$ from 0 V to $U_C = 1\,\mathrm{V}$. These bias-dependent transients were analyzed for $t_{\mathrm{int}} = 25$, 50, 100 mV. For the SNR studies, a 10 mM PBS solution with pH = 7.2 was used. The results are shown in figure 4.11.

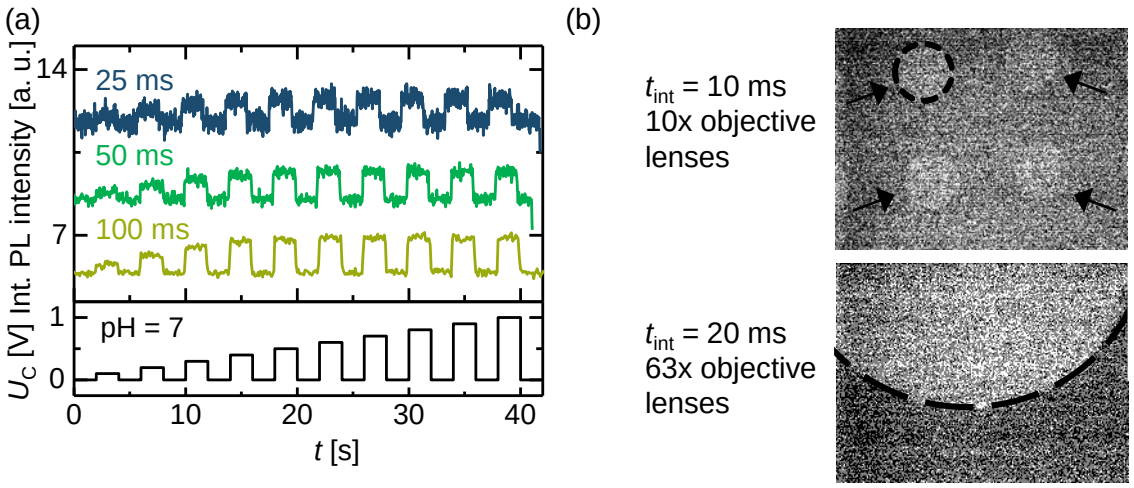

Figure 4.11: (a) Integrated PL intensity as a function of the applied bias potential from $U_C = 0$ - 1 V with an increasing step size of $\Delta U_C = 100\,\mathrm{mV}$. The integration time was varied between $t_{\mathrm{int}} = 25\,\mathrm{ms}, 50\,\mathrm{ms}$ and $t_{\mathrm{int}} = 100\,\mathrm{ms}$. A tenfold objective lens was used. (b) Fluorescence images with an integration time of $t_{\mathrm{int}} = 10\,\mathrm{ms}$ can be resolved. The patterned sample structure (NWs are indicated as black dotted line) is visible due to the increase of PL intensity. Doubling of the integration time to $t_{\mathrm{int}} = 20\,\mathrm{ms}$ allows the clear discrimination between the area with and without nanowires. The applied bias was $U_C = 1\,\mathrm{V}$. The images were adjusted by an automatic white balance.

The transient bias-dependent results show that with increasing integration time from $t_{\mathrm{int}} = 25\,\mathrm{ms}$ to $t_{\mathrm{int}} = 100\,\mathrm{ms}$, the noise amplitude decreases and the bias resolution is increased. As a result, the bias differences ($\Delta U_C = 100\,\mathrm{mV}$) at higher U_C can be resolved more clearly. The fluorescence images in figure 4.11(b) demonstrate that with application of an external bias potential of $\Delta U_C = 1\,\mathrm{V}$ even the reduction of the integration time down

to $t_{\mathrm{int}} = 10\,\mathrm{ms}$ allows to identify the areas with fluorescing nanowires.
The signal-to-noise ratio SNR was investigated as function of ΔU_{C} and t_{int}. It is determined according to

$$SNR = \frac{\overline{I}(U_{\mathrm{C}})}{\sigma(\overline{I}(U_{\mathrm{C}}))} \tag{4.1}$$

where $\overline{I}$ is the mean integrated intensity at U_{C} and σ is the standard deviation. The calculated SNR values are plotted as a function of the integration time t_{int} and the bias U_{C} and are shown in figure 4.12.

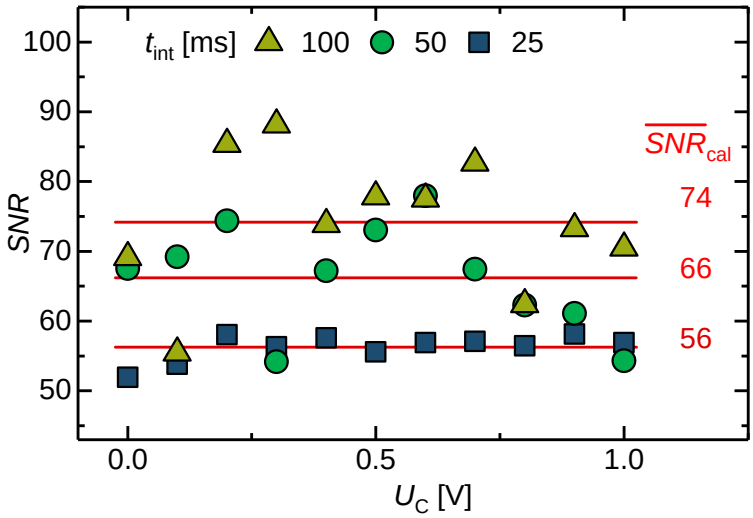

Figure 4.12: Calculated SNR values as function of ΔU_{C} and t_{int}. The mean values $\overline{SNR}_{\mathrm{cal}}$ are indicated in red.

The SNRs do not show a systematic dependence on ΔU_{C}, but increase with increasing t_{int}. The calculated mean signal-to-noise ratios are $\overline{SNR}_{\mathrm{cal}} = 56$ ($t_{\mathrm{int}} = 25\,\mathrm{ms}$), $\overline{SNR}_{\mathrm{cal}} = 66$ ($t_{\mathrm{int}} = 50\,\mathrm{ms}$) and $\overline{SNR}_{\mathrm{cal}} = 74$ ($t_{\mathrm{int}} = 100\,\mathrm{ms}$). The increase of the integration time from $t_{\mathrm{int}} = 25\,\mathrm{ms}$ to $t_{\mathrm{int}} = 100\,\mathrm{ms}$ increases the signal-to-noise by a factor of 1.32.
The transient measurement to analyze the time resolution was investigated by buffer solution exchange and thus, generating a pH-step of $\Delta\mathrm{pH} = 4$. The fluorescence images were recorded with an integration time of $t_{\mathrm{int}} = 100\,\mathrm{ms}$ at $U_{\mathrm{C}} = 1\,\mathrm{V}$ when abruptly decreasing the pH from $\mathrm{pH} = 7$ to $\mathrm{pH} = 3$. The results are shown in figure 4.13.

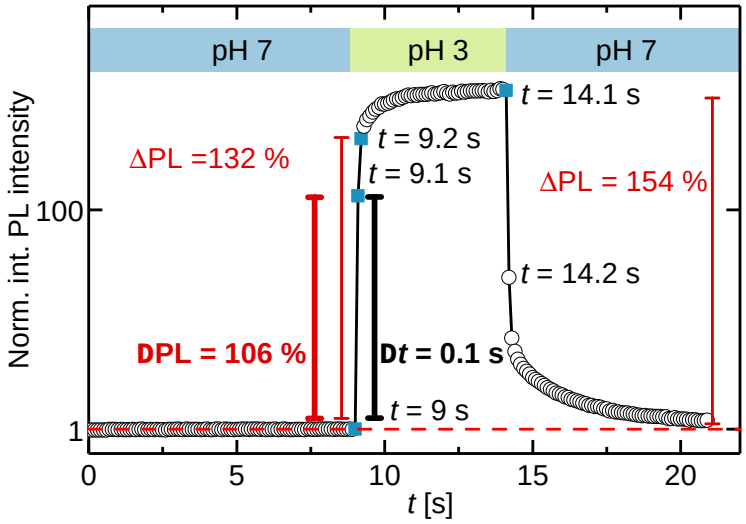

Figure 4.13: Time-resolved fluorescence measurement. The pH was decreased with $\Delta\mathrm{pH} = 4$ from $\mathrm{pH} = 7$ to $\mathrm{pH} = 3$ at $U_\mathrm{C} = 1\,\mathrm{V}$ using an integration time of $t_\mathrm{int} = 100\,\mathrm{ms}$ and a 63-fold objective lens.

The time-dependent measurement with a pH decrease of $\Delta\mathrm{pH} = 4$ demonstrates that these InGaN/GaN NWHs as OCEs allow the recording of changes in the surface potential with a PL change of $\Delta\mathrm{PL} = 106\,\%$ in less than $\Delta t < 100\,\mathrm{ms}$. The PL intensity increase is $\Delta\mathrm{PL} = 154\,\%$ within the pH change.

4.3.3 Imaging of Activity of Na^+/H^+-Exchanger

The basic characterization and the analysis of the InGaN/GaN nanowire heterostructures with a standard fluorescence optical microscope demonstrate that such arrays are ideally suited for the application as optochemical electrodes. The NWH arrays possess a high sensitivity of the PL intensity towards local changes of the pH and the bias voltage since the electrochemical working point can be well-defined. In addition, the GaN surface demonstrated a high electrochemical stability in aqueous environments [13–15, 207]. As a consequence, InGaN/GaN NWHs as OCEs enable the realization of time- and space-resolved imaging of extracellular biochemical reactions that are accompanied by local bias or pH changes.

As a proof of concept for the imaging of biochemical transport mechanisms, the cellular transport via the electro-neutral sodium/proton (Na^+/H^+) antiport was analyzed. For this purpose, isolated intestinal crypts from Wistar rats were investigated [3]. Usually, the NHE activity is studied as a function of the intracellular pH [199, 208, 209] since there is a scarcity of extracellular detection methods. Ion-sensitive field-effect transistors (ISFETs) enabled the detection of extracellular pH changes in the vicinity of the cell [156, 210]. However, these methods lacked the possibility of a spatially resolved evaluation and thus, bioimaging was not demonstrated.

[3] The isolation procedure was performed by Dr. med. vet. Sandra Bader, vet. Lena Lottig and Ervice Pouokam, Ph.D of the research group of Prof. Martin Diener (Institute for Veterinary Physiology and Biochemistry, Justus Liebig University, Giessen, Germany).

The NHE activity was altered and monitored due to externally induced reduction or enhancement of the NHE activity. The reduction of the NHE activity is realized by two different techniques: inhibition due to blocking or indirect deactivation.
The indirect deactivation of the NHE was realized using a 1.3 mM 2,4-Dinitrophenol (DNP) solution. DNP is a proton transporter that acts as an uncoupler of the oxidative phosphorylation in mitochondria of cells. The oxidative phosphorylation (OXPHOS) is a metabolic pathway where the cells oxidize the essential nutrients enzymatically. In general, the OXPHOS is based on two main mechanisms which are the electron transport chain and the movement of ions across the cell membrane (chemiosmosis). During chemiosmosis, energy is stored which is consumed while ATP production. Both processes must be active to ensure the proper cell function. At the end of the electron transport chain, oxygen accepts the electrons and establishes the completion of the oxidative phosphorylation. In the absence of oxygen, the phosphorylation process is interrupted and as a consequence, the ATP production is inhibited. The presence of DNP results in the decomposition of proton gradients and the energy stored for the ATP production is released in form of thermal energy. This means that those pumps depending on ATP, such as the sodium/potassium (Na^+/K^+) pump, located in the basolateral membrane of enterocytes (crypt cells), show reduced activity (cf. section 4.2.2). Na^+/K^+-pumps release three Na^+-ions and have an uptake of two K^+-ions in turn. This non-stoichiometric exchange results in a concentration gradient which energizes the Na^+/H^+-exchanger for the uptake of the non-stoichiometric lacking Na^+-ion. The indirect deactivation by DNP reduces the exchange of Na^+-ions with H^+-ions [197] and less protons are released into the extracellular space [202]. The decreasing number of protons in the extracellular region is equivalent to an extracellular alkanization that induces a decrease in PL intensity.
To study the proper cell function, the PL intensity of the OCEs was investigated as a function of time before and after the addition of 1.3 mM DNP solution to the electrolyte solution. The fluorescence images were transiently recorded. In the beginning of the measurement, the system was perfused with modified Tyrode´s solution at $pH = 7.4$. For all biochemical experiments, modified Tyrode´s solution with $pH = 7.4$ was used to mimic the physiological environment of vital cells. DNP solution was directly added into the chamber. The perfusion was stopped a few minutes before the addition of DNP which allowed to make a direct relation to the additive and to avoid experimental artefacts. The images were recorded at $U_C = 200\,mV$ with $t_{int} = 250\,ms$. The results in terms of integrated intensity/area as a function of the buffer solution and the cell activity due to the monitoring of the extracellular pH are shown in figure 4.14.

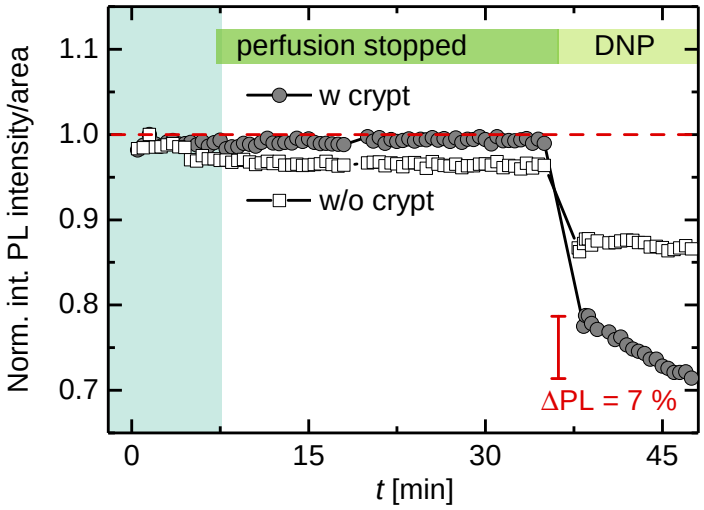

Figure 4.14: Integrated PL intensity/area of InGaN/GaN NWHs as a function of modified Tyrode´s solution without and with DNP solution. After the addition of DNP solution to the electrolyte solution, the PL intensity of the area without crypt remains constant after an initial drop. In contrast, the PL intensity of the area with crypt initially drops and then decreases. The images were recorded at $U_C = 200\,\mathrm{mV}$ using an integration time of $t_{int} = 250\,\mathrm{ms}$ and a tenfold objective lens.

The fluorescence intensities are not altered when the samples are perfused with buffer solution. The results do not show a change of the fluorescence intensities when the perfusion of the sample surface with modified Tyrode´s solution is stopped. Directly after the additon of the DNP solution into the measurement chamber, the fluorescence intensities in both areas decrease. This can be attributed to the enhanced light absorption of the altered composition of the electrolyte solution. Subsequently, the fluorescence intensity of the area without crypt shows the same magnitude after the first decrease, but the fluorescence intensity of the area with crypt shows a linear decrease. This can be explained by the decline of the NHE activity due to the indirect NHE inhibition by the deduction of the energy that was provided by ATP. The ATP reduction is reported to reduce the NHE activity [200, 201]. This finding allows to relate the pH changes to the cell activity by energy depletion.
The estimation of the pH change from the PL changes by $\Delta PL = 7\,\%$ is $\Delta pH = -1.85$ which is comparable to the findings in ref. [197] with $\Delta pH = -1$. The estimation of the pH change was calculated by reference to the sample´s calibration curve which is shown in figure 4.15.

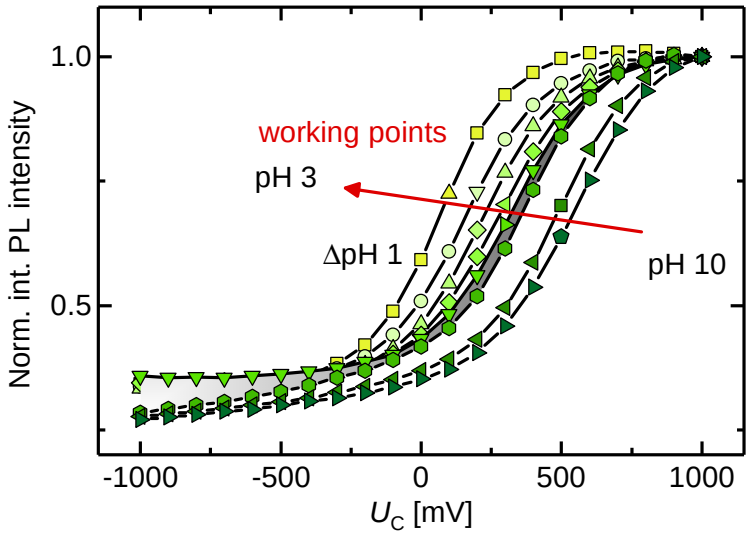

Figure 4.15: Calibration curve for bioimaging experiments. The images were recorded using a 40x objective lens and an integration time of $t_{\text{int}} = 100\,\text{ms}$.

The calibration curve shows the normalized integrated intensity as function of the pH and U_C. The pH changes in the biochemical experiments were estimated by using the sensitivity in the linear range of 35.8 mV/pH (cf. grey section lining in figure 4.9).
Moreover, the NHE activity was investigated by directly blocking the antiport with a NHE inhibitor and by stimulating the NH_3 uptake by the cell in the same experimental sequence. The NHE is an integral transport protein that, among others, regulates the intracellular pH by means of the hydrogen transport (cf. section 4.2.2). This transport mechanism can be inhibited by the use of appropriate inhibitiors such as amiloride and the amiloride derivates that occupy the Na^+-binding sites in the extracellular space [196] (cf. section 4.2.2). The inhibition of the exchanger disables the exchange of the sodium with hydrogen with the result that the extracellular hydrogen concentration is reduced and thus, the pH increases. Here, the inhibition is realized by the addition of 0.1 mM amiloride to the buffer solution.
Another method to monitor the change of the extracellular pH caused by the modification of the NHE activity by external stimuli is the use of ammonium chloride NH_4Cl. NH_4Cl is used as prepulse for the induction of a cellular acidification via acid load [199, 208, 211]. For the purpose of externally causing an extracellular acidification, 20 mM NH_4Cl was added to the buffer solution.
For spatially resolved analysis of the pH changes and the NHE activity, fluorescence images were recorded as a function of the buffer solution. The transient fluorescence images (1200 pixel x 1600 pixel resolution) were recorded by a monochrome charge-coupled device (CCD) camera with 211 megapixels and evaluated. The area of the OCEs with crypts and without were compared to allow the direct correlation of pH changes to the cell activity. The transient measurements were performet at $U_C = 200\,\text{mV}$ which is the working point for the sample at pH = 7.4. The results are shown in figure 4.16.

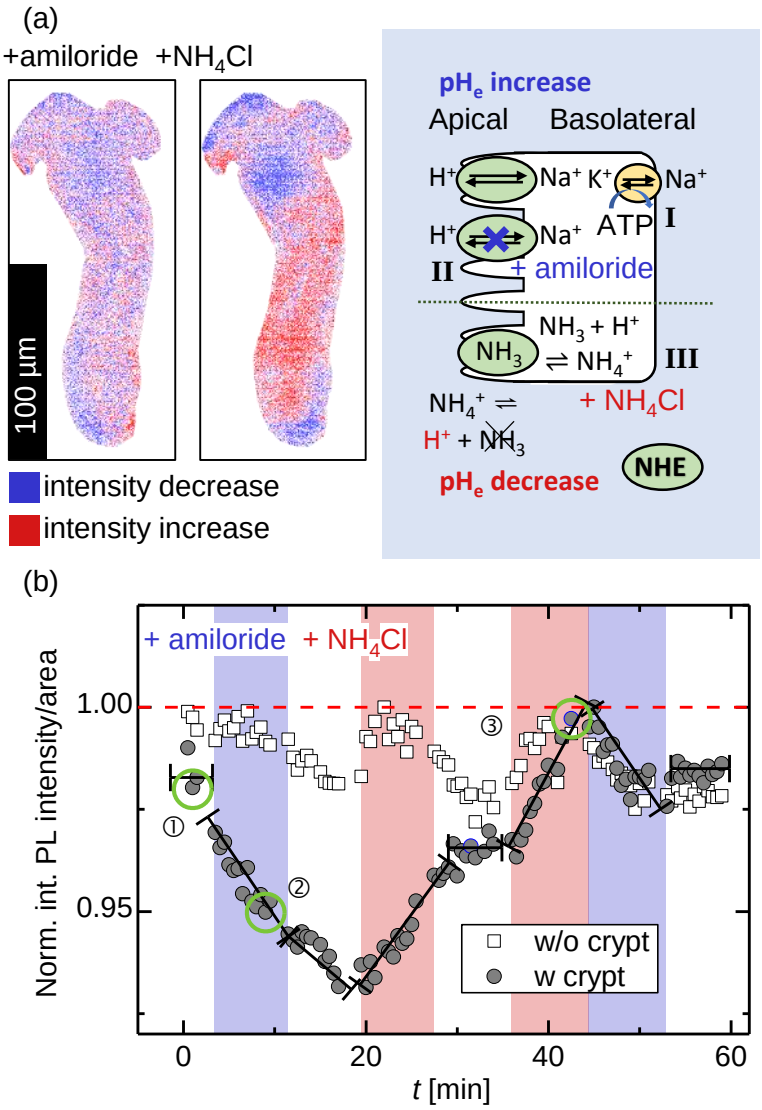

Figure 4.16: (a) Spatially resolved images of isolated intestinal crypt with biochemical contrast: the intensity increase is shown in red and the intensity decrease in shown is blue for the sequence in presence of 0.1 mM amiloride or 20 mM NH_4Cl. The three different mechanism of the imaged NHE activity are schematically displayed: indirect deactivation by DNP **I**, blocking by amiloride **II**, NH_3 uptake **III**. (b) Corresponding transient measurement of bioimaging the pH change by integrating the PL intensity of the area with and without crypt as function of the buffer solution with the addition of 0.1 mM amiloride or 20 mM NH_4Cl. The delay for the exchange of the electrolyte solution is considered. The images were recorded with $t_{\mathrm{int}} = 250\,\mathrm{ms}$ and using a tenfold lens. The applied bias was $U_{\mathrm{C}} = 200\,\mathrm{mV}$.

In figure 4.16(a) the calculated biochemical contrast in presence of amiloride or ammonium chloride is shown as difference of the fluorescence images recorded in the transient measurement in figure 4.16(b). The details of the calculation and the image processing are described in section 4.1. The blue color represents a decrease of the fluorescence intensity, red color an increase. The addition of amiloride results in a decrease of the fluorescence intensity. The decrease occurs almost homogeneously in the entire area of the surface of the crypt (cf. figure 4.16(a), left). This finding is consistent with the results of the transient measurement of the OCE covered with the crypt shown in figure 4.16(b). Here, a distinct intensity decrease in the sequences where amiloride is present is observable. In contrast, the area of the OCE without crypt only demonstrates negligible changes in the fluorescence intensity that can be explained by small fluctuations of the buffer solution temperature. Since the findings are reversible and similar for the same sequences when amiloride is present, the intensity decrease that is equal to a pH increase for the InGaN/GaN NWHs can be solely attributed to the cell activity. These findings demonstrate that the induced alkalization results from the inhibition of the NHE via amiloride-blocking.
In contrast, the results showing the chemical contrast for the addition of NH_4Cl (cf. figure 4.16(a), right) depict a pronounced increase of the fluorescence intensity that is predominant in the lower third of the cell ("fundus", cf. section 4.2.2, figure 4.3). The transient measurements, too, show a reversible intensity increase in presence of NH_4Cl (cf. figure 4.16(b)). Different from other experiments where NH_4Cl is used as prepulse, this method cannot explain the findings here. The mechanism proposed here is the intracellular alkanization due to the uptake of NH_3 which is schematically shown in figure 4.17.

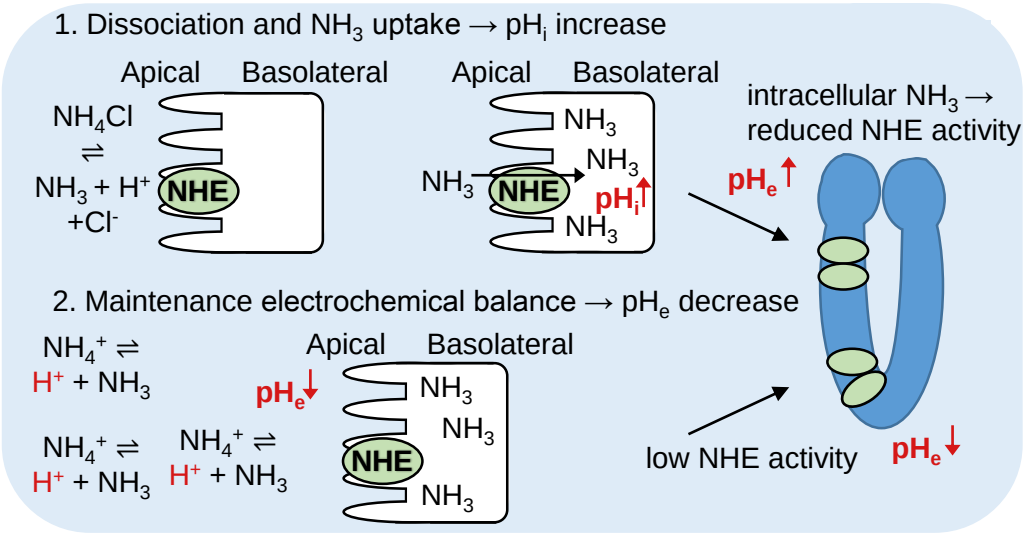

Figure 4.17: Schematic presentation of pH change due to the uptake of NH_3. The intracellular pH is denoted as "pH_i" and the extracellular pH as "pH_e"
1. NH_3 uptake into the cell realized by nonionic diffusion → pH_i increases. 2. Maintenance of electrochemical equilibrium by enhanced NH_4Cl dissociation → pH_e decreases. The NH_3 uptake preferentially occurs in the upper third of the cell. Since these cells are more differentiated, the pronounced NHE activity is reduced due to the alkanization.

NH_4Cl dissociates into a proton and NH_3. NH_3 diffuses into the cell via nonionic diffusion resulting in an intracellular pH increase at the first step. To maintain the electrochemi-

cal equilibrium, the NH_4^+-dissociation rate increases and thus, increases the extracellular hydrogen concentration which is detected by an increase of the fluorescence intensity. Particularly, the intensity increase in the lower part of the cell is an indication for this proposed mechanism. In the lower part of the crypt, commonly called fundus, most of the cells are undifferentiated cells which do only possess a low NHE activity [199]. The cells which are more differentiated are located in the upper part of the crypt (surface) and have a higher activity of NHE exchange such as the Na^+-absorption. The uptake of NH_3 results in an intracellular alkanization which reduces the NHE activity and thus, the proton export via NHE is reduced. As a consequence of the reduced NHE exchange activity, the extracellular acidification in the upper part of the crypt is affected. On the contrary, the fluorescence intensity decrease found in the lower part of the crypt can be explained by a mismatch of the cell position for the data processing.
The slopes of the various sequences in transient measurement in figure 4.16(b) were analyzed and compared. The determined results are summarized in table 4.2.

Table 4.2: Calculated slopes which are the changes of the normalized intensity divided by the product of area and time for the sequences I and II in presence of 0.1 mM amiloride and 20 mM NH_4Cl in figure 4.16(b).

Slope $[10^{-3}/(\text{area} \cdot \text{min})]$	+ amiloride I	+ amiloride II	NH_4Cll I	NH_4Cl II
OCE area with crypt	-3.04	-2.44	3.17	3.96
OCE area	-0.37	-1.62	-0.88	0.85

The slopes of the integrated PL intensity show that the changes of the repetitive sequences are comparable. The results for the different sequences differ widely for the uncovered OCE area and the OCE area with crypt. The results allow the direct correlation of the changes in the fluorescence intensity with the NHE activity. Here, too, the intracellular alkanization due to the NH_3 uptake is measurable: the slope of the fluorescence signal induced by amiloride after the NH_3 uptake (amiloride II, table 4.2) is smaller than the slope in the first sequence where the intracellular pH is at physiological value (amiloride I, table 4.2). The NHEs expressed in the colon of rats are of type NHE-2, NHE-3 and NHE-4, but only NHE-2 and NHE-3 are amiloride-sensitive [196]. The inhibitory potency for NHE-2 is a hundred times higher than that of NHE-3 ($IC50\,(\text{NHE-2}) = 1\,\mu M$ and $IC50\,(\text{NHE-3}) > 100\,\mu M$) [196]. The pH-induced PL change of the crypt due to the presence of amiloride is probably mainly attributable to the NHE-2.
The transient fluorescence image analysis with DNP as indirect NHE de-activator allows assigning the observed changes of the PL intensity of the OCEs to the cell activity of the isolated intestinal crypts. In advanced studies using the NHE inhibitor amiloride for extracellular alkanization and NH_4Cl for extracellular acidification via NH_3 uptake, the changes of the PL intensity can be unambiguously correlated to the pH changes. These pH changes were estimated based on the calibration curves in figure 4.15 with the calculated sensitivity of 35.8 mV/pH which are $\Delta pH = +0.7$ for amiloride and $\Delta pH = -0.8$ for NH_4Cl. The pH changes from intracellular pH measurements that are based on fluorescent dyes are comparable to these findings with $\Delta pH \sim +0.5$ for amiloride [212] and $\Delta pH \sim 0.68$-

1.1 for NH_4Cl [195, 199, 212], but the values obtained here are consistent with additional information from spatial resolution. The approach shown here yielded reproducible measurements with only small variations of the absolute pH changes as demonstrated by figure 4.18 for a measurement with long sequences of modified Tyrode´s solution and the NHE inhibitor amiloride.

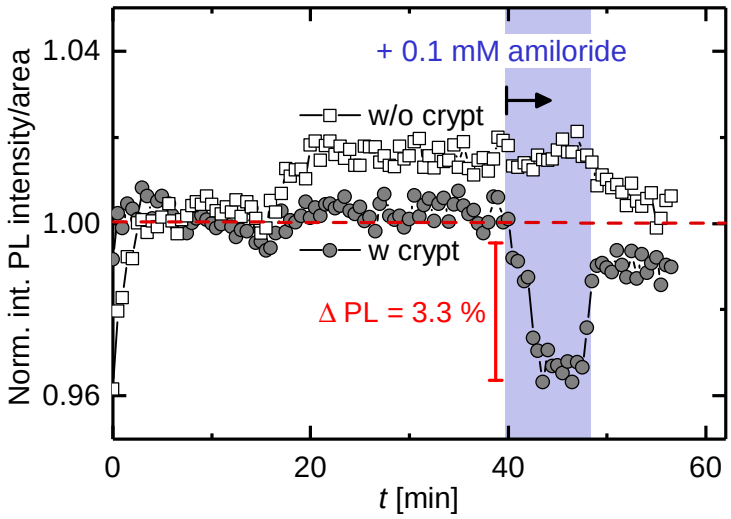

Figure 4.18: Transient recording of fluorescence changes due to the NHE inhibition with amiloride using long sequences of the respective buffer solutions. With the addition of 0.1 mM amiloride, the PL intensity of the area with crypt clearly decreases compared to the reference region. Even after 40 minutes of transient measurement with Tyrode´s solution, the biochemical activity of the isolated intestinal crypt was approved with an estimated pH change of $\Delta\text{pH} = +1.1$ by blocking with 0.1 mM amiloride. PL intensity variations of the reference region are assigned to small pH and temperature differences of the buffer solutions. The delay for the exchange of the electrolyte solution is considered. The images were recorded using an integration time of $t_{\text{int}} = 250$ ms and a tenfold lens. The applied bias was $U_C = 200$ mV.

These deviations originate from fluctuations in the biochemical activity of the investigated intestinal crypts. Considering the results obtained by three different measurements, the estimated pH change upon blocking of the NHE with amiloride in the buffer solution was $\Delta\text{pH}(\text{amiloride}) = (+0.78 \pm 0.23)$. The calculated pH change from the NH_3 uptake by NH_4Cl was determined to $\Delta\text{pH}(NH_4Cl) = (0.59 \pm 0.25)$.

Intracellular pH-measurement techniques based on the pH-sensitive fluorescent dye 2´,7´-bis(2-carboxyethyl)-5,6-carboxyfluorescein acetoxymethyl (BCECF/AM) are frequently used for the pH determination in cells (cf. refs. [199, 209]). However, this method has pratical drawbacks related to the signal gain due to dye leackage, a minimal fluorescence emission profile for pH changes, low signal-to-noise values in ratio imaging and bleaching [213]. Bleaching can only be reduced with the advanced method of fluorescence ratio measurement at two different photoexcitation wavelengths ($\lambda_{\text{exc}} = 490$ nm and $\lambda_{\text{exc}} = 440$ nm with an emission at $\lambda_{\text{em}} = 535$ nm are recommended). However, this approach suffers from fast bleaching since it inhibits the calculation of the ratio.

Currently published methods to monitor the extracellular pH such as the ratiometric flu-

orescence technique demonstrated a simultaneous high spatiotemporal resolution [214]. Nevertheless, with $\Delta\mathrm{pH} = 0.1$, the pH resolution of InGaN/GaN NWHs ($\Delta\mathrm{pH} = 0.03$) is considerably higher. In addition, the application of these ratiometric fluorescence probes is only possible in weak alkaline or acidic environments due to stability problems [214]. Another approach is based on surface-enhanced Raman scattering (SERS). Using SERS, a subendosomal spatial resolution can be achieved, but this method possesses a very limited temporal resolution and a comparably small pH resolution of $\Delta\mathrm{pH} = 0.2$ [215].

4.4 Summary and Conclusion

InGaN/GaN nanowire arrays as optochemical electrodes in combination with a standard optical microscope are very well-suited for the optical readout and imaging of biochemical processes that are based on pH or bias changes. In contrast to methods with optical detection mechanisms that are commonly used up to now, such as fluorescent dyes or semiconductor QDs, the capability of externally adjusting the working point of InGaN/GaN NWH arrays allows operation with high sensitivity in acidic, neutral and alkaline aqueous environments. Moreover, the long-term stability was demonstrated which enables the monitoring of biochemical processes to locate the changes with a subsequent quantification.

The bias resolution is $\Delta U_\mathrm{C} \leq 1\,\mathrm{mV}$ and a pH resolution of $\Delta\mathrm{pH} \leq 0.03$ was demonstrated. By application of the proper bias voltage, the detection of pH changes with a time resolution of $\Delta t \leq 50\,\mathrm{ms}$ was shown. A further reduction of the integration time is possible, but the adjustment of the different settings is associated with losing bias/pH resolution and shifting the resolution limits to higher values. The signal-to-noise ratio increases by $\Delta SNR = 30\,\%$ when the integration time increases from $t_\mathrm{int} = 25$ ms to $t_\mathrm{int} = 100$ ms.

The reduction and the enhancement of the activity of the sodium/proton exchanger was successfully detected using InGaN/GaN NWH arrays. In addition, the pH changes due to the blocking by amiloride and the NH_3 uptake in terms of imaging with biochemical contrast were visualized. The effects were localized and attributed to the inhibition of the NHE activity homogeneously along the surface of the crypt. Here, the higher number of differentiated cells in the upper part of the crypt showed an alteration of the activity due to the NH_3 uptake. Subsequently after the imaging, the externally induced pH changes of the crypt were quantified using the calibration curve to $\Delta\mathrm{pH} =$ -0.7 for the blocking with amiloride and to $\Delta\mathrm{pH} = +0.8$ for the NH_3 uptake in presence of NH_4Cl. These pH changes are in agreement with other published results that investigated the respective intracellular pH changes. InGaN/GaN NWH arrays enable the imaging of biochemical processes with chemical contrast possessing a spatial resolution of below $\Delta\mathrm{x} < 0.63\,\mu\mathrm{m}$ with the possibility of simultaneous quantitative analysis of the pH changes.

The imaging of pH changes with InGaN/GaN NWH OCEs due to the cell activity was demonstrated. Furthermore, the pH of the electrolyte solution can be adjusted to enable the detection and visualizing of electrical changes that are caused by electrogenic cells or alternatively, the NWs could be used for the electrical stimulation of cells. For this

purpose, the NHW arrays allow of an improvement of the aspect ratio as well as improved time and spatial resolutions. As a result the sensitivity and resolution of the OCEs are enhanced so that the biochemical imaging of neuronal action potentials becomes possible. Besides conductive silicon substrate, also transparent sapphire can be used as growth template to improve the localization of the pH and bias changes and that inverse optical microscopes can be applied which improves the operability with various cell types and enables collection statistics.

The use of InGaN/GaN NWH arrays as optochemical electrodes in combination with techniques of the fluorescence microscopy establishes the biochemical imaging of local processes. Possible applications are the tracking of intracellular events such as the cell metabolism (proliferation and apoptosis) [216], the contractility of muscular cells [217] and neural activity [218].

Chapter 5

Summary

InGaN/GaN NWH and GaN NW electrodes were presented for the successful application as multifunctional optical biosensors.
In the first part of the work, both electrode materials were analyzed in view of the charge transfer processes at the NW/electrolyte interface by simultaneous PL and PC measurements. InGaN/GaN NWH electrodes can be applied for the detection of ascorbic acid, uric acid and hydrogen peroxide. The detection is based on the proper selection of the working point that allows to switch between the reduction or oxidation of the biomolecules. The simultaneous recording of PL intensity and the PC density allows the assignment of the changes to one of the three molecules in a sample solution. The influence of the molecules on the PL and PC characteristics of InGaN/GaN NWH electrodes by the variation of the barrier height or SBB due to proton adsorption was suggested.
The successful covalent linkage of photoresponsive donor-acceptor triad molecules to the GaN NW surface was demonstrated. The charge separation state was studied by simultaneous PL and PC measurements. The results showed a decrease in the PL intensity in presence of the generation of the charge-separated state that could exclusively be attributed to a photo-induced change of the charge transfer between the NWs and the triad molecules. It was demonstrated that the photoactivation of the triad molecule reduces the effective barrier height. The details of the charge transfer via the fullerene, which forms one part of the triad molecule, are not clear, yet. However, the use of GaN NW electrodes with photoactive molecules was demonstrated for the first time. In addition, it was shown that surface states are relevant for the performance of the electrode.
The application of InGaN/GaN NWHs as optochemical electrodes for dynamic (bio-)chemical imaging with a standard optical microscope was presented. The photoelectrochemical stability of InGaN/GaN NWH arrays is comparable to currently used methods. In contrast to that, solely InGaN/GaN NWHs showed that the application in a broad pH range from acidic to alkaline solution is possible due to the possibility to define the electrochemical working point. The NWH electrodes demonstrated a bias resolution below 1 mV and a pH resolution below 0.03. The spatial resolution was determined to 0.63 μm. The dynamic imaging of cell activity was presented by the local extracellular pH monitoring of the sodium/proton exchanger of isolated intestinal crypts of Wistar rats. The quantified pH changes were in agreement with commonly used intracellular pH measurement methods.

List of Figures

List of Tables

Appendix A

Reagents

- Carl Roth, Karlsruhe, Germany:
  NaCl (purity $> 99.8\,\%$), Na_2HPO_4 ($\geq 99.5\,\%$), KH_2PO_4 ($\geq 98\,\%$), KCl ($\geq 99\,\%$), glucose ($\geq 99.5\,\%$), 4-(2-Hydroxyethyl)piperazine-1-ethanesulfonic acid (HEPES, $\leq 99.5\,\%$), L(+)-ascorbic acid ($\geq 99\,\%$), uric acid ($\geq 99\,\%$).
- Merck Millipore, Darmstadt, Germany:
  $CaCl_2 \cdot 2\,H_2O$($\geq 99\%$), $MgCl_2 \cdot 6\,H_2O$ ($\geq 99\,\%$).
- Sigma-Aldrich, Steinheim, Germany:
  Amiloride (from $C_6H_8ClN_7O \cdot HCl \cdot xH_2O$, $\geq 98\,\%$, NH_4Cl ($\geq 99.5\,\%$), 2,4-Dinitrophenol (from $(O_2N)_2C_6H_3OH$, poly(fluorescein isothiocyanate allylamine hydrochloride) (PAH-FITC, $M_{\text{PAH-FITC}} = 56000\,\text{g/mol}$), poly(allylamine hydrochloride) (PAH, $M_{\text{PAH}} = 15000\,\text{g/mol}$), poly(sodium 4-styrenesulfonate) (PSS, $M_{\text{PSS}} = 70000\,\text{g/mol}$), hydrogen peroxide (30 wt%).

Appendix B

Buffer Solutions

The preparation of the buffer solutions with a volume of $V = 1\,\mathrm{l}$ is described. The pH is adjusted with sodium hydroxide and hydrochloric acid.

B.1 Phosphate-Buffered Salt Solution

A 10 mM PBS solution with 137 mM NaCl and 2.7 mM KCl is obtained with:

- 8.18 g NaCl
- 1.44 g Na_2HPO_4
- 0.24 g KH_2PO_4
- 0.20 g KCl.

B.2 HEPES Solution

For a 100 mM 4-(2-Hydroxyethyl)piperazine-1-ethanesulfonic acid (HEPES) solution 23.831 g of HEPES were weighted into a 1 l volumetric flask and filled with bidestilled water.

B.3 Modified Tyrode´s Solution

Modified Tyrode´s solution with 140 mM NaCl, 1 mM phosphate buffer, 5.4 mM KCl, 12.2 mM glucose, 1.25 mM $CaCl_2$ and 1 mM $MgCl_2$ was used for the bioimaging measurements of intestinal crypts. 1 ml of 1.25 M $CaCl_2$ and of 1 M $MgCl_2$ solution were added and the salts were weighed to:

- 8.18 g NaCl
- 0.29 g Na_2HPO_4
- 0.03 g NaH_2PO_4
- 0.40 g KCl
- 2.20 g glucose.

Appendix C

Surface Functionalization with APTES

(1) The samples were cleaned consecutively in acetone and isopropyl alcohol for $t = 1\,\text{min}$ each using an ultrasonic bath with a power of $P = 110\,\text{W}$. Then, the samples were dried under oxygen flow.

(2) The samples were oxidized for $t = 20\,\text{min}$ in sulfuric acid (96 %) and hydrogen peroxide (30 %) in a ratio of 3:1. H_2O_2 was added to sulfuric acid and the mixture was stirred. After oxidation, the samples were cleaned in bidestilled water and dried under oxygen flow.

(4) Another oxidation step followed by UV/O_3 treatment for $t = 30\,\text{min}$. The samples were stored in a desiccator for $t \geq 2\,\text{h}$ to reduce the water content.

(5) For silanization a 20 mM APTES solution with $V = 50\,\text{ml}$ anhydrous toluene and $V = 234\,\mu\text{L}$ APTES ($c \geq 98\,\%$) are mixed in the reactor. The glas ware was pre-rinsed with anhydrous toluene before preparation. The samples were put in the reactor which was closed with a glass lid. The silanization proceeds for $t = 90$ min at a temperature of $\vartheta = 45\,°\text{C}$ using the ultrasonic bath ($P = 110\,\text{W}$). The temperature should not rise above $\vartheta = 51\,°\text{C}$, otherwise cross-linkage takes place. To avoid the evaporation of the solvent, the glass lid and the reactor were sealed with parafilm.

(6) After silanization, the samples rested for $t = 60\,\text{min}$. The ultrasonic bath was turned off and cooled with ice to reduce the temperature to stop the reaction.

(7) For cleaning, the samples were rinsed with anhydrous toluene. Next, the samples were cleaned in anhydrous toluene for $t = 15$ min using the ultrasonic bath ($P = 110\,\text{W}$). The pre-rinsing and the cleaning is repeated with isopropyl alcohol.

(8) Removal of unbound and physisorbed APTES molecules was realized by the use of diluted acetic acid. The samples were pre-rinsed with diluted acetic acid with pH = 4 ($V_{\text{acetic cid}} = 3.13\ \mu\text{L}$, (100 w.-%) in $V = 100\,\text{ml}$ bidestilled water). Next, the samples in the diluted acetic acid were mounted on a vortexer (lowest setting) and cleaned for $t = 30\,\text{min}$.

(9) The samples were rinsed with bidestilled water and dried under oxygen flow. Then, the samples were stored light protected in a desiccator until use ($t \geq 12\,\text{h}$).

Appendix D

Isolation of Intestinal Crypts

The isolation procedure was performed by Dr. med. vet. Sandra Bader, vet. Lena Lottig and Ervice Pouokam, Ph.D of the research group of Prof. Martin Diener (Institute for Veterinary Physiology and Biochemistry, Justus Liebig University, Giessen, Germany).
For bioimaging, isolated intestinal crypts from Wistar rats were used. Rats of both sexes with a body mass of about $m = 200 \pm 20\,\mathrm{g}$ were used for the experiments, since only the animals with $m \leq 220\,\mathrm{g}$ feature intact crypts [219]. The laboratory animals were all bred and housed at the institute of veterinary physiology and biochemistry of the Justus-Liebig-University, Giessen. The rats were kept in a $12\,\mathrm{h} : 12\,\mathrm{h}$ light-dark cycle at $\vartheta = 22.5\,^{\circ}\mathrm{C}$ with an air humidity of 50 - 55 %. The rats were offered free access to food and water before the time of the experiment.
The animals are collected in their home cages that contain ambient air (20 % O_2) where they stay until the start of the experiment. To avoid anxiety, the cages are covered with a CO_2 delivery lid that is connected to a CO_2 gas cylinder. The rats are narcotized by CO_2-anesthesia with a CO_2-flow rate of approximately 20 % of the cage volume/min.
The loss of consciousness is tested by checking the loss of righting reflex. After the removal of the rats from the cage, the death is assured by physical methods because the CO_2-anesthesia is reversible. The physical methods involve the cervical dislocation and an exsanguination which are approved by the named animal welfare officer of the Justus-Liebig-University, administrative number 487_M and conducted according to the German and European animal welfare law.
The isolation of enteric crypts was conducted according to ref. [219]. In doing so, the colon was removed from the rats and flushed with an ice-cold Tyrode buffer solution where the colon was kept until the following preparation steps. The isolation of the crypts included the stripping of the serosa and muscularis propria by hand. The cleaned colon was put on a small plastic rod ($d = 5\,\mathrm{mm}$) so that an incision could circularly be conducted at the anal end using a blunt scalpel. In proximal direction, the serosa and the lamina propria were gently removed. For the mucosa-submucosa preparation, the residues of the colon were glued to a plastic holder with a tissue adhesive. To solvate the crypts from the tissue, the plastic holder was incubated for about $t = 5\,\mathrm{min}$ to $t = 7$ min in an ethylendinitrilotetraacetic acid (EDTA) solution at $\vartheta = 38\,^{\circ}\mathrm{C}$. The incubation time was depending on the animals weight and thus, the tissue texture. After the incubation period, the tissue on the plastic holder was mounted in a Tyrode´s buffer solution with

high K^+-concentration and vibrated for $30 - 60\,\mathrm{s}$ to detach the isolated crypts from the tissue. The sample solution with isolated crypts was kept at $\vartheta = 4\,^\circ\mathrm{C}$ in the dark until the start of experiments .

List of Publications

Sara Sibylle Hölzel, maiden name Sara Sibylle Lippert

Dynamic Extracellular Imaging of Biochemical Cell Activity Using InGaN/GaN Nanowire Arrays As Nanophotonic Probes
S. Hölzel, M. V. Zyuzin, J. Wallys, E. Pouokam, J. Müßener, P. Hille, M. Diener, W. J. Parak, and M. Eickhoff
Advanced Functional Materials (2018)

Photoelectrochemical response of GaN, InGaN and GaNP nanowire ensembles
J. Philipps, **S. Hölzel**, P. Hille, J. Schörmann, S. Chatterjee, I. A. Buyanova, M. Eickhoff, and D. Hofmann
Journal of Applied Physics (2018)

Flexible Modulation of Electronic Band Structures of Wide Band Gap GaN Semiconductors Using Bioinspired, Non-Biological Helical Peptides
S. Mehlhose, N. Frenkel, H. Uji, **S. Hölzel**, G. Müntze, D. Stock, S. Neugebauer, A. Dadgar, W. Abuillan, M. Eickhoff, S. Kimura, and M. Tanaka
Advanced Functional Materials (2017)

InGaN/GaN nanowires as a new platform for photoelectrochemical sensors - detection of NADH
M. Riedel, **S. Hölzel**, P. Hille, J. Schörmann, M. Eickhoff and F. Lisdat
Biosensors & Bioelectronics, Vol. 94, p. 298-304 (2017)

High Precision Electrochemical Detection of Reversible Binding of Recombinant Proteins on Wide Band Gap GaN Electrodes Functionalized with Biomembrane Models
N. Frenkel, J. Wallys, **S. Lippert**, J. Teubert, A. Das, E. Monroy, S. Kaufmann, M. Eickhoff, and M. Tanaka
Adv. Func. Mat. 24, 4927-4934 (2014)

InGaN/GaN quantum dots as optical probes for the electric field at the GaN/electrolyte interface
J. Teubert, S. Koslowski, **S. Lippert**, M. Schäfer, J. Wallys, G. Dimitrakopulos, Th. Kehagias, Ph. Komninou, A. Das, E. Monroy, and M. Eickhoff
J. Appl. Phys. 114, 74313 (2013)

List of Scientfic Contributions

29.05. - 02.06.2017	Nanowire Week, Lund, Schweden
06.03. - 11.03.2016	DPG-Frühjahrstagung, Regensburg, Deutschland
02.10. - 07.10.2016	International Workshop on Nitride Semiconductors, Orlando, Florida
23.02.2016	SPIRITS Symposium “Creation of Bio-Inspired, Non-Biological Mesoscale Hybrid Materials”, Kyoto, Japan
18.11. - 19.11.2014	SPIRITS Kick-Off Symposium “Creation of Bio-Inspired, Non-Biological Mesoscale Hybrid Materials”, Kyoto, Japan

Bibliography

[1] J. Yin, Y. Hu, J. Yoon, *Chemical Society Reviews* **44**(14), 4619 (2015).

[2] K. Sokolov, et al. **63**, 1999 (2003).

[3] R. J. Gillies, N. Raghunand, G. S. Karczmar, Z. M. Bhujwalla, *Journal of Magnetic Resonance Imaging* **16**(4), 430 (2002).

[4] N. Chaniotakis, N. Sofikiti, *Anal. Chim. Acta* **615**(1), 1 (2008).

[5] M. Pohanka, J. Leuchter, *International Journal of Electrochemical Science* **12**, 6611 (2017).

[6] P. Bergveld, *IEEE Transactions on Bio-Medical Engineering* **17**, 70 (1970).

[7] S. Caras, J. Janata, *Analytical Chemistry* **52**(12), 1935 (1980).

[8] S. V. Dzyadevich, et al., *Biosensensors and Bioelectronics* **14**(3), 283 (1999).

[9] J. Fritz, E. B. Cooper, S. Gaudet, P. K. Sorger, S. R. Manalis, *Proceedings of the National Academy of Sciences* **99**(22), 14142 (2002).

[10] P. Bergveld, *IEEE Transactions on Biomedical Engineering* **19**(5), 342 (1972).

[11] H. Abe, M. Esaschi, T. Matsuo, *IEEE Transactions on Electron Devices* **26**, 1939 (1979).

[12] J. Wallys, J. Teubert, F. Furtmayr, D. M. Hofmann, M. Eickhoff, *Nano Letters* **12**(12), 6180 (2012).

[13] H. P. Maruska, J. J. Tietjen, *Applied Physics Letters* **15**(10), 327 (1969).

[14] J. I. Pankove, *Journal of The Electrochemical Society* **119**, 1118 (1972).

[15] G. Steinhoff, O. Purrucker, M. Tanaka, M. Stutzmann, M. Eickhoff, *Advanced Functional Materials* **13**(11), 841 (2003).

[16] G. Steinhoff, et al., *Applied Physic Letters* **86**(3), 033901 (2005).

[17] J. Yu, et al., *Biosensors and Bioelectronics* **23**(4), 513 (2007).

[18] B. Baur, et al., *Applied Physic Letters* **89**(18), 183901 (2006).

[19] B. Baur, et al., *Applied Physic Letters* **87**(26), 263901 (2005).

[20] G. M. Müntze, et al., *Biosensors and Bioelectronics* **64**(0), 605 (2015).

[21] G. M. Müntze, et al., *Biosensors and Bioelectronics* **77**, 1048 (2016).

[22] M. Riedel, et al., *Biosensors and Bioelectronics* **94**, 298 (2017).

[23] P. Neuderth, et al., *Journal of Materials Chemistry A* **6**(2), 565 (2018).

[24] J. M. Philipps, et al., *Journal of Applied Physics* **123**(17), 175703 (2018).

[25] P. Hille, *Advanced Group III-Nitride Nanowire Heterostructures – Self-Assembly and Position-Controlled Growth*, Ph.D. thesis, I. Physikalisches Institut, Justus-Liebig-Universität Gießen (2017).

[26] M. de la Mata, et al., *Nano Lett.* **12**(5), 2579 (2012).

[27] F. Furtmayr, et al., *J. Appl. Phys.* **104**(3), 034309 (2008).

[28] V. I. Lobyshev, R. E. Shikhlinskaya, B. D. Ryzhikov, *J. Mol. Liq.* **82**(12), 73 (1999).

[29] G. Tourbot, et al., *Nanotechnology* **22**(7), 075601 (2011).

[30] S. Albert, et al., *Crystal Growth & Design* **15**(6), 2661 (2015).

[31] T. Tabata, J. Paek, Y. Honda, M. Yamaguchi, H. Amano, *physica status solidi (c)* **9**(3-4), 646 (2012).

[32] X. Kong, et al., *physica status solidi (a)* **212**(4), 736 (2015).

[33] T. Kehagias, et al., *Nanotechnology* **24**(43), 435702 (2013).

[34] I. Vurgaftman, J. R. Meyer, L. R. Ram-Mohan, *J. Appl. Phys.* **89**(11), 5815 (2001).

[35] G. Tourbot, et al., *Nanotechnology* **23**(13), 135703 (2012).

[36] T. Kehagias, *Physica E: Low-dimensional Systems and Nanostructures* **42**(9), 2197 (2010).

[37] D. Cherns, et al., *Nanotechnology* **25**(21), 215705 (2014).

[38] K. D. Goodman, et al., *J. Appl. Phys.* **109**(8), 084336 (2011).

[39] J. M. E. Wallys, *Characterization of Group III–Nitride Nanowires for Bio–Electrochemical Sensors*, Ph.D. thesis, I. Physikalisches Institut, Justus-Liebig-Universität Gießen (2014).

[40] D. E. Yates, S. Levine, T. W. Healy, *Journal of the Chemical Society, Faraday Transactions 1* **70**, 1807 (1974).

[41] W. Steins, 'Funktionalisierte GaN-Oberflächen: Charakterisierung und Photostrukturierung', Diploma thesis, Walter Schottky Institut, Technische Universität München (2008).

[42] O. Weidemann, et al., *Appl. Phys. Lett.* **83**(4), 773 (2003).

[43] L. Caccamo, et al., *ACS Applied Materials & Interfaces* **8**(12), 8232 (2016).

[44] C. Y. Cummings, F. Marken, L. M. Peter, A. A. Tahir, K. G. U. Wijayantha, *Chemical Communications* **48**(14), 2027 (2012).

[45] S. M. Sze, K. K. Ng, *Physics of semiconductor devices*. John Wiley & Sons, Inc., Hoboken, New Jersey (2006).

[46] R. Dalven, *Introduction to Applied Solid State Physics: Topics in the Applications of Semiconductors, Superconductors, Ferromagnetism, and the Nonlinear Optical Properties of Solids*. Springer (1990).

[47] M. G. Walter, et al., *Chemical Reviews* **110**(11), 6446 (2010).

[48] K. Rajeshwar, *Fundamentals of Semiconductor Electrochemistry and Photoelectrochemistry*. Wiley-VCH Verlag GmbH & Co (2007).

[49] J. D. Beach, R. T. Collins, J. A. Turner, *J. Electrochem. Soc.* **150**(7), A899 (2003).

[50] C. G. Van de Walle, J. Neugebauer, *Nature* **423**(6940), 626 (2003).

[51] P. G. Moses, C. G. V. de Walle, *Appl. Phys. Lett.* **96**(2), 021908 (2010).

[52] H. Imahori, S. Fukuzumi, *Advanced Functional Materials* **14**(6), 525 (2004).

[53] W. H. Koppenol, J. F. Liebman, *J. Phys. Chem.-US* **88**(1), 99 (1984).

[54] I. Vurgaftman, J. R. Meyer, *Journal of Applied Physics* **94**(6), 3675 (2003).

[55] J. F. Sierra, J. Galbán, J. R. Castillo, *Analytical Chemistry* **69**(8), 1471 (1997).

[56] R. Wilson, A. Turner, *Biosensors and Bioelectronics* **7**(3), 165 (1992).

[57] G. Cerny, *Packaging Technology and Science* **5**(2), 77 (1992).

[58] A. Moody, S. Setford, S. Saini, *The Analyst* **126**(10), 1733 (2001).

[59] S. Caron, R. W. Dugger, S. G. Ruggeri, J. A. Ragan, D. H. B. Ripin, *Chemical Reviews* **106**(7), 2943 (2006).

[60] J. Wang, Y. Lin, L. Chen, *The Analyst* **118**(3), 277 (1993).

[61] C. Hadjok, G. Mittal, K. Warriner, *Journal of Applied Microbiology* **104**(4), 1014 (2008).

[62] C.-M. Lin, S. S. Moon, M. P. Doyle, K. H. McWatters, *Journal of Food Protection* **65**(8), 1215 (2002).

[63] K. U. Schallreuter, et al., *Journal of Investigative Dermatology Symposium Proceedings* **4**(1), 91 (1999).

[64] E. Cadenas, K. J. Davies, *Free Radical Biology and Medicine* **29**(3-4), 222 (2000).

[65] Y. Xiao, et al., *Life Sciences* **112**(1-2), 33 (2014).

[66] S. Fahn, G. Cohen, *Annals of Neurology* **32**(6), 804 (1992).

[67] Y. Luo, H. Liu, Q. Rui, Y. Tian, *Analytical Chemistry* **81**(8), 3035 (2009).

[68] C.-Y. Lin, et al., *Talanta* **82**(1), 340 (2010).

[69] D. W. Kimmel, G. LeBlanc, M. E. Meschievitz, D. E. Cliffel, *Analytical Chemistry* **84**(2), 685 (2011).

[70] J. P. Lowry, R. D. O'Neill, *Analytical Chemistry* **64**(4), 453 (1992).

[71] J. E. Seegmiller, A. I. Grayzel, L. Laster, L. Liddle, *Journal of Clinical Investigation* **40**(7), 1304 (1961).

[72] M. D. Harris, L. B. Siegel, J. A. Alloway, *Am Fam Physician.* (1999).

[73] H. K. Walker, W. D. Hall, J. W. Hurst, *Clinical Methods: The History, Physical, and Laboratory Examinations*. Butterworths, 3 edn. (1990).

[74] J.-C. W. Kuan, S. Kuan, G. Guilbault, *Clinica Chimica Acta* **64**(1), 19 (1975).

[75] M. A. Ross, *Journal of Chromatography B: Biomedical Sciences and Applications* **657**(1), 197 (1994).

[76] L. Robitaille, L. J. Hoffer, *Nutrition Journal* **15**(1) (2015).

[77] M. A. Karimi, *International Journal of Electrochemical Science* **12**, 7089 (2017).

[78] M. A. Kamyabi, M. A. Shafiee, *Journal of the Brazilian Chemical Society* **23**(4) (2012).

[79] E. Kurowska-Tabor, M. Jaskuła, G. D. Sulka, *Electroanalysis* **27**(8), 1968 (2015).

[80] F.-F. Zhang, et al., *Analytical and Bioanalytical Chemistry* **382**(6), 1368 (2005).

[81] N. F. Atta, M. F. El-Kady, A. Galal, *Analytical Biochemistry* **400**(1), 78 (2010).

[82] W. Shi, et al., *Biosensors and Bioelectronics* **38**(1), 100 (2012).

[83] A. Liu, W. Chen, L. Huang, X. Lin, *Chemical & Pharmaceutical Bulletin* **56**(12), 1665 (2008).

[84] D. Liu, et al., *Nanotechnology* **27**(33), 33LT01 (2016).

[85] W.-w. Zhan, et al., *Journal of the American Chemical Society* **135**(5), 1926 (2013).

[86] Z.-H. Li, H. Guedri, B. Viguier, S.-G. Sun, J.-L. Marty, *Sensors* **13**(4), 5028 (2013).

[87] M. S. Lin, T. F. Tseng, *The Analyst* **123**(1), 159 (1998).

[88] C. H. D. Nieto, et al., *Sensors and Actuators B: Chemical* **263**, 377 (2018).

[89] S. Ghosh, S. C. Bhattacharya, A. Saha, *Analytical and Bioanalytical Chemistry* **397**(4), 1573 (2010).

[90] G. Kaur, S. Tripathi, *Materials Chemistry and Physics* **143**(2), 514 (2014).

[91] S. Bharti, G. Kaur, S. Gupta, S. Tripathi, *Journal of Luminescence* **181**, 459 (2017).

[92] M. G. Traber, J. F. Stevens, *Free Radical Biology and Medicine* **51**(5), 1000 (2011).

[93] K. A. Naidu, *Nutrition Journal* **2**(1), 145 (2003).

[94] G. Noctor, C. H. Foyer, *Annual Review of Plant Physiology and Plant Molecular Biology* **49**(1), 249 (1998).

[95] R. C. Rose, A. M. Bode, *The FASEB Journal* **7**(12), 1135 (1993).

[96] D. R. Lide, *Handbook of Chemistry and Physics*. CRC Press LLC, 84 edn. (2003-2004).

[97] N. A. Thorn, F. S. Nielsen, C. K. Jeppesen, *Acta Physiologica Scandinavica* **141**(1), 97 (1991).

[98] R. W. Welch, et al., *Journal of Biological Chemistry* **270**(21), 12584 (1995).

[99] L. Siliprandi, P. Vanni, M. Kessler, G. Semenza, *Biochimica et Biophysica Acta (BBA) - Biomembranes* **552**(1), 129 (1979).

[100] H. Helbig, et al., *American Journal of Physiology-Cell Physiology* **256**(1), C44 (1989).

[101] R. W. Welch, P. Bergsten, J. D. Butler, M. Levine, *Biochemical Journal* **294**(2), 505 (1993).

[102] L. Giannuzzi, N. E. Zaritzky, *LWT - Food Science and Technology* **29**(3), 278 (1996).

[103] N. Smirnoff, *Current Opinion in Plant Biology* **3**(3), 229 (2000).

[104] Y. Nishikawa, T. Kurata, *Bioscience, Biotechnology, and Biochemistry* **64**(3), 476 (2000).

[105] S. C. Rumsey, M. Levine, *The Journal of Nutritional Biochemistry* **9**(3), 116 (1998).

[106] A. Bode, L. Cunningham, R. Rose, *Clinical Chemistry* (1990).

[107] G. Bánhegyi, L. Braun, M. Csala, F. Puskás, J. Mandl, *Free Radical Biology and Medicine* **23**(5), 793 (1997).

[108] R. C. Rose, A. M. Bode, *Comparative Biochemistry and Physiology Part A: Physiology* **100**(2), 273 (1991).

[109] Y. Nishikawa, T. Kurata, *Food Science and Technology International, Tokyo* **4**(2), 155 (1998).

[110] T. Kurata, Y. Nishikawa, *Bioscience, Biotechnology, and Biochemistry* **64**(8), 1651 (2000).

[111] A. Z. M. Hussein, *Journal of Al-Nahrain University Science* **16**(3), 65 (2013).

[112] S. A. Maniyar, J. G. Jargar, S. N. Das, S. A. Dhundasi, K. K. Das, *Asian Pacific Journal of Tropical Biomedicine* **2**(3), 220 (2012).

[113] M. Shukla, P. Mishra, *Journal of Molecular Structure* **377**(3), 247 (1996).

[114] B. H. J. Bielski, A. O. Allen, *Journal of the American Chemical Society* **92**(12), 3793 (1970).

[115] B. N. Ames, R. Cathcart, E. Schwiers, P. Hochstein, *Proceedings of the National Academy of Sciences* **78**(11), 6858 (1981).

[116] R. J. Johnson, et al., *Hypertension* **41**(6), 1183 (2003).

[117] J. Maiuolo, F. Oppedisano, S. Gratteri, C. Muscoli, V. Mollace, *International Journal of Cardiology* **213**, 8 (2016).

[118] Y. Y. Sautin, R. J. Johnson, *Nucleosides, Nucleotides and Nucleic Acids* **27**(6-7), 608 (2008).

[119] B. Frei, R. Stocker, B. N. Ames, *Proceedings of the National Academy of Sciences of the United States of America* **85**, 9748 (1988).

[120] J. S. N. Dutt, M. F. Cardosi, J. Davis, *The Analyst* **128**(7), 811 (2003).

[121] G. Ragab, M. Elshahaly, T. Bardin, *Journal of Advanced Research* **8**(5), 495 (2017).

[122] R. Bentley, A. Neuberger, *Biochemical Journal* **52**(4), 694 (1952).

[123] A. A. Karyakin, *Electroanalysis* **13**(10), 813 (2001).

[124] A. Matilainen, M. Sillanpää, *Chemosphere* **80**(4), 351 (2010).

[125] A. Meireles, E. Giaouris, M. Simões, *Food Research International* **82**, 71 (2016).

[126] E. A. Veal, A. M. Day, B. A. Morgan, *Molecular Cell* **26**(1), 1 (2007).

[127] J. O. Bockris, L. F. Oldfield, *Transactions of the Faraday Society* **51**, 249 (1955).

[128] M. C. M. Vissers, M. Hampton, A. J. Kettle, *Hydrogen Peroxide Metabolism in Health and Disease*. CRC Press, 1 edn. (2017).

[129] S. Goldstein, D. Aschengrau, Y. Diamant, J. Rabani, *Environmental Science & Technology* **41**(21), 7486 (2007).

[130] M. K. Phibbs, P. A. Giguère, *Canadian Journal of Chemistry* **29**(6), 490 (1951).

[131] O. Blokhina, *Annals of Botany* **91**(2), 179 (2003).

[132] W. Khalid, et al., *Journal of Nanobiotechnology* **9**(1), 46 (2011).

[133] J. Li, Q. Yu, T. Peng, *Analytical Sciences* **21**(4), 377 (2005).

[134] P. Westbroek, E. Temmerman, *Journal of Electroanalytical Chemistry* **482**(1), 40 (2000).

[135] Y. Takano, et al., *Chem. Sci.* **7**, 3331 (2016).

[136] A. Goetzberger, C. Hebling, H.-W. Schock, *Materials Science and Engineering: R: Reports* **40**(1), 1 (2003).

[137] H. Imahori, et al., *Journal of the American Chemical Society* **123**(11), 2607 (2001).

[138] I. Hiroshi, et al., *Chemical Physics Letters* **263**(3-4), 545 (1996).

[139] H. Imahori, T. Umeyama, S. Ito, *Accounts of Chemical Research* **42**(11), 1809 (2009), PMID: 19408942.

[140] T. Numata, et al., *Journal of the American Chemical Society* **134**(14), 6092 (2012).

[141] C. A. Rozzi, F. Troiani, I. Tavernelli, *Journal of Physics: Condensed Matter* **30**, 013002 (2018).

[142] H. Imahori, et al., *The Journal of Physical Chemistry B* **103**(34), 7233 (1999).

[143] H. Imahori, Y. Sakata, *Advanced Materials* **9**(7), 537 (1997).

[144] D. M. Guldi, M. Prato, *Accounts of Chemical Research* **33**(10), 695 (2000).

[145] R. Koeppe, N. S. Sariciftci, *Photochemical & Photobiological Sciences* **5**(12), 1122 (2006).

[146] F. D'Souza, O. Ito, *Chem. Soc. Rev.* **41**(1), 86 (2012).

[147] J. Hare, H. Kroto, R. Taylor, *Chemical Physics Letters* **589**, 57 (2013).

[148] B. V. Lobanov, A. I. Murzashev, *Russian Physics Journal* **59**(6), 856 (2016).

[149] T. Higashino, et al., *Angewandte Chemie* **128**(2), 639 (2015).

[150] M. Yamamoto, J. Föhlinger, J. Petersson, L. Hammarström, H. Imahori, *Angewandte Chemie International Edition* **56**(12), 3329 (2017).

[151] N. Frenkel, et al., *Adv. Funct. Mater.* **24**, 4927 (2014).

[152] K. Bierbaum, et al., *Langmuir* **11**(2), 512 (1995).

[153] J. Howgate, et al., *Advanced Materials* **22**(24), 2632 (2010).

[154] Y. Zhao, P. Larimer, R. T. Pressler, B. W. Strowbridge, C. Burda, *Angewandte Chemie International Edition* **48**(13), 2407 (2009).

[155] G. Knör, *Chemistry - A European Journal* **15**(3), 568 (2009).

[156] D. Schaffhauser, M. Fine, M. Tabata, T. Goda, Y. Miyahara, *Biosensors* **6**(4), 11 (2016).

[157] R. C. Stringer, S. Schommer, D. Hoehn, S. A. Grant, *Sensors and Actuators B: Chemical* **134**(2), 427 (2008).

[158] W. J. Parak, et al., *Nanotechnology* **14**(7), R15 (2003).

[159] B. O. Dabbousi, et al., *The Journal of Physical Chemistry B* **101**(46), 9463 (1997).

[160] X. Michalet, *Science* **307**(5709), 538 (2005).

[161] N. Gomez, et al., *Talanta* **67**(3), 462 (2005).

[162] D. Gerion, et al., *The Journal of Physical Chemistry B* **105**(37), 8861 (2001).

[163] T. Pellegrino, et al., *Nano Letters* **4**(4), 703 (2004).

[164] S. T. Selvan, T. T. Y. Tan, D. K. Yi, N. R. Jana, *Langmuir* **26**(14), 11631 (2010).

[165] M. Vibin, et al., *Journal of Colloid and Interface Science* **357**(2), 366 (2011).

[166] I. L. Medintz, et al., *Nature Materials* **9**(8), 676 (2010).

[167] J. Zhang, A. M. Bond, *The Analyst* **130**(8), 1132 (2005).

[168] J. D. Marshall, M. J. Schnitzer, *ACS Nano* **7**(5), 4601 (2013).

[169] C. E. Rowland, et al., *Nano Letters* **15**(10), 6848 (2015).

[170] O. K. Nag, et al., *ACS Nano* **11**(6), 5598 (2017).

[171] C. Kirchner, et al., *Nano Letters* **5**(2), 331 (2005).

[172] S. Hölzel, et al., *Advanced Functional Materials* (2018).

[173] P. Reiss, J. Bleuse, A. Pron, *Nano Letters* **2**(7), 781 (2002).

[174] G. Decher, *Science* **277**(5330), 1232 (1997).

[175] S. L. Hörger, *Die segmentspezifischen Wirkungen von Adrenalin auf den Ionentransport am Colon der Ratte*, Ph.D. thesis, Institut für Veterinär-Physiologie, Justus-Liebig-Universität Gießen (1999).

[176] G. Prinz, *Intrazelluläre Ca^{2+}-Transporter im Kolonepithel der Ratte: Untersuchungen von Ryanodinrezeptoren sowie SERCAs*, Ph.D. thesis, Institut für Veterinär-Physiologie, Justus-Liebig-Universität Gießen (2007).

[177] K. Kunzelmann, M. Mall, *Physiol Rev.* **82**(1), 245 (2002).

[178] J. Sobotta, H. Becher, *Atlas der Anatomie des Menschen*, vol. 2. Urban and Schwarzenberg, 17 edn. (1972).

[179] B. Hennig, *Calcium-induzierte Chloridsekretion an isolierten Krypten aus dem Kolon der Ratte*, Ph.D. thesis, Institut für Veterinär-Physiologie, Justus-Liebig-Universität Gießen (2007).

[180] S. Bader, *Das non-neuronale cholinerge System des Kolons der Ratte*, Ph.D. thesis, Institut für Veterinär-Physiologie und –Biochemie, Justus-Liebig-Universität Gießen (2014).

[181] C. S. Potten, C. Booth, D. M. Pritchard, *International Journal of Experimental Pathology* **78**(4), 219 (1997).

[182] W. Specht, *Morpholgy of intestinal wall.* Intestinal permeation, Excerpta Medica, Amsterdam, Oxford (1977).

[183] M. Lipkin, *Annual Review of Physiology* **47**(1), 175 (1985).

[184] J. Williams, C. Duckworth, K. Vowell, M. Burkitt, D. Pritchard, *Curr. Protoc. Mouse Biol.* **6**, 148 (2016).

[185] S. B. Ho, *Journal of Cellular Biochemistry* **Supplement 16G**, 119 (1992).

[186] M. Horster, J. Fabritius, M. Büttner, R. Maul, P. Weckwerth, *Pflugers Arch.* **426**(1-2), 110 (1994).

[187] D. Dawson, *Annual Review of Physiology* **53**, 321 (1991).

[188] M. Diener, M. Nobles, W. Rummel, *Pflügers Archiv European Journal of Physiology* **421**(6), 530 (1992).

[189] M. Haas, B. F. III, *Annual Review of Physiology* **62**(1), 515 (2000).

[190] J. P. Geibel, S. Singh, V. M. Rajendran, H. J. Binder, *Gastroenterology* **118**(1), 101 (2000).

[191] K. E. Barrett, S. J. Keely, *Annual Review of Physiology* **62**(1), 535 (2000).

[192] J. L. Kinsella, P. S. Aronson, *Biochimica et Biophysica Acta (BBA) - Biomembranes* **689**(1), 161 (1982).

[193] H. Murer, U. Hopfer, R. Kinne, *Biochemical Journal* **154**(3), 597 (1976).

[194] J. L. Seifter, P. S. Aronson, *Journal of Clinical Investigation* **78**(4), 859 (1986).

[195] E. A. Arena, et al., *American Journal of Physiology-Cell Physiology* **302**(2), C412 (2012).

[196] B. Masereel, *European Journal of Medicinal Chemistry* **38**(6), 547 (2003).

[197] N. Demaurex, R. R. Romanek, J. Orlowski, S. Grinstein, *The Journal of General Physiology* **109**, 117 (1997).

[198] P. S. Aronson, *American Journal of Physiology-Renal Physiology* **240**(1), F1 (1981).

[199] M. Diener, C. Helmle-Kolb, H. Murer, E. Scharrer, *Pflügers Archiv European Journal of Physiology* **424**(3-4), 216 (1993).

[200] K. D. Burns, T. Homma, R. C. Harris, *American Journal of Physiology-Renal Physiology* **261**(4), F607 (1991).

[201] S. Grinstein, *The Journal of Cell Biology* **101**(1), 269 (1985).

[202] J. Orlowski, S. Grinstein, *The journal of biological chemistry* **272**, 22373 (1997).

[203] M. F. Frasco, N. Chaniotakis, *Sensors* **9**(9), 7266 (2009).

[204] Y.-S. Liu, et al., *The Journal of Physical Chemistry C* **111**(7), 2872 (2007).

[205] W. Shi, X. Li, H. Ma, *Methods and Applications in Fluorescence* **2**(4), 042001 (2014).

[206] A. Dowd, D. Pissuwan, M. B. Cortie, *Trends in Biotechnology* **32**(11), 571 (2014).

[207] S. Schäfer, A. H. R. Koch, A. Cavallini, M. Stutzmann, I. D. Sharp, *J. Phys. Chem. C* **116**(42), 22281 (2012).

[208] M. Diener, E. Scharrer, *Comparative Biochemistry and Physiology Part A: Physiology* **118**(2), 375 (1997).

[209] A. Gupta, J. Edwards, K. Hruska, *Bone* **18**(2), 87 (1996).

[210] M. George, et al., *Annals of the Rheumatic Diseases* **63**(1), 67 (2004).

[211] W. F. Boron, *The Journal of General Physiology* **67**(1), 91 (1976).

[212] J. Laurent, et al., *FEBS Journal* **281**(3), 683 (2013).

[213] S. Han, et al., *ACS Applied Materials & Interfaces* **2**(7), 1918 (2010).

[214] R. Ohgaki, et al., *Scientific Reports* **7**(1) (2017).

[215] J. Kneipp, H. Kneipp, B. Wittig, K. Kneipp, *Nanomedicine: Nanotechnology, Biology and Medicine* **6**(2), 214 (2010).

[216] H. Wang, D. Singh, L. Fliegel, *Journal of Biological Chemistry* **272**(42), 26545 (1997).

[217] I. Wakabayashi, M. Poteser, K. Groschner, *Journal of Vascular Research* **43**(3), 238 (2006).

[218] M. Chesler, *Physiological Reviews* **83**(4), 1183 (2003).

[219] G. Schultheiss, S. L. Kocks, M. Diener, *Biological Procedures Online* **3**(1), 70 (2002).

Acknowledgement

An dieser Stelle möchte ich mich gerne bei allen Personen bedanken, die mich im Verlauf meiner Promotion begleitet, unterstützt und motiviert haben.

Mein größter Dank gilt dabei meinem Mann. Danke, dass Du mich bei diesem Projekt immer unterstützt und dabei mein Wohl nie aus den Augen verloren hast. Du hast mir Kraft gegeben und somit einen großen Anteil an dem Gelingen dieser Arbeit gehabt.

Herzlichen Dank auch an meine ganze Familie und an all meine Freunde. Ihr habt mir meine Arbeit erleichtert, indem Ihr mir Pausen angeordnet und diese dann mit Freude und schönen gemeinsamen Stunden gefüllt habt. Ihr seid fantastisch!

Ich möchte mich im Besonderen bei meinem Doktorvater Prof. Dr. Martin Eickhoff bedanken. Vielen Dank für die Möglichkeit, dass ich eine interdisziplinäre Arbeit im Bereich der Biosensorik anfertigen konnte. Ich habe in meiner Doktorandenzeit viele verschiedene Labore durchlaufen, weit entfernte Länder besucht und wichtige Kontakte geknüpft. Dabei konnte ich sowohl meine wissenschaftlichen Fähig- und Fertigkeiten entwickeln als auch meine sozialen Kompetenzen erweitern. Danke dafür!
Da gibt es aber eine Sache, für die ich mich noch einmal extra bedanken möchte und die Du mir schon zu Beginn meines Studiums mit auf den Weg gegeben hast. Diese Sache hat mich seither begleitet, und mir erfolgreich in den schwierigen Zeiten Antrieb gegeben. Es waren Deine Worte mit folgendem Inhalt: “Nicht aufgeben, dranbleiben und durchziehen. Es ist noch nichts verloren.”
Egal, wie knapp die Fristen waren, wie herausfordernd die Durchführung der Experimente oder wie komplex die Ergebnisse. Diese Aussage im Zuge meiner Bewerbung für den Auslandsaufenthalt hat mir während meiner Promotion geholfen weiter motiviert dran zu bleiben und die Dissertation zu dem zu machen, was sie jetzt ist.
Vielen Dank!

Mein herzlicher Dank gilt Prof. Dr. Detlev Hofmann für die wissenschaftlichen Diskussionen im Arbeitsgruppenseminar und für die Übernahme des Korreferats dieser Arbeit.

Vielen Dank Prof. Dr. Martin Diener für die erfolgreiche Zusammenarbeit hinsichtlich des Bioimagings, den fachlichen Rat und die Bereitschaft Teil der Prüfungskommission zu sein.

Prof. Dr. Bernd Smarsly möchte ich für die Bereitschaft danken, Teil meiner Prüfungskommission zu sein.

Ich danke Jörg Teubert, dass er mich auf meinem Weg hin zur Promotion fachlich und auch freundschaftlich begleitet hat. Ich habe erst als Du weg warst gemerkt, wie wichtig diese aus kurzen Nachfragen resultierenden Diskussionen waren.

Dann möchte ich allen Ehemaligen der Arbeitsgruppe danken: Jens Wallys, Markus Schäfer, Gesche Müntze, Pascal Becker, Pascal Hille. Ich danke Euch dafür, dass Ihr viele Sachen schon ausprobiert und entwickelt habt, sodass ich direkt mit der Biosensoranwendung starten konnte. Danke für all die Tricks und Kniffe, die Ihr mir beigebracht habt. Ihr habt es einfach drauf!

Liebe Arbeitsgruppe Nanomaterialien, Euch allen danke ich für das, was den Arbeitsort an sich erst so angenehm gemacht hat: Meine Kollegen! Ich schließe hiermit alle ehemaligen und aktuellen Mitarbeiter ein, alle unsere Bachelor- und Masterstudenten wie auch der neue Kern in Bremen. Ich danke Euch für die Hilfe bei den Experimenten, bei den Diskussionen der Ergebnisse und Euren Rat. Wir hatten viele schöne Stunden, in denen wir uns nicht nur fachlich ausgetauscht, sondern uns auch gemeinsam die Zeit mit außerfachlichen Aktivitäten vertrieben haben. Wir waren ein gutes Team, und Ihr habt es mitverantwortet, dass die Arbeit ein schöner Ort war. Danke für die daraus entstandenen Freundschaften, liebe Paula, lieber Pascal, liebe Jans. Das ist etwas, das bleibt.

Vielen Dank an alle Freunde und Kollegen im I. Physikalischen Institut für die Gespräche und die gute Zusammenarbeit. Ich konnte meine Messungen bei Euch durchführen, und Ihr habt mir bei Problemen mit Rat und Tat zur Seite gestanden. Dankeschön!

Jetzt wird es technisch, aber nicht weniger wichtig. Danke an Thomas Wasem, der ausgeklügelte Messkammern mit entworfen und bei der Umsetzung mitgewirkt hat. Dankeschön auch an alle Mitarbeiter der Feinmechanik und der Elektronikwerkstatt. Roger Burger, Rainer Weiss, Ihr habt wirklich super Arbeit geleistet und die filigranen Entwürfe perfekt umgesetzt. Thomas Nimmerfroh und Björn Bellof, danke an Euch und Euer Team, dass Ihr meine Gerätschaften immer wieder in Gang gebracht habt.

Vielen Dank an alle Personen, die meist im Hintergrund agieren und trotzdem eine wichtige Rolle während der Entstehung dieser Arbeit hatten: Helge Höchsmann, Kerstin Will, Anja Dehnhardt, Susanne Jeske, Daniela Musaeus, Hans Peter Jorde, Renate Fuchs, Ute Balser.

Dann möchte ich mich noch bei den kooperierenden Arbeitsgruppen bedanken, mit denen wir erfolgreich zusammengearbeitet haben.

Danke für die gute Zusammenarbeit liebe Arbeitsgruppe “Prof. Martin Diener”. Allen voran möchte ich mich bei Dr. Ervice Pouokam für die Hilfestellungen bei der Messung der isolierten Krypten und der damit verbundenen Thematik bedanken. Du hattest immer ein offenes Ohr und hast dabei all meine Fragen geduldig beantwortet. Ich danke den wissenschaftlichen Mitarbeitern für den fachlichen Austausch, das Probenpräparieren und das Teilen Eurer Erfahrungen im Labor. Danke an alle technischen Angestellten für Eure Hilfe und die vielen Vorbereitungen. Danke, liebe Brigitta, Barbara, Alice! Ich war gerne bei Euch zum Messen und habe mich gut aufgenommen gefühlt.

Ich möchte mich herzlich bei Prof. Dr. Motomu Tanaka bedanken, dass ich die Chance hatte in der Arbeitsgruppe mitzuarbeiten und mir neue Methoden anzueignen. Ich konnte mich in dieser Zeit fachlich fortbilden und dabei Forschungsaufenthalte in Japan absolvieren. Danke für die wissenschaftlichen Besprechungen und Hilfestellungen und auch für das gute Sushi.

Dankeschön sowohl an Prof. Dr. Fred Lisdat und M.Sc. Marc Riedel für die gute Zusammenarbeit bei der NADH-Sensorik.

Vielen Dank an die Justus-Liebig-Universität Gießen, die diese Arbeit durch das Graduiertenstipendium finanziell unterstützt hat.

Selbstständigkeitserklärung

Ich erkläre: Ich habe die vorgelegte Dissertation selbständig und ohne unerlaubte fremde Hilfe und nur mit den Hilfen angefertigt, die ich in der Dissertation angegeben habe. Alle Textstellen, die wörtlich oder sinngemäß aus veröffentlichten Schriften entnommen sind, und alle Angaben, die auf mündlichen Auskünften beruhen, sind als solche kenntlich gemacht. Bei den von mir durchgeführten und in der Dissertation erwähnten Untersuchungen habe ich die Grundsätze guter wissenschaftlicher Praxis, wie sie in der „Satzung der Justus-Liebig-Universität Gießen zur Sicherung guter wissenschaftlicher Praxis“ niedergelegt sind, eingehalten.

Gießen, den

_____

Sara Hölzel